Review article

Stavroula Foteinopoulou*, Ganga Chinna Rao Devarapu, Ganapathi S. Subramania, Sanjay Krishna and Daniel Wasserman

Phonon-polaritonics: enabling powerful capabilities for infrared photonics

https://doi.org/10.1515/nanoph-2019-0232
Received July 31, 2019; revised August 30, 2019; accepted September 2, 2019

Abstract: Here, we review the progress and most recent advances in phonon-polaritonics, an emerging and growing field that has brought about a range of powerful possibilities for mid- to far-infrared (IR) light. These extraordinary capabilities are enabled by the resonant coupling between the impinging light and the vibrations of the material lattice, known as phonon-polaritons (PhPs). These PhPs yield a characteristic optical response in certain materials, occurring within an IR spectral window known as the reststrahlen band. In particular, these materials transition in the reststrahlen band from a high-refractive-index behavior, to a near-perfect metal behavior, to a plasmonic behavior – typical of metals at optical frequencies. When anisotropic they may also possess unconventional photonic constitutive properties thought of as possible only with metamaterials. The recent surge in two-dimensional (2D) material research has also enabled PhP responses with atomically-thin materials. Such vast and extraordinary photonic responses can be utilized for a plethora of unusual effects for IR light. Examples include sub-diffraction surface wave guiding, artificial magnetism, exotic photonic dispersions, thermal emission enhancement, perfect absorption and enhanced near-field heat transfer. Finally, we discuss the tremendous potential impact of these IR functionalities for the advancement of IR sources and sensors, as well as for thermal management and THz-diagnostic imaging.

Keywords: phonon-polaritons; superabsorbers; photonic crystals; infrared light; plasmonics; metamaterials; THz gap.

1 Introduction

The fast pace in progress of visible/near-infrared (IR) plasmonic optics [1, 2] has not been mirrored in the IR part of the electromagnetic (EM) spectrum. However, a plethora of applications would require extraordinary EM control at longer wavelengths throughout the mid-infrared (MIR) spectrum [3, 4], between 3 and 30 μm free-space wavelengths, and into the far-IR and terahertz (THz) spectrum [5] of sub-mm free-space wavelengths. A few characteristic examples of such applications are bio-molecule fingerprinting [6–8], inspections of energy efficiency of buildings [9], passive radiative cooling [10, 11], as well as diagnostic tools in dentistry and cancer detection [12]. Optical and optoelectronic components, such as sources, detectors, beam guides, beam splitters and beam-steering devices, that function in the mid- and far-IR [13], especially in integrable chipscale form [14, 15], are thus extremely important for studying and advancing the pertinent physics and developing new optical systems at these long wavelengths.

Here, we review the progress and most recent advances of the emerging and fast growing field of "phonon-polaritonics" [16, 17] or "reststrahlen optics" [18], which has brought about a range of versatile possibilities for harnessing IR light with the so-called phonon-polariton (PhP) or reststrahlen-band materials [19–24]. These materials were initially overlooked for applications requiring manipulation and control of IR light because of their near-perfect reflector properties in bulk form. However,

*Corresponding author: Stavroula Foteinopoulou, Electrical and Computer Engineering, University of New Mexico, Albuquerque, NM 87131, USA, e-mail: sfoteino@unm.edu. https://orcid.org/0000-0003-4405-5209
Ganga Chinna Rao Devarapu: Centre for Advanced Photonics and Process Analysis, Cork Institute of Technology, Cork, T12 P928, Ireland; and Tyndall National Institute, Cork, T12 R5CP, Ireland
Ganapathi S. Subramania: Sandia National Laboratories, P.O. Box 5800, Albuquerque, NM 87185, USA; and Electrical and Computer Engineering, University of New Mexico, Albuquerque, NM 87131, USA. https://orcid.org/0000-0002-6288-0344
Sanjay Krishna: Electrical and Computer Engineering, The Ohio State University, Columbus, OH, USA
Daniel Wasserman: Electrical and Computer Engineering, The University of Texas at Austin, Austin, TX, USA

the wide range of works that we review, highlight and discuss here have unveiled their powerful potential for IR photonics. We analyze in the following how these unconventional capabilities for IR light emission, detection, and manipulation emanate from the different possible photonic properties in the vicinity of the reststrahlen band. We will also discuss how some of these extraordinary IR effects are unique to PhP platforms and are not possible with metals.

In particular, this review article is structured as follows. In Section 2, we discuss why traditional metallic-based platforms which have revolutionized light control at optical frequencies do not possess the full range of light manipulation capabilities in the IR. In Section 3, we describe the characteristics of PhP materials, explaining how they obtain their interesting photonic responses from a resonant interaction between their phonon vibrations and the impinging EM field. We present examples of materials in this class, ranging from ionic crystals, semiconductors, as well as two-dimensional (2D) materials, along with the associated frequency spectrum of operation in Section 4. In Section 5 we review the distinct photonic responses that PhPs make available that include exotic indefinite permittivity responses [25] initially thought of as possible only with metamaterials. In Section 6, we go through the different types of modes supported by PhP media which are the essential building blocks providing the foundation for the progress in the phonon-polaritonics field. In Section 7, we review the capabilities unleashed by popular photonic material structuring routes when applied to PhP materials. In Section 8, we discuss avenues to tune, switch or reconfigure the responses of PhP material. In Section 9, we give examples of how to bring together PhP platforms with other photonic systems for new functionalities in hybrid platforms. Finally, we present our conclusions in Section 10 with a brief outlook on the future of the field.

2 Metallic platforms for IR light: possibilities and limitations

In order to provide a context for what capabilities and directions phonon-polariton platforms bring about in IR photonics we briefly review in this section widely-researched metallic platforms for IR light and discuss their possibilities and limitations. A range of unique IR photonic effects have been reported leveraging metallic platforms with significant relevance to a wide range of IR photonic applications. Examples include IR metasurfaces

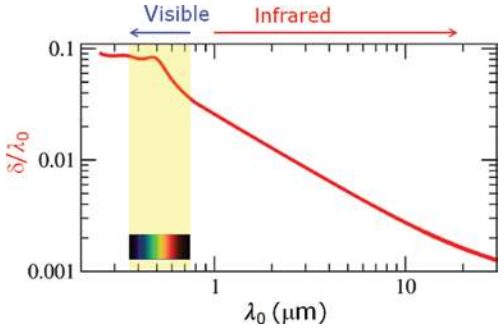

Figure 1: Spectral dependence of the skin depth of gold. The skin depth of gold, δ, with respect to the corresponding free-space wavelength λ_0 throughout the EM spectrum is shown. For the calculation of the skin-depth realistic models for the optical properties of gold are used obtained by fitting [32, 33] to experimental optical data [34, 35] at the relevant spectra.

[26], resonant or impedance matched platforms for super-absorption[1] [28, 29], spoof surface plasmons (SPs) [30], as well as resonant [31] or non-resonant [32] IR transparency and extraordinary near-field enhancement in perforated arrays. Actually, most of these platforms operate based on resonances induced by the geometry rather than the metallic material properties of the structural elements [26, 28–31]. All share a common feature: there is little overlap between IR light and the metallic matter, and the three-dimensional (3D) localization of the field around the metal constituents is rather weak.

This rather weak overlap between light and metallic matter is inherent to metallic platforms at IR frequencies. It emanates from the relatively small skin depth, δ, when compared to the free-space wavelength λ_0 (e.g. see Figure 1).[2] We note that despite the ultra-small skin depth with respect to the free-space wavelength in the IR spectrum the dissipative (ohmic) losses inside the metal may not be necessarily negligible; specifically in certain metamaterial-based IR detector architectures metallic losses as high as 20% have been reported [37]. However, such ultra-small relative skin depth most certainly prevents IR metal-optics systems [3] from reaching the full EM-field-sculpting

1 We use the term super-absorption here in line with literature in the area of enhancing absorption with structured materials; for example, see [27]. The term signifies a behavior where a structured platform exhibits a strong absorption, typically more than 80%, which at the same time represents a significant absorption enhancement with respect to the absorption exhibited by the lossy constituent material, when in bulk form.

2 The skin depth, represents the distance the EM wave travels before its electric field strength attenuates by a factor of $1/e$, [36]; so $\delta/\lambda_0 = 1/2\pi\kappa$, where κ is the imaginary part of the complex refractive index, or otherwise known as extinction coefficient [34].

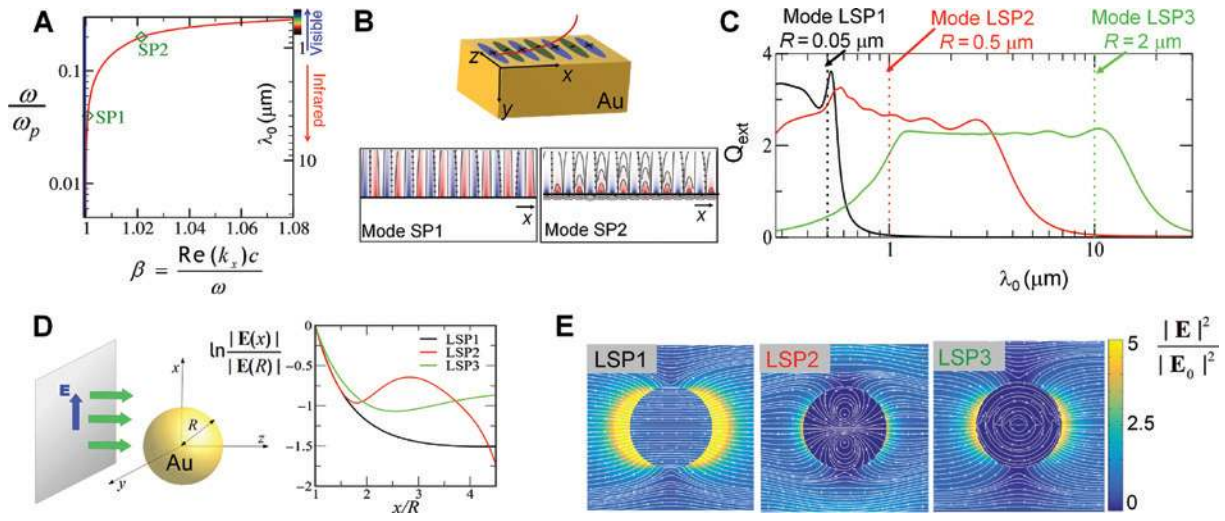

Figure 2: Planar and localized SPs from the IR to the visible spectrum.
(A) SPP dispersion from IR to visible at the air-gold interface (red line). The frequency, ω, and wave vector k_x, are expressed in dimensionless units, by scaling them with the plasma frequency ω_p and the free-space wave vector $k_0=\omega/c$, respectively; the vertical blue line is the lightline. (B) *x*-component of the electric field with associated streamlines for selected modes designated in (A). (C) Extinction efficiency, Q_{ext}, versus free-space wavelength λ_0 for three different Au spheres with a radius $R=0.05$ μm (black line), $R=0.5$ μm (red line), and $R=2$ μm (green line). (D) Field decay outside each of the gold spheres for selected modes designated in (B). $|\mathbf{E}(x)|$ represents the magnitude of the electric field at distance *x* from the sphere's center; *R* is the sphere's radius. (E) Electric field intensity landscape $|\mathbf{E}|^2$ normalized with the incident electric field intensity $|\mathbf{E}_0|^2$ for the same modes with associated streamlines (*xy*-plane view).

capabilities of plasmonic optics [2]. As a result, metals in the IR do not support the familiar highly-confined optical states at metallic planar interfaces, – known as SPs or surface-plasmon polaritons (SPPs) [38, 39] –, or around metallic particles, – known as localized surface plasmons resonances (LSPRs) [40], particle plasmons [41], or Mie plasmons [42, 43].

Indeed, this is attested by the representative examples for SPPs and LSPRs for gold (Au) shown in Figure 2. Specifically, Figure 2A depicts the dispersion relation, i.e. the frequency ω, versus the real part of the lateral wave vector $\mathrm{Re}(k_x)$, for the SPP modes at the vacuum-Au interface.[3] We see that for IR light of wavelength larger than ~3 μm the SPP mode dispersion is very close to the lightline (vertical blue line) signifying the free-space EM wave dispersion. The SPP mode's field profile, at these long wavelengths, has more in common with a grazing EM wave propagating along the *x*-direction rather than a surface wave localized around the interface (see panel SP1 of Figure 2B). The situation changes as the frequency increases towards the visible spectrum; the SPP mode moves away from the lightline while becoming more localized around the interface (e.g. see panel SP2 of Figure 2B).

To evaluate IR LSPR modes we calculate the extinction efficiency, Q_{ext} (see Figure 2C) accounting both for scattering and absorption for an EM wave launched onto a Au sphere.[4] Small, nm-sized, spheres are resonant at the visible spectrum, with absorption dominating their extinction response. On the other hand larger, sub-micron/micron-sized particles show a flat response, in the IR spectrum; the extinction response is absent of clearly defined resonances, and both scattering and absorption make a comparable contribution. Furthermore, the field decays much faster outside the sphere for the nm-sized sphere (mode LSP1[5]; see Figure 2D). In other words, near-resonance visible light can be strongly localized around a nm-sized metal particle (e.g. mode LSP1), while IR EM-fields are only weakly confined around larger micron-sized particles over a spectral region without clearly defined resonances (e.g. modes LSP2 and LSP3) (see also corresponding electric field intensity landscapes in Figure 2E).

The tight electric-field confinement around planar interfaces or particle geometries underpins most observed plasmonic phenomena in the visible spectrum. Moreover,

3 This is calculated from the well-known exact Raether expression [38] in its full complex form with the use of realistic parameters for Au as in Figure 1.

4 Calculated with the Mie theory (see [42, 44]) using the realistic Au permittivity as in Figure 1.

5 The term mode has been used loosely here for the highly-lossy metallic systems to describe the near-field excitation [42] and associated extinction that corresponds to a specific frequency, ω; in the strictest definition modes can be associated only with lossless systems.

certain types of photonic metamaterials whose design relies on a judicious volumetric mixing between constituents with opposite permittivities, such as epsilon-near-zero [45, 46] or hyperbolic metamaterials [47, 48] also require constituents with photonic responses similar to those yielding plasmonic phenomena. Clearly, then, the aforementioned phenomena and properties would not be transferable to the mid-/far-IR spectrum with traditional metallic structures. A very active research direction to bring the familiar effects of visible/near-IR plasmonics into the mid-/far-IR spectrum involves alternative plasmonic materials for IR light such as graphene [49, 50], conductive oxides [51, 52], or heavily-doped semiconductors [53–55]. We direct the reader to [3, 56, 57] reviewing this broad and highly-promising area.

Here, we review a different burgeoning research direction that involves tailoring IR photonic behaviors that do not emanate predominantly from the material free carriers. This research direction involves PhP materials which owe their photonic responses to the strong coupling of light and certain vibrational modes of the material lattice. As we discuss in the sections that follow, these photonic responses not only may mimic those of noble metals at visible frequencies and thus are ideal candidates for enabling "plasmonic effects" at the mid-/far-IR spectrum but also enable unconventional photonic responses and associated extraordinary modes.

3 Beyond metals: IR photonics with PhP materials

3.1 What are PhPs?

The native out-of-phase vibrational modes of the lattice (optical phonons) can strongly couple to impinging IR EM fields (photons) for certain types of solids. Such strong coupling can be triggered only in solids comprising oppositely charged atoms in their lattice basis so that the incident electric field can drive their out-of-phase vibrational modes; also known in the spectroscopy community as IR active phonons [58]. As a result of such strong coupling, an EM wave going through such solid would have mixed wave dispersion characteristics, which are neither "photon-like" nor "phonon-like" [23]. We depict the wave dispersion of these "mixed modes," known as PhPs, in Figure 3 (red solid line). Polar covalent semiconductors can be seen as effectively comprising two separate oppositely charged ions [59] and therefore also support IR active phonons and thus PhP modes.

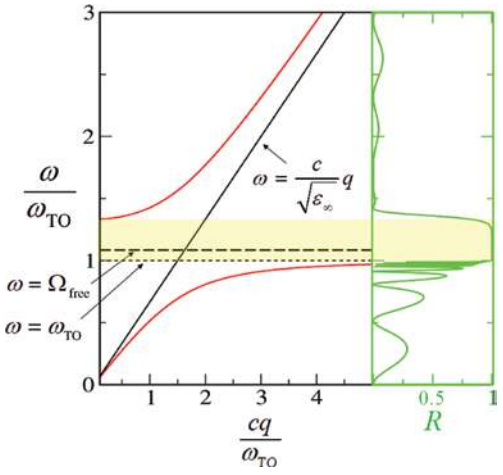

Figure 3: PhP dispersion relation.
The frequency ω versus wave vector q for strongly coupled lattice optical phonons (long-dashed horizontal line at Ω_{free}) with the radiation field (slanted solid lines) signifying mixed phonon-photon modes (red lines). The asymptote at the lower branch (short-dashed horizontal line) designates the frequency of the TO phonon, ω_{TO}. The yellow shaded regions represents the PhP gap or reststrahlen band (region of no mixed phonon-photon modes). Conversely, a slab of material in this frequency region is nearly perfectly reflecting. [See reflectance, R (green line).] ε_∞ and c represent the high frequency permittivity of the material and speed of light, respectively.

3.2 A microscopic model for the macroscopic PhP photonic responses

To understand the strong phonon-photon coupling phenomenon and its effect on the macroscopic optical response of ionic or ionic-like solids, we consider a basic, simple cubic diatomic lattice model. This comprises two oppositely charged ions with charges $+Q$, $-Q$ and respective masses M_+, M_-, as depicted in Figure 4A. These charges correspond to effective charges in real materials as the concept of a perfect ionic medium is an idealized model [59]. We consider an EM wave incident with electric field $\mathbf{E}_{inc}$ along the x-direction, launched from atop the structure of Figure 4A along the $+y$-direction. In order to satisfy the EM boundary conditions at the interface the wave-vector of the coupled radiation field-phonon wave inside the ionic medium, $\mathbf{q}$, must also lie in the y-direction [60]. Also, from Maxwell's equations it follows that the displacement vector $\mathbf{D}$ should be divergence-free inside the ionic material, implying that $\mathbf{q} \cdot \mathbf{D} = 0$ [60]. Assuming linear and isotropic materials:

$$\mathbf{D} = \mathbf{P} + \varepsilon_0 \mathbf{E} = \varepsilon \varepsilon_0 \mathbf{E} \quad (1)$$

where $\mathbf{P}$ is the polarization, defined as the dipolar moment per unit volume, ε is the relative permittivity of the material and ε_0 is the vacuum permittivity. It follows from all

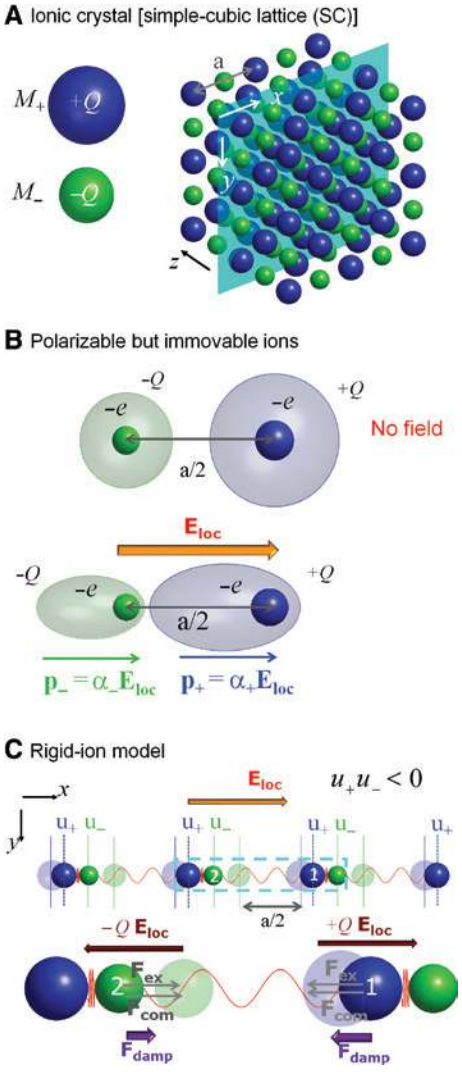

Figure 4: The ionic lattice and its response under the local electric field in the immovable-ion and rigid-ion models.
(A) A simple cubic ionic lattice of lattice constant, a, comprising positive ions of mass M_+ and charge $+Q$ and negative ions of mass M_- and charge $-Q$. (B) Dipole moment contributions, $\mathbf{p}_+$ and $\mathbf{p}_-$ of each of the deformable ion types assuming they are immovable. The displaced electron clouds around the ionic cores under the influence of the local electric field $\mathbf{E}_{loc}$ are shown. (C) The ions moving as rigid, non-deformable ions, under the influence of the local electric field $\mathbf{E}_{loc}$ and elastic restoring forces coming from the extended and compressed "inter-ionic springs", $\mathbf{F}_{ex}$ and $\mathbf{F}_{com}$. A diatomic chain of the ions at certain depth, *y*, of the cubic lattice is depicted, where the positive (negative) ions are displaced from their equilibrium positions by u_+ (u_-). The equilibrium positions for each ion type are designated with respective faint colored spheres. The bottom panel, is a zoomed depiction of the section within the cyan dashed lines, with the relevant forces in each kind of ions depicted. Damping forces, are also present (designated as $\mathbf{F}_{damp}$).

the above, that **D**, **P**, and **E** are along the *x*-direction inside the ionic material and normal to the wave-vector **q** of the PhP wave.

In order to understand the phonon-photon strong coupling we must understand how the macroscopic electric field, **E**, and polarization, **P**, correlate with the microscopic properties and motion of the atoms, as well as with the microscopic local electric field $\mathbf{E}_{loc}$. In lattices of tetrahedral symmetry, the local microscopic field at the center of both types of ions [61, 62] is given by:

$$\mathbf{E}_{loc} = \mathbf{E} + \frac{\mathbf{P}}{3\varepsilon_0}. \tag{2}$$

This local electric field, $\mathbf{E}_{loc}$, is the superposition of the impinging EM wave, and the long-range electrostatic field of the rest of the ions in the lattice. The macroscopic polarization in the ionic crystal, **P**, will be a superposition of the polarization resulting from the dipole moments of each kind of the two polarizable ions and the polarization from the dipole moments emanating from the oppositely-charged ions as they move. In particular, for the former contribution, we assume immovable but deformable ions under the influence of the local electric field $\mathbf{E}_{loc}$. The local electric field shifts the electron cloud around the ionic cores in each ion type (see Figure 4B). The contributing dipole moments of each ion type ($\mathbf{p}_-$ and $\mathbf{p}_+$) yield a total macroscopic polarization of:

$$\mathbf{P}_{immov} = N(\mathbf{p}_+ + \mathbf{p}_-) = N(\alpha_+ + \alpha_-)\mathbf{E}_{loc} = N\alpha\mathbf{E}_{loc}, \tag{3}$$

where *N* represents the number of positive-negative ion pairs per unit volume, and α_+, α_- the respective polarizabilities of the positively-charged and negatively-charged ions. We have set $\alpha = \alpha_+ + \alpha_-$ to represent the total polarizability of the oppositely-charged ion pair.

Conversely, for the latter contribution, i.e. for the polarization from the dipole moments emanating from the oppositely-charged ions as they move, we consider the oppositely-charged ions as rigid ions moving under the influence of the local electric field $\mathbf{E}_{loc}$ and the restoring forces from the inter-atomic potential. By rigid ions we mean that the ions move with the electron cloud tight around them [23], i.e. neither of the ions is polarizable (see Figure 4C). Then a net dipole moment in the elementary cell can be obtained only when there is a net displacement **w** of the positive ions with respect to the negative ions, yielding a total macroscopic polarization of:

$$\mathbf{P}_{rigid-ion} = NQ\mathbf{w}, \tag{4}$$

Accounting for both types of contributions to the microscopic dipole moments, the total polarization, **P**, would be:

$$\mathbf{P} = \mathbf{P}_{immov} + \mathbf{P}_{rigid-ion} = N[\alpha\mathbf{E}_{loc} + Q\mathbf{w}] \tag{5}$$

As the macroscopic polarization and field are parallel to each other [see Eq. (1)], i.e. $\mathbf{E}\|\mathbf{P}$, it follows from Eq. (2) that the microscopic local field, $\mathbf{E}_{\text{loc}}$, is parallel to both of them. Then Eq. (5) implies that the relative displacement between the positive and negative ions, $\mathbf{w}$, must also remain parallel to all fields. So, we have that $\mathbf{E}_{\text{inc}}\|\mathbf{E}_{\text{loc}}\|\mathbf{E}\|\mathbf{P}\|\mathbf{w}$, with all perpendicular to the wave vector $\mathbf{q}$. In other words, $\mathbf{w}\cdot\mathbf{q}=0$, meaning that the impinging EM can drive only the transverse phonon vibrational waves [19, 24].

Eqs. (2) and (5) can be also used to express both the local electric field, $\mathbf{E}_{\text{loc}}$, and the polarization, $\mathbf{P}$ in term of the macroscopic field $\mathbf{E}$. We get:

$$\mathbf{P}=\frac{1}{1-\frac{N\alpha}{3\varepsilon_0}}[N\alpha\mathbf{E}+NQ\mathbf{w}], \tag{6}$$

and

$$\mathbf{E}_{\text{loc}}=\frac{1}{1-\frac{N\alpha}{3\varepsilon_0}}\left[\mathbf{E}+\frac{NQ}{3\varepsilon_0}\mathbf{w}\right], \tag{7}$$

So, all displacements and fields are along the x-direction, while the PhP mode propagates along the y-direction. If the incoming EM field is a harmonic field of frequency ω, so will be the macroscopic field inside the ionic medium, which still must satisfy Maxwell's equations. As Eqs. (2), (6) and (7) must be obeyed at any depth of the lattice, the macroscopic field, $\mathbf{E}$, the local field, $\mathbf{E}_{\text{loc}}$, the polarization, $\mathbf{P}$, and the relative displacement, $\mathbf{w}$, all would follow the same waveform [24], i.e. we have:

$$\begin{pmatrix}\mathbf{E}\\ \mathbf{E}_{\text{loc}}\\ \mathbf{P}\\ \mathbf{w}\end{pmatrix}=\begin{pmatrix}E_0\\ E_{\text{loc},0}\\ P_0\\ \text{w}_0\end{pmatrix}e^{i(qy-\omega t)}\hat{\mathbf{x}}, \tag{8}$$

with E_0, $E_{\text{loc},0}$, P_0 and w_0 representing their respective amplitudes.

To understand further the motion of the ions in the lattice (in the rigid-ion model of Figure 4C), we take $\mathbf{E}_{\text{loc}}$ at a certain depth y to be constant, i.e. we ignore any spatial variations at the inter-ion scale [24, 61]. Thus, it suffices to focus our attention on two particular ions at certain depth y, one positive and one negative [e.g. see ions designated with (1) and (2) in Figure 4C]. The short-range forces between adjacent ions can be approximated as restoring forces [23], similar to the elastic force between two masses connected with a spring. A damping force proportional to the velocity of the ion is also taken, to account for dissipation in realistic lattices with the assumption that the more massive ion experiences a proportionally stronger damping force. We take u_+, u_- to represent the respective displacements along the x-direction of the positive and negative ions in the chain from their equilibrium position. We also take k to represent the elastic constant of the restoring force on the ions, and γ to be a constant related to the strength of the damping force. Then the the equation of motion becomes [23, 62]:

$$M_+\ddot{u}_+=QE_{\text{loc}}-2k(u_+-u_-)-\gamma M_+\dot{u}_+, \tag{9}$$

for the positive ions, and

$$M_-\ddot{u}_-=-QE_{\text{loc}}+2k(u_+-u_-)-\gamma M_-\dot{u}_-, \tag{10}$$

for the negative ions.

In order to understand better how the incident field drives the motion of the two kinds of ions in the lattice we temporarily ignore the damping term in Eqs. (9) and (10). Then, by adding these and integrating over time (assuming at $t=0$ the ions are at their equilibrium position) we get that:

$$M_+u_++M_-u_-=0. \tag{11}$$

Eq. (11) signifies that the motion of the positive and negative ions will be out-of-phase with $u_+u_-<0$. Also, if w_0 is the maximum value of the relative displacement, w, along the x-direction, i.e. $\text{w}=u_+-u_-=\text{w}_0e^{i(qy-\omega t)}$, we would have that:

$$u_+=\frac{1}{1+\frac{M_+}{M_-}}\text{w}_0e^{i(qy-\omega t)}, \tag{12}$$

and

$$u_-=-\frac{1}{1+\frac{M_-}{M_+}}\text{w}_0e^{i(qy-\omega t)}, \tag{13}$$

The PhP wave is a slow varying wave in the y-direction. Meaning, the wave would need to cross several atoms typically of the order of a 1000 or more for a full cycle. In Figure 5, we depict a snapshot of the transverse PhP wave.

We follow through to determine the amplitude of the relative ion displacement, w_0, needed to determine the macroscopic polarization and thus the effective photonic response of the ionic medium. It can be shown, by subtracting Eq. (10) from Eq. (9), after multiplying them

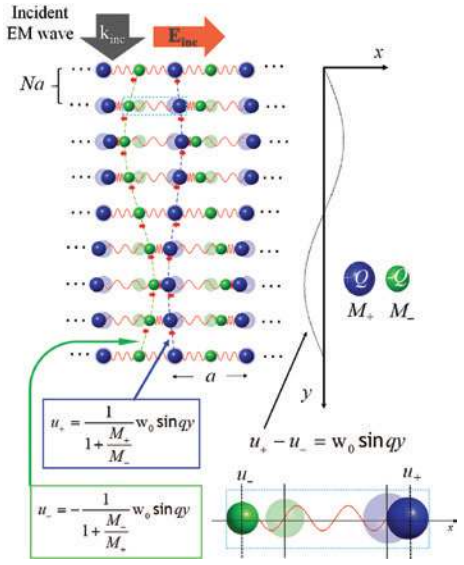

Figure 5: The transverse PhP wave.
The displacement of the ions is along the electric field of the impinging EM wave and perpendicular to the propagation direction, *y*. Because this is a slow-varying wave in the atomic scale, the ions along the *y*-direction are depicted only every *N* lattice planes, with *N* being of the order of a 1000 atoms or more. The displacements of the positive and negative ions are always out-of-phase (optical-phonon mode) with a respective ratio of $-M_-/M_+$ in the absence of damping. This out-of-phase phonon mode is activated by an impinging IR EM wave that displaces the two oppositely-charged ions in opposite directions; hence this mode is also known as IR-active optical phonon.

respectively, with M_+ and M_-, and using Eq. (7) to express the local field in terms of the macroscopic field, that:

$$M\ddot{\mathrm{w}} = \frac{Q}{1-\dfrac{N\alpha}{3\varepsilon_0}}E - \left(2k - \frac{\dfrac{NQ^2}{3\varepsilon_0}}{1-\dfrac{N\alpha}{3\varepsilon_0}}\right)\mathrm{w} - M\gamma\dot{\mathrm{w}}, \tag{14}$$

with M being the reduced mass of the the ion-pair of Figure 4C given by:

$$M = \frac{M_+M_-}{M_+ + M_-}. \tag{15}$$

After setting,

$$\omega_R^2 = \frac{2k}{M} - \frac{1}{M}\frac{\dfrac{NQ^2}{3\varepsilon_0}}{1-\dfrac{N\alpha}{3\varepsilon_0}}, \tag{16}$$

and using Eq. (8) into Eq. (14) we obtain:

$$\mathrm{w}_0 = \frac{\dfrac{Q}{M}}{1-\dfrac{N\alpha}{3\varepsilon_0}}\frac{1}{\omega_R^2 - \omega^2 - i\omega\gamma}E_0 \tag{17}$$

We first consider a limiting case: when the driving field is a high frequency field. For such a case, the atomic polarizability from the electron displacement dominates the permittivity response; the fields change too fast for the ions to respond (the atoms having much larger inertia in comparison to electrons). This means that the displacement, w, in Eq. (6) can be taken to be zero. We can see that also from Eq. (17) as $\mathrm{w}_0 \to 0$ as $\omega \to \infty$. Then from Eqs. (1) and (6) we get the familiar Clausius-Mossotti relation [19] for the high-frequency permittivity, ε_∞:

$$\frac{N\alpha}{3\varepsilon_0} = \frac{\varepsilon_\infty - 1}{\varepsilon_\infty + 2}. \tag{18}$$

Eq. (18) allows simplifying (16) to:

$$\omega_R^2 = \frac{2k}{M} - \frac{1}{M}\frac{NQ^2}{9\varepsilon_0}(\varepsilon_\infty + 2). \tag{19}$$

Now we consider another limiting case: the driving field being a static field, i.e. $\omega = 0$. Then from Eqs. (17) along with Eqs. (1) and (6) we get for the static permittivity ε_s:

$$\varepsilon_s = \varepsilon_\infty + \frac{1}{M\omega_R^2}\frac{\dfrac{NQ^2}{\varepsilon_0}}{\left(1-\dfrac{N\alpha}{3\varepsilon_0}\right)^2} = \varepsilon_\infty + \frac{(\varepsilon_\infty + 2)}{\dfrac{2k}{\dfrac{NQ^2(\varepsilon_\infty+2)}{9\varepsilon_0}} - 1}. \tag{20}$$

Conversely, we get for the permittivity response [with the successful application of Eqs. (1), (6), (17) and (20)]:[6]

$$\varepsilon(\omega) = 1 + \frac{1}{\varepsilon_0}\frac{P_0}{E_0} =$$

$$1 + \frac{\dfrac{N\alpha}{\varepsilon_0}}{1-\dfrac{N\alpha}{3\varepsilon_0}} + \frac{1}{M}\frac{\dfrac{NQ^2}{\varepsilon_0}}{\left(1-\dfrac{N\alpha}{3\varepsilon_0}\right)^2}\frac{1}{\omega_R^2 - \omega^2 - i\omega\gamma} =$$

$$\varepsilon_\infty\left(1 + \frac{\dfrac{\varepsilon_s}{\varepsilon_\infty}\omega_R^2 - \omega_R^2}{\omega_R^2 - \omega^2 - i\omega\gamma}\right) \tag{21}$$

6 The (–) sign before the $i\omega\gamma$ term is consistent with harmonic fields varying in time as $e^{-i\omega t}$. This is the physics convention that will be followed throughout the paper. Note, the engineering convention considers harmonic fields varying in time as $e^{i\omega t}$, in which case then a (+) instead of (–) should precede the term $i\omega\gamma$ in the related expressions.

To understand the physical meaning of the frequency ω_R in Eq. (21) we assume for a moment an undamped system, i.e. a system with $\gamma=0$; then as $\omega\to\omega_R$, Eq. (17) implies that the amplitude of oscillations becomes infinite. Essentially, ω_R, represents the frequency of the transverse optical (TO) phonon vibrations that are driven by a static field [63]. We will designate such frequency as ω_{TO} and simply refer to it as TO phonon frequency, i.e. $\omega_R\equiv\omega_{\text{TO}}$. The TO phonon frequency is somewhat different from the free vibration optical phonon mode, Ω_{free}, of a diatomic chain which for $q=0$ [19] is:

$$\Omega_{\text{free}}=\sqrt{\frac{2k}{M}}. \tag{22}$$

Then, with the use of Eqs. (16), (18) and (22), it can be shown that:

$$\Omega_{\text{free}}=\sqrt{\frac{\varepsilon_s+2}{\varepsilon_\infty+2}}\omega_{\text{TO}}, \tag{23}$$

which means the TO phonon frequency of modes driven by a static electric field is lower than the free vibrational optical phonon modes of a diatomic chain (both are designated with horizontal long-dashed and short-dashed lines, respectively in Figure 3).

Continuing, we can observe that at $\omega=\sqrt{\frac{\varepsilon_s}{\varepsilon_\infty}}\omega_{\text{TO}}$, the permittivity, ε, becomes zero (for the undamped system). Previously, we stated that only TO phonons couple to the radiation field. Indeed, the divergence-free nature of the displacement field **D**, mandates $\varepsilon\mathbf{q}\cdot\mathbf{E}$ to be zero which requires the wave vector **q** to be perpendicular to the driving field **E**, i.e. requires transverse modes. However, when the permittivity, ε, is exactly zero, the divergence-free condition for the displacement field **D** may be satisfied without requiring transverse modes, meaning longitudinal modes may be possible in this case. This is the reason why the frequency at which the permittivity, ε becomes zero for the undamped system, is called the longitudinal optical (LO) phonon frequency [19], ω_{LO}. Hence we obtain the famous Lyddane-Sachs-Teller (LST) relation [19, 23]:

$$\omega_{\text{LO}}=\sqrt{\frac{\varepsilon_s}{\varepsilon_\infty}}\omega_{\text{TO}} \tag{24}$$

With the use of the LST relation, we are able to obtain from Eq. (21) the familiar expression for the dielectric function of PhP media:

$$\varepsilon(\omega)=\varepsilon_\infty\left(1+\frac{\omega_{\text{LO}}^2-\omega_{\text{TO}}^2}{\omega_{\text{TO}}^2-\omega^2-i\omega\gamma}\right) \tag{25}$$

Eq. (25) encompasses the basic photonic responses that result from strong phonon-photon coupling as derived from a classical microscopic picture for the motion of the ions and the associated electron cloud. The particular parameters of a certain material are extracted from experimental reflectivity and/or ellipsometry spectra (see Section 4). Very recently Rivera et al. [64] showed that a quantum mechanical model leads to an effective permittivity response that is essentially equivalent to that of Eqs. (21) and (25).[7] The quantum model [64], which encompasses treatment of more complex unit cells with multiple-atom basis and tensorial Born effective charges, provides a pathway to first-principle predictions of PhP permittivities, which is particularly important for emergent materials where experimental data may not be available.

3.3 The PhP gap and the reststrahlen band

Figure 3 depicts the coupled phonon-radiation field wave dispersion, ω versus q, i.e. the PhP dispersion (red solid lines). This is determined by $\omega=\frac{c}{\sqrt{\varepsilon(\omega)}}q$, where $\varepsilon(\omega)$ is the permittivity response of Eq. (25). The two mixed phonon-photon mode branches are strongly modified from both the phonon dispersion (long-dashed horizontal line) and the high-frequency photon dispersion (slanted solid line, with $\omega=\frac{c}{\sqrt{\varepsilon_\infty}}q$). The phonon-mode dispersion appears flat as it represents phonons with a near-zero phonon wave vector, q. As EM waves are extremely slow varying in the atomic scale it is only the near-zero-q phonons which may couple to EM waves. The frequency region where no mixed phonon-photon modes (yellow-shaded region) is known as the PhP gap signifying forbidden EM propagation; almost all impinging light would get reflected from the material [see Figure 3 (right panel) showing the reflectance from a respective slab with thickness about a half the impinging light's wavelength].

Alternatively, the PhP gap is called the reststrahlen band; a term coming from German for the spectrum of "residual radiation". Historically, this term emerged [65] from experiments where a pulsed signal is reflected back and forth between slabs made of a PhP material. While the radiation comprising most of the pulse's frequency spectrum transmits through the slabs and escapes the

7 The quantum mechanical model captures also non-local permittivity responses dependent on the phonon wave vector q; these however are unimportant for typical photonic set-ups where EM waves interact with the near-zero q phonons.

set-up, the part of the pulse with frequencies within the PhP gap nearly-perfectly reflects on the surfaces of these slabs, thereby remaining trapped in the slit area between them. These "residual" radiation/rays [66] exit eventually through the slit as a narrow-band beam after multiple bounces. Set-ups like these had been used in the past to create narrowband/quasi-monochromatic sources from broadband thermal sources [65].

The permittivity is negative, i.e. $Re(\varepsilon)<0$, within the PhP gap/reststrahlen band. In the sections that follow we review interesting photonic phenomena and properties within but also around the vicinity of the reststrahlen band; we will be referring to this broader spectral region as the PhP regime.

3.4 Extensions to the basic PhP permittivity model for a broader class of material

The basic permittivity model of Eq. (25) covers successfully the photonic response of some materials but it may be too crude for others where the assumptions made in Section 3.2 fail by a large degree. For example, in the microscopic model the damping was simply associated with a single force proportional to the velocity of the ions. However, there are different distinct mechanisms causing damping of the PhP mode. Mechanisms that can cause PhP damping are scattering at crystal defects [67], as well as decay of the phonon-part of the PhP into acoustic phonons [67–70]; the latter is caused by the presence of anharmonic terms in the interatomic forces [71]. Damping can also occur because of other coupling to low frequency phonon excitations aided by strain or defects [67, 70, 72].

Schwarz and Maier [70] have asserted that damping caused by the presence of defects and the anharmonicity in the ionic potential can be lumped together in the decay constant γ of Eq. (25). However, according to [70] coupling to low frequency phonon excitations adds up a number of Lorentzian oscillatory terms in the denominator of Eq. (25) with associated poles at the zeros of $\omega_n^2-\omega^2-i\omega\gamma_n$, where ω_n and γ_n are the resonant frequencies and damping constants of the low-frequency phonon excitations. In materials where multiple of these damping mechanisms are dominant, as for example, in lithium niobate [73], other authors [67, 73, 74] have considered a frequency-dependent decay constant in the model of Eq. (25), $\gamma(\omega)$; a causal model [60] however requires $\gamma(\omega)$ to be itself complex valued [74]. The treatment of [70] offers more insight to the actual physical mechanisms of damping, beyond considering ad-hoc parameters that improve the agreement between the model-predicted PhPs and experimental results [74].

Furthermore, depending on the lattice symmetry multiple optical phonon branches may exist also. If these are well-separated in frequency, Eq. (25) serves as a good model in the neighborhood of the TO phonon frequency of interest. By well-separated we mean that there should not be a significant spectral overlap between adjacent TO phonon resonances, when taking into account their respective broadening as determined by the decay constant, γ_l, associated with the respective phonon resonance, $\omega_{\mathrm{TO},l}$. This however, is not true for many materials for which in order to construct the photonic response N independent harmonic oscillators should be considered. Each oscillator corresponds to one of the relevant TO phonon resonances $\omega_{\mathrm{TO},l}$ with damping γ_l with a corresponding LO phonon frequency $\omega_{\mathrm{LO},l}$, that is independent of the other oscillators [75]. So, the full permittivity response would be in such case:

$$\varepsilon(\omega)=\varepsilon_\infty+\sum_{l=1}^{N}\frac{\varepsilon_\infty(\omega_{\mathrm{LO},l}^2-\omega_{\mathrm{TO},l}^2)}{\omega_{\mathrm{TO},l}^2-\omega^2-i\omega\gamma_l}, \tag{26}$$

Not all the oscillators contribute equally; the strength of each oscillator, S_l, is determined by [76]:

$$S_l=\varepsilon_\infty\left(\frac{\omega_{\mathrm{LO},l}^2}{\omega_{\mathrm{TO},l}^2}-1\right), \tag{27}$$

implying that a certain oscillator makes a stronger contribution the larger the relative difference between the respective LO and TO phonon frequencies.

Eq. (26) can be approximated to the simpler expression [75, 77]:

$$\varepsilon(\omega)\approxeq\varepsilon_\infty\prod_{l=1}^{N}\frac{\omega_{\mathrm{LO},l}^2-\omega^2-i\omega\gamma_{\mathrm{LO},l}}{\omega_{\mathrm{TO},l}^2-\omega^2-i\omega\gamma_{\mathrm{TO},l}}. \tag{28}$$

Note here that, the independent oscillator model of Eq. (26) would have led to the same decay constant, γ_l, appearing in both the numerator and denominator of Eq. (28) [75, 78]. However, Gervais and Piriou [78] have asserted that a model that permits a different broadening of the LO and TO phonon resonance, – or in other words a different decay constant in the numerator, $\gamma_{\mathrm{LO},l}$ and in the denominator, $\gamma_{\mathrm{TO},l}$ respectively –, better captures the permittivity response for materials where the anharmonic decay channel of the PhP is strong [75, 78]. There are some constraints in the permissible values for the decay constants, mandated by the passivity condition for the permittivity model which requires the imaginary part of the

permittivity function to be positive or zero, i.e. $\mathrm{Im}[\varepsilon(\omega)] \geq 0$ [79]. In particular [75, 79]:

$$\sum_{l=1}^{N} (\gamma_{\mathrm{LO},l} - \gamma_{\mathrm{TO},l}) \geq 0. \tag{29}$$

4 Widely-used and emergent PhP materials

4.1 Ionic crystals (insulators)

Ionic crystals are the quintessential example of media with a PhP response. Table 1 outlines the permittivity model parameters of Eq. (26) for some characteristic material of this class. The TO and LO phonon frequencies are accompanied by their corresponding free-space wavelengths, λ_{TO} and λ_{LO}. The representation of the reststrahlen band in terms of free-space wavelength is helpful for gauging the relevant feature-size ranges for platforms functional in this spectrum. We will therefore include such representation for all materials in the subsequent tables, 1 through 5 that follow.[8] While the subject of this review is how to utilize the reststrahlen band for photonic applications, we remark in passing that for some applications the reststrahlen band may need to be avoided. For example, CaF_2 and BaF_2 are popular as IR transparent materials, in which cases they are utilized for spectral regions away from their reststrahlen band.

Table 1: Ionic crystals: permittivity model parameters corresponding to Eq. (26) for some common ionic crystals.

Mat.[a]	ε_∞	l	$\omega_{\mathrm{TO}}\times10^{12}$ (rad/s)	$\omega_{\mathrm{LO}}\times10^{12}$ (rad/s)	λ_{TO} (μm)	λ_{LO} (μm)	$\gamma\times10^{12}$ (rad/s)
NaCl	2.22	1	30.90	50.37	60.96	37.40	1.20
LiF	1.04	1	57.98	174.22	32.49	10.81	4.20
CaF_2	2.045	1	48.41	84.60	38.91	22.27	0.87
		2	61.78	67.56	30.49	27.88	21.62
BaF_2	2.16	1	34.66	60.86	54.35	30.95	0.69
		2	52.37	53.21	35.97	35.40	15.71

[a]Parameters are taken from: [80] for NaCl and LiF; [81] for CaF_2 and BaF_2.

4.2 Semiconductors: semi-insulating versus doped materials

4.2.1 Isotropic semiconductors

Heteropolar and polar covalent semiconductors comprise effective cation-anion pairs; so they may also exhibit IR active phonons, and hence PhPs. However, unlike the case of the insulating ionic crystals of Table 1, in general their permittivity response is not fully captured by the models of Section 3; these would be only appropriate for semi-insulating or undoped semiconductors. The full permittivity response of semiconductors must include the contribution of the free carriers typically showing a Drude response [19] to the macroscopic electric field. It can be reasonably assumed that the free carriers do not contribute to the local field experienced by the ions.[9] So the semiconductor's full permittivity response, $\varepsilon_{\mathrm{sem}}$, can be considered as the cumulative result of the electric-field induced motion of the ions and their bound electrons as if free carriers were not there and then the electric-field induced motion of the free carriers as if the ions and their bound electrons were immovable. In other words:

$$\varepsilon_{\mathrm{sem}} = \varepsilon_{\mathrm{ion}} + \varepsilon_{\mathrm{Drude}}, \tag{30}$$

where the ionic contribution $\varepsilon_{\mathrm{ion}}$ has the same expression as one of the models of Section 3 as appropriate per case;

Table 2: Ionic permittivity model parameters of widely-used semiconductors.

Sem.[a]	ε_∞	$\omega_{\mathrm{TO}}\times10^{12}$ (rad/s)	$\omega_{\mathrm{LO}}\times10^{12}$ (rad/s)	λ_{TO} (μm)	λ_{LO} (μm)	$\gamma_{\mathrm{TO}}\times10^{12}$ (rad/s)	$\gamma_{\mathrm{LO}}\times10^{12}$ (rad/s)
InP	9.61	57.21	64.99	32.93	28.99	0.66	0.66
InSb	15.7	33.91	36.17	55.56	52.08	0.57	0.57
GaAs	11.0	50.48	55.02	37.32	34.23	0.45	0.45
GaP	9.09	68.94	75.87	27.32	24.83	0.21	0.21
SiC*	6.7	149.37	182.52	12.61	10.32	0.90	0.90
ZnSe	5.4	39.00	46.34	48.31	40.65	0.70	0.70
AlN[b]	4.53	126.20	171.79	14.93	10.96	1.13	1.70
GaN[b]	5.35	105.48	140.52	17.86	13.40	3.20	3.20

[a]Parameters are for $N=1$ and the model of Eq. (26) (if $\gamma_{\mathrm{LO}}=\gamma_{\mathrm{TO}}=\gamma$) or the model Eq. (28); they are taken from: [34] for InP; [85] for InSb; [86] for GaAs; [74] for GaP; [87, 88] for SiC (*6H/α-II); [89] for ZnSe; [90] for AlN; [91] for GaN.
[b]Please refer also to Table 3 for AlN and GaN.

8 In Tables 1 through 5: $\lambda_{\mathrm{TO}}=2\pi c/\omega_{\mathrm{TO}}$, $\lambda_{\mathrm{LO}}=2\pi c/\omega_{\mathrm{LO}}$, shown in units of μm. All parameters refer to room-temperature parameters.

9 The free carrier screening length is of the order of several lattice constants and also the electrons move much faster than the more inert ions [82].

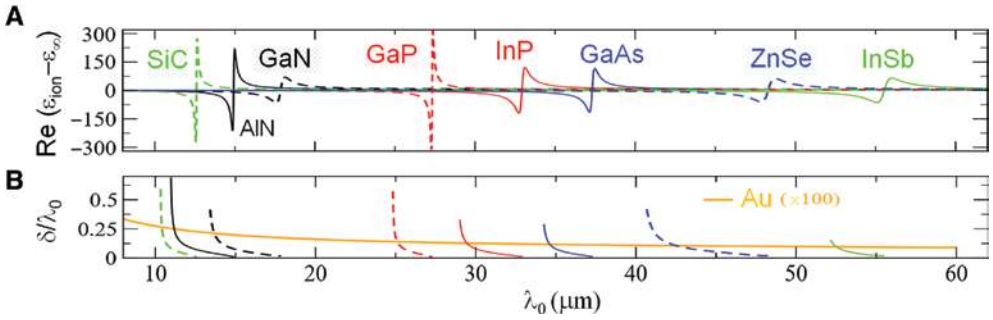

Figure 6: PhP permittivity and skin depth of widely-used semiconductors.
(A) Ionic response of the permittivity (real part) without the bound-electron contribution, i.e. $\mathrm{Re}(\varepsilon_{\mathrm{ion}}-\varepsilon_{\infty})$, versus the free-space wavelength, λ_0, for different semiconductor material (for AlN and GaN which are anisotropic the response for electric field $\perp$ to the *c*-axis is shown). (B) Corresponding skin depth, δ, scaled with the free-space wavelength, λ_0 (shown only within the respective reststrahlen bands with $\mathrm{Re}(\varepsilon_{\mathrm{ion}})<0$). The bold orange line represents the respective value for Au, multiplied by a factor of 100 to aid the comparison.

$\varepsilon_{\mathrm{Drude}}$ represents the Drude permittivity response of the free carriers, i.e.:

$$\varepsilon_{\mathrm{Drude}}=-\frac{\omega_p^2}{\omega(\omega+i\gamma_p)}, \tag{31}$$

where ω_{p} represents the plasma frequency[10] given by [20, 59, 83]:

$$\omega_{\mathrm{p}}=\sqrt{\left(\frac{N_{\mathrm{e}}}{m_{\mathrm{e}}^*}+\frac{N_{\mathrm{h}}}{m_{\mathrm{h}}^*}\right)\frac{e^2}{\varepsilon_0}}. \tag{32}$$

For generality the contribution of both types of carriers, electrons and holes, is taken [84] in Eq. (32) with respective carrier densities N_{e} and N_{h} and effective masses m_{e}^* and m_{h}^*; e is the electron charge, ε_0 the vacuum permittivity and γ_p the decay-rate/damping constant of the free-carriers motion.[11] The Drude response should be suitably adapted to account for cases where contributions from multiple valleys or sub-bands are relevant (e.g. see [20]).

In Table 2 we show some examples of widely used semiconductor material and the parameters relevant to their PhP permittivity response, $\varepsilon_{\mathrm{ion}}$. The parameters refer to the model of Eq. (26) (with $N=1$) except for the case of AlN that requires the model of Eq. (28) (with $N=1$). In Figure 6A, we plot the real part of the ionic permittivity response but without the bound electron contribution, i.e. $\mathrm{Re}(\varepsilon_{\mathrm{ion}}-\varepsilon_{\infty})$, for the materials and model parameters of Table 2. We observe the PhP responses of the different semiconductors cover a wide IR spectral range from about 10 μm to 60 μm. We also show in Figure 6B the related skin depth, δ, scaled with the free-space wavelength λ_0 along with the skin-depth value for Au (solid orange line), – multiplied with a factor of a hundred for an easier comparison. We observe high PhP related skin-depth values for all semiconductors, much higher than the skin-depth of Au. Thus, semiconductors in the reststrahlen band are ideal material for strong IR light-matter interactions.

The examples of Table 2 and associated models capture the photonic responses of most semiconductors. Semiconductor alloys tend to show the vibrational resonances of their constituents typically leading to photonic responses that can be described with the multi-pole models of Eqs. (26) and (28) [20]. For small gap or zero-gap semiconductors, as for example, HgTe, the full picture is more involved [92, 93] as the intra- and inter-band transitions spectrally overlap with the PhP regime and contribute to the permittivity response; these fall out of the scope of phenomena and applications in this review. Furthermore, some semiconductors show directional dependent responses that we discuss later.

Table 3: Anisotropic PhP responses of AlN and GaN: the ionic permittivity parameters for electric field parallel to the *c*-axis (optical axis) are shown here; the corresponding ones for electric field perpendicular to the *c*-axis were given in Table 2.

Sem.[a]	ε_∞	$\omega_{\mathrm{TO}}\times10^{12}$ (rad/s)	$\omega_{\mathrm{LO}}\times10^{12}$ (rad/s)	λ_{TO} (μm)	λ_{LO} (μm)	$\gamma_{\mathrm{TO}}\times10^{12}$ (rad/s)	$\gamma_{\mathrm{LO}}\times10^{12}$ (rad/s)
AlN	4.72	114.90	167.64	16.39	11.23	1.51	2.07
GaN	5.35	100.40	140.14	18.76	13.44	3.20	3.20

[a]Parameters correspond to the models of Eq. (26) [if $\gamma_{\mathrm{LO}}=\gamma_{\mathrm{TO}}=\gamma$] or Eq. (28) for $N=1$; these are taken from: [90] for AlN and [91] for GaN.

10 Note: some authors define the plasma frequency by dividing with an additional factor $\sqrt{\varepsilon_\infty}$.
11 The same damping constant, γ_p, is assumed for both electron and holes; however, in general this might not be the case.

4.2.2 Anisotropic semiconductors

The permittivity models of Eqs. (26) or (28) may unwittingly imply that the ionic photonic responses are independent of the propagation direction. This is not true; in materials with crystallographic anisotropy the TO phonon will depend on the direction of the electric field inside the material. These anisotropic materials still follow the aforementioned models as appropriate but with different parameters for electric field oriented along different crystallographic directions [94, 95]. Typically, they are uniaxial media [96] with their *c*-axis coinciding with the optical axis.

SiC(6H) shows a small anisotropy per [97] but has been predominantly treated as an isotropic PhP material [87, 98–102] with the parameters of [88] which are the ones shown in Table 2. On the other hand, SiC (4H) is typically considered as an anisotropic PhP material [97, 103] with the anisotropy coming in large part from the anisotropy of the high-frequency permittivity ε_∞ [97]. The nitride semiconductors of Table 2, AlN and GaN, are also anisotropic with the most significant anisotropy

Table 4: Anisotropic PhP responses of some widely used photonic materials.

Material[a]	E-field	ε_∞	l	$\omega_{TO}\times10^{12}$ (rad/s)	$\omega_{LO}\times10^{12}$ (rad/s)	λ_{TO} (μm)	λ_{LO} (μm)	$\gamma_{TO}\times10^{12}$ (rad/s)	$\gamma_{LO}\times10^{12}$ (rad/s)
α-Quartz	⊥ to *c*-axis	2.356	1	231.12	231.57	8.15	8.13	25.42	25.42
			2	219.07	219.53	8.60	8.58	1.31	1.31
			3	201.93	228.85	9.33	8.23	1.43	1.43
			4	150.13	153.59	12.55	12.26	1.35	1.35
			5	131.30	131.79	14.35	14.29	1.58	1.58
			6	84.76	98.42	22.22	19.14	0.76	0.76
			7	74.22	79.24	25.38	23.77	0.52	0.52
α-Quartz	|| to *c*-axis	2.383	1	229.81	230.34	8.20	8.18	34.47	34.47
			2	203.43	230.26	9.26	8.18	1.40	1.40
			3	146.55	149.59	12.85	12.59	1.47	1.47
			4	101.53	101.66	18.55	18.53	4.06	4.06
			5	95.88	96.88	19.65	19.44	1.34	1.34
			6	93.24	105.36	20.20	17.88	0.84	0.84
			7	68.56	77.73	27.47	24.23	0.96	0.96
Sapphire	⊥ to *c*-axis	3.077	1	72.52	73.01	25.97	25.80	0.62	0.58
			2	82.71	90.73	22.77	20.76	0.58	0.36
			3	107.18	118.58	17.57	15.89	0.89	1.11
			4	119.35	170.77	15.78	11.03	0.94	2.77
Sapphire	|| to *c*-axis	3.072	1	74.88	96.23	25.16	19.57	1.00	0.21
			2	109.71	165.97	17.17	11.35	0.57	2.90
VO_2	⊥ to α_M-axis	10.0	1	35.60	36.55	52.91	51.54	0.43	0.43
			2	50.86	77.13	37.04	24.42	3.56	3.56
			3	58.39	76.14	32.26	24.74	2.92	2.92
			4	64.04	66.25	29.41	28.43	1.54	1.54
			5	95.12	108.87	19.80	17.30	6.66	6.66
			6	113.02	137.49	16.67	13.70	8.36	8.36
			7	133.74	134.74	14.08	13.98	8.02	8.02
VO_2	|| to α_M-axis	9.7	1	42.85	43.07	43.96	43.73	0.86	0.86
			2	53.68	62.15	35.09	30.31	3.22	3.22
			3	61.03	66.88	30.86	28.16	1.10	1.10
			4	66.87	88.79	28.17	21.22	5.35	5.35
			5	73.93	77.65	25.48	24.26	2.22	2.22
			6	90.04	90.96	20.92	20.71	7.20	7.20
			7	99.83	103.12	18.87	18.27	4.49	4.49
			8	131.86	133.54	14.29	14.11	7.25	7.25

[a]The parameters correspond to the model of Eq. (26) [i.e. when $\gamma_{LO}=\gamma_{TO}=\gamma$] or Eq. (28).; these are taken from: [104] for α-quartz, [79] for sapphire, i.e. α-Al_2O_3 and [105] for VO_2 (insulating monoclinic phase [106]).

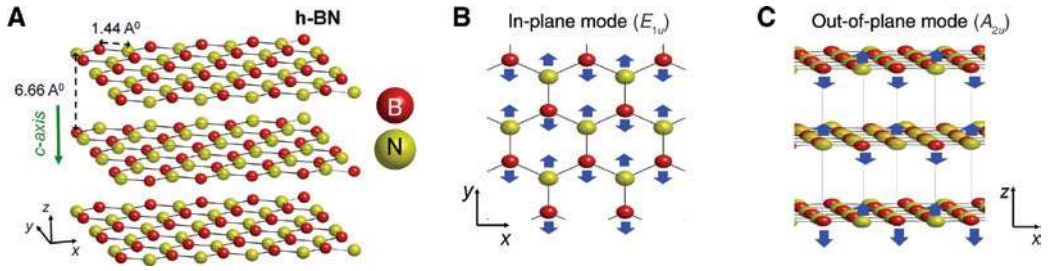

Figure 7: Structure and IR active phonon modes of hBN.
(A) The hBN vdW crystal (atomic spacings taken from [126]). (B) [(C)] The IR-active in-plane (E_{1u}) [out-of-plane (A_{2u})] phonon modes for hBN.

contributed by the TO phonon frequency. Table 3 complements Table 2 in capturing their full directional PhP response.

4.3 Other anisotropic PhP material

Aside from the semiconductors of Section 4.2.2, other widely used materials in photonics with an anisotropic PhP response are quartz [104], sapphire [79] and vanadium oxide (VO_2) [105, 106]. Their permittivity model parameters are given in Table 4, where we observe these materials possess multiple PhP resonances. The anisotropy in TO phonon frequency underpins the existence of extreme, hyperbolic, photonic responses as we discuss in more detail in Section 5.2 and drives a strong interest towards materials with this property. Furthermore, VO_2 has additional interest as a phase-transition material [107] offering tunability by switching on or off PhP responses (see Section 8.5).

One particular material, hexagonal boron nitride (hBN), has received a recent heightened attention for IR applications because of its anisotropic PhP responses [108–125]. While in principle the exotic hyperbolic modes exist in all uniaxial PhP material, what sets hBN apart is the degree of TO-phonon-frequency anisotropy leading to a much broader bandwidth where these modes are available. hBN is a van der Waals (vdW) crystal (see Figure 7A). The much looser connection between the hexagonal-lattice planar sheets with weaker vdW forces significantly red-shifts the out-of-plane IR-active phonon frequency [see Eq. (22)] and accordingly the TO phonon frequency [see Eq. (23)]. We show hBNs in-plane (⊥ to the *c*-axis) and out-of-plane (|| to the *c*-axis) IR active phonons in Figure 7B and C, respectively, designated with Mulliken's notation [127] that is common in phonon/Raman spectroscopy communities. In Table 5 we list hBN's PhP permittivity model parameters. Indeed, we observe a tremendous anisotropy between the in-plane (⊥ to the *c*-axis) and out-of plane (|| to the *c*-axis) PhP responses of hBN. To quantify such anisotropy in the observed PhP responses we introduce the PhP anisotropy factor, f_{anis}, defined as:

Table 5: Anisotropic PhP responses of vdW crystals: hBN and α-MoO_3.

ε_∞[a]	$\omega_{TO}\times10^{12}$ (rad/s)	$\omega_{LO}\times10^{12}$ (rad/s)	λ_{TO} (μm)	λ_{LO} (μm)	$\gamma\times10^{12}$ (rad/s)
hBN:	E-field	⊥ to	*c*-axis		
4.87	257.50	303.27	7.32	6.21	0.94
hBN:	E-field	|| to	*c*-axis		
2.95	147.50	155.97	12.77	12.08	0.75
α-MoO_3:	E-field	in-plane	|| to	[100]	
4.0	154.46	183.09	12.20	10.29	0.75
α-MoO_3:	E-field	in-plane	|| to	[001]	
5.2	102.66	160.30	18.35	11.75	0.75
α-MoO_3:	E-field	|| to	*c*-axis	([010])	
2.4	180.45	189.11	10.44	9.96	0.38

[a]The parameters correspond to the model of Eq. (26) for $N=1$; they are from [108–112] for hBN (see discussion in text) and [128] for α-MoO_3.

$$f_{\text{anis}} = 2\frac{\omega_{\text{TO},\perp} - \omega_{\text{TO},\parallel}}{\omega_{\text{TO},\perp} + \omega_{\text{TO},\parallel}}, \tag{33}$$

where $\omega_{\text{TO},\perp}$, $\omega_{\text{TO},\parallel}$ are the respective TO-phonon frequencies for electric field perpendicular and parallel to the *c*-axis. hBN has a PhP anisotropy factor, f_{anis}, of more than 50% compared to only ~10% and ~5% f_{anis} for AlN and GaN, respectively. Large f_{anis} values indicate a wider spectral band where indefinite uniaxial photonic responses [25] and associated exotic hyperbolic modes can be available as we discuss in Section 5.2.1.

While the model parameters of the Tables 1–4 are typically obtained by fitting to experimental reflectivity spectra, for hBN this process would be highly non-trivial. Available experimental data highly depend on the polycrystalline nature of the samples, leading to substantial

overestimation of the decay constants, as well as on domain off-plane orientation defects [126], leading to mixing between the on- and off-plane responses [126]. As a result the older experimentally extracted model parameters [126] may not be appropriate for single crystalline hBN systems of current interest [108]. It appears that similar but different permittivity parameters have been used in different works with no clear consensus. We choose to indicate in Table 5 the model parameters that have been adopted by many current works [109–112], following the ones of Dai et al. [108]; i.e. ω_{TO}, ω_{LO}, from [126], ε_{∞} values from the ab-initio calculations of [129] and γ, from the observed decay of exotic guided modes in hBN by Dai et al. [108].

Another emergent vdW material for PhP-based photonics is α-MoO_3 (see Figure 8A). Due to its crystal structure this material has a very rich vibrational response. We focus our discussion here on the main three IR active modes relevant to photonic applications in the free-space wavelength range around 10 μm–20 μm [128]. The vdW planes connect same-species atoms, O-atoms in this case; so the out-of-plane PhP response comes only from the asymmetric stretching vibration of the Mo-O(1) bond (B_{2u} mode) (see Figure 8B). This is not too different from the B_{3u} asymmetric-stretching mode of the Mo-O(3) bond; so both are spectrally very close. However, the O(2) forms two bonds of significantly unequal length with the adjacent Mo atoms [133], which significantly red-shifts the associated IR active mode (mode B_{1u}) with respect to the B_{2u} and B_{3u} modes. As a result α-MoO_3 has a biaxial PhP response (see also Section 5.2.2) with a large in-plane anisotropy (plane $\perp$ to the stacking direction [010]). To be specific, an analogous PhP anisotropy factor, $f_{\text{anis–IP}}$, can be defined for the in-plane (IP) PhP modes as:

$$f_{\text{anis–IP}} = 2\frac{\omega_{\text{TO},x} - \omega_{\text{TO},z}}{\omega_{\text{TO},x} + \omega_{\text{TO},z}}, \tag{34}$$

where x and z define the two in-plane symmetry directions of α-MoO_3, [100] and [001]. The in-plane PhP anisotropy factor for α-MoO_3, $f_{\text{anis–IP}}$, is about 40% indicating the possibility for broad spectral availability of indefinite biaxial photonic responses [25] that we discuss in Section 5.2.2.

Thus, hBN and α-MoO_3 are PhP material of high current interest because they exhibit an extreme PhP anisotropy, out-of-plane and in-plane, respectively; this anisotropy leads to unusual photonic responses that we discuss in more detail in Section 5.2. But this tells only part of the story. The weaker cross-plane vdW forces also allow for straightforward fabrication of few layer hBN [108] or α-MoO_3 thereby unlocking extreme possibilities for molding EM waves with PhPs in atomic scale materials. In the section that follows, we go beyond the examples of hBN and α-MoO_3 and discuss the importance and implications of 2D and quasi-2D PhP materials for phonon-polaritonics.

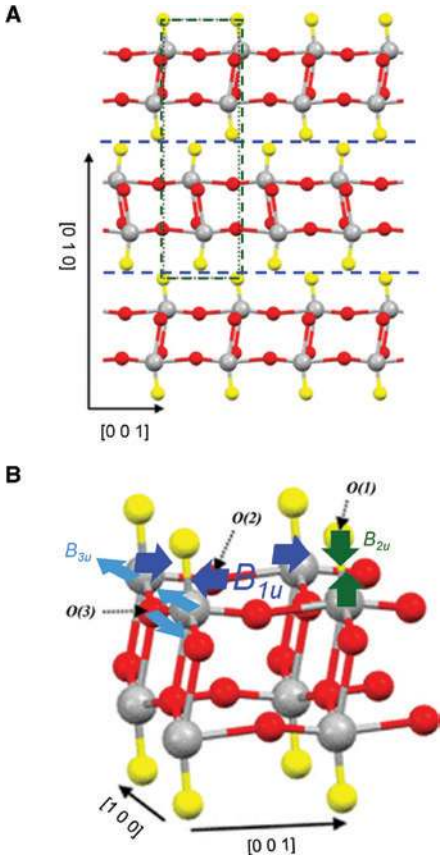

Figure 8: Structure and IR active phonon modes of α-MoO_3. (A) The unit cell of the α-MoO_3 structure is designated with the green-dotted box. The blue-dashed lines enclose one α-MoO_3 layer that interacts with the adjacent layers with weaker vdW forces. (B) Magnified part of an α-MoO_3 layer: the three in-equivalent O atoms and associated asymmetric stretching vibrations are indicated. [Figure reprinted (adapted) with permission from [130]. Copyright (2013) American Chemical Society.] Note: The stretching modes designation has been added in accordance with the modes reported in [131]. The notation of the in-plane directions has been altered to be consistent with [128] and [132].

4.4 PhPs in the "flatland": 2D and quasi-2D PhP materials

2D materials have broken boundaries in material science and are a subject of intense research efforts both for their appealing electronic [134] and photonic [135, 136] properties. Going a step further, Geim and Grigorieva [137] envisioned that 2D material could be used as building-block "legos" that can be joined together plane-by-plane to make materials with new properties. These super-2D

materials are structurally stable as the material planes are held together with vdW forces in the absence of dangling bonds; hence their name vdW heterostructures [134, 137]. When it comes to PhPs these vdW heterostructures can provide an avenue to make atomic-level designer PhP material with tailored functional spectral ranges of their IR-active phonons (see schematic of Figure 9). To the best of our knowledge these atomic-level designer PhP materials, comprising dissimilar adjacent vdW planes, are uncharted territory at present. Their possibility has only been envisioned by Caldwell and Novoselov in [142] and briefly discussed in [143], where they were referred to as "crystalline hybrids".

One could argue that for these atomic-level designer materials the effective in-plane PhP responses might bear some similarities to the case of semiconductor alloys, especially as the intra-plane bonds are much stronger than the inter-plane forces. Nevertheless, interlayer charge transfer effects as well as the charged-phonon effect [138–141] that depend on the particular materials involved may cause completely unexpected responses. The resulting effective permittivity could be very different from the one hypothesized from simpler classical arguments as above. In addition, new IR-active phonons for an electric field perpendicular to the atomic planes could emerge, as a result of possible new IR-activated lattice vibrations in the cross-plane direction. Most certainly, these vdW heterocomposites open exciting bottom-up design routes to new materials with different PhP spectral ranges. vdW heterocomposites could form a very promising research direction for on-demand IR light control with atomically-thin materials.

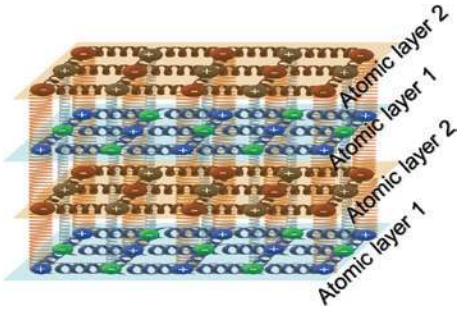

Figure 9: Atomic-level designer PhP materials.
A basic conception of a vdW heterostructure involving two fictitious atomic layer materials. The in-plane IR-active phonons emanate from the lattice vibrations within each atomic layer (depicted as springs along the cyan and orange planes). Quantum effects could cause counter-intuitive and completely unexpected responses [138–141]. In addition, new cross-plane IR-active phonons (vertical springs) could emerge with the appropriate choices of the atomic material layers.

Although vdW hetero-composites have not been studied in the context of creating new effective photonic responses, vdW crystals supporting IR-active phonons have been interfaced with other 2D material with the purpose of achieving strong coupling between their respective native EM modes (e.g. see [123]). The underlying physics principles of these systems are to tune/modulate the EM wave propagation properties by a strong interaction between the EM wave modes supported in each sub-system. As these do not relate to changing inherent material properties we will review these phenomena in detail in Section 9 where we discuss hybrid platforms. The vast possibilities of these hybrid platforms can have a strong impact on future photonic applications. This has stimulated a strong interest in the community for realizing 2D/quasi-2D PhP materials.

Many of the research efforts have mainly focused on hBN. Monolayer [124, 144] and few layer hBN [108, 122, 125] have been reported and studied for its PhP-related hyperbolic responses by various groups [see also Sections 6.1.2 and 6.1.4]. Detailed studies of atomic-scale (few-layer) hBN [108, 122] have shown that exotic hyperbolic-type of guided modes survive even for atomic-scale thickness [albeit with a modified guided wave dispersion, $\omega(k)$]. This fact provides evidence that the strong TO phonon anisotropy, in the respective planar and *c*-axis directions, is maintained for atomically-thin hBN [108]. Indeed, [108] reports an excellent agreement between theoretical predictions and experimental results on the PhP guided-mode even for sub-5 nm thicknesses. Furthermore, Raman spectra for the similar in-plane Raman-active phonon mode in monolayer and few-layer hBN have confirmed a small shift only for the optical phonon frequency [144]. These results in combination imply that the TO phonon frequency for the in-plane IR-active mode (Figure 7B) is fairly robust to finite-size effects.

This is likely not the case for the TO phonon mode across vdW planes of hBN, where the atoms oscillate along the *c*-axis as depicted in Figure 7C. In the extreme case of monolayer hBN, no out-of-plane vibration modes would be possible. Thus, the TO phonon mode along the *c*-axis completely disappears [123] in hBN monolayers along with the associated extraordinary hyperbolic photonic responses (see also Section 5.2.1). The significant interest in mid-IR photonics with atomically-thin hBN calls for further experimental evaluation of finite-size effects when thicknesses approach the atomic scale. Characterization of the in-plane and out-of-plane TO-phonon modes and their associated photonic responses for atomically-thin hBN will be extremely important in elucidating such effects.

As an insulator [145], hBN may have a limited potential for achieving PhP-based structures or devices with actively tunable responses. Semiconductor 2D/quasi-2D PhP materials would be highly desirable for tunable IR devices. Atomically-thin semiconductors that have been most frequently discussed as 2D PhP material, at least theoretically [146–148], are the transition metal dichalcogenides (TMDs). TMDs are also vdW crystals allowing their realization in a monolayer or few-layer form via mechanical exfoliation [149]. Semiconducting TMD monolayers are typically in the 1H phase (hexagonal/trigonal prismatic arrangements) [149, 150] as depicted in Figure 10A, which is the standard thermodynamically stable phase for sulfides and selenides of group VI TMDs [150]. Although tellurides of group VI TMDs are typically semi-metallic following octahedral (trigonal anti-prismatic) arrangements [150], a recent work has shown that it is possible to mechanically exfoliate $MoTe_2$ monolayers onto Si/SiO_2 substrates in the semiconducting hexagonal phase [151].

What is remarkable about these 2D semiconducting TMDs is that even in the monolayer form they may support extraordinary hyperbolic modes, in stark contrast to monolayer hBN which loses the hyperbolic photonic response in its monolayer form. The monolayer-TMD hyperbolic photonic response is a direct consequence of the trigonal prismatic atomic arrangement, allowing out-of-phase vibrations between the transition metal and chalcogenide atoms not only along the atomic planes (see Figure 10B) but also in the direction perpendicular to the atomic planes, i.e. along the *c*-axis (see Figure 10C). The bandwidth of such hyperbolic photonic response depends on the spectral separation of the in- and out-of plane IR-active phonons. To the best of our knowledge, experimental characterization for the permittivity responses of monolayer TMDs in the mid/far-IR is not yet available. However, first-principle calculations based on density functional theory (DFT) can predict the resonant frequencies/wavelengths for the IR-active phonon modes of Figure 10B and C [146–148], which are related to the TO phonon frequency, ω_{TO} [see Eq. (23)].

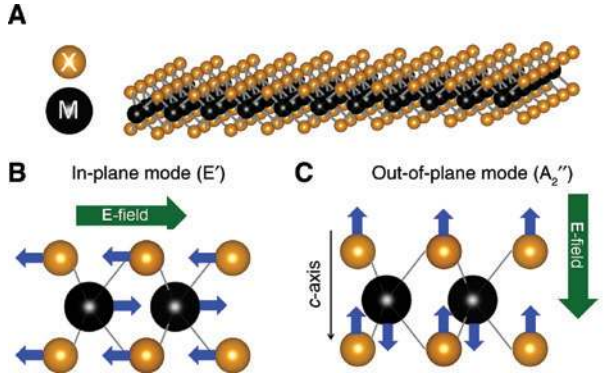

Figure 10: Structure and IR active phonons of TMDs.
(A) A monolayer TMD in hexagonal (trigonal prismatic) arrangement (1H-phase). M denotes the transition metal atoms and X the chalcogenide atoms. (B) [(C)] Side view of the monolayer TMD indicating the phonon vibrations induced by an electric field ⊥ [|||] to the *c*-axis, i.e. the in-plane (out-of-plane) IR-active phonon modes (E′) [(A_2'')].

We list in Table 6 the IR-active phonon mode wavelengths for certain semiconducting monolayer TMDs (1H-phase), calculated from DFT at the Γ point [146–148], i.e. at zero phonon wave vector, $q \sim 0$ (see discussion in Section 3). We observe from Table 6 that the typical anisotropy between the in-plane and out-of-plane IR-active phonon frequencies is about 20%. Although not exactly equal, the anisotropy between the in-plane and out-of-plane IR-active phonon frequencies relates to the PhP anisotropy factor, f_{anis}, of Eq. (33) (see also footnote *c* in Table 6). Thus, a more moderate f_{anis} of about 20% is expected for TMDs, much smaller than that of hBN, which has an f_{anis} of about 50%, but still much larger than that of the traditional semiconductors of Table 3, which have an f_{anis} of about 10% or less. Such significant PhP anisotropy factor makes hexagonal 2D TMDs excellent media for hyperbolic photonic responses with the added advantage of gate tunability, which is not available in hBN. The PhP modes listed in Table 6 would be of course lossy, just like in hBN and other semiconductors, because of the relaxation to the low-lying phonon bands

Table 6: Out-of-plane (A_2'') and in-plane (E′) IR-active phonon wavelengths, λ_{ph}, of 1H monolayer TMDs.

TMD mat.[a,b]	λ_{ph} (μm) (Out-of-plane: A_2'') E || *c*-axis	λ_{ph} (μm) (In-plane: E′) E ⊥ *c*-axis	IR-active Phonon Anisotropy[c]
MoS_2	21	26	21%
*WS_2	23	28	20%
*$MoSe_2$	29	36	22%
*WSe_2	34	43	23%
$MoTe_2$	35	43	21%

[a]Parameters are taken from: [146] for MoS_2 and WS_2; [147] for $MoSe_2$ and WSe_2; [148] for $MoTe_2$.
[b]For the materials designated with a (*) the IR-active phonon mode wavenumbers have been extracted from related graphs. All wavenumbers have been converted to wavelengths in μm (free-space) and rounded-off to the nearest integer value.
[c]This is the anisotropy in the wavelength/frequency of the IR-active phonon mode. It is related and gives an indication for the PhP anisotropy factor defined in Eq. (33), f_{anis}. Nevertheless, it is not quite equal to f_{anis}, as the IR active phonon frequencies and the TO phonon frequencies are somewhat different [see Eq. (23) with Ω_{free} representing the IR-active-phonon frequency].

[146]. The actual PhP resonances in experimental samples may show a slight spectral shift depending on the isotopic purity of the TMD samples which affects the mass of the ionic oscillators [152].

In reviewing 2D materials as PhP media, special attention should be given to graphene, the first ever 2D material, discovered in 2004 [153]. Since graphene's discovery there have been numerous reports of its unique electronic properties and vastly tunable photonic response. However, graphene has not received much attention for its potential as a PhP material. Although graphene is comprised of only carbon atoms, it can actually support optical phonon modes [154]. This is because graphene has two atoms within the hexagonal Bravais-lattice unit cell which can vibrate out-of-phase. However, because of the lack of charge asymmetry between the two atoms of the unit-cell basis, it is not possible for EM waves to trigger their out-of-phase vibrational modes. In other words, monolayer graphene supports optical phonon modes, which however are not IR active; hence PhPs cannot be supported on monolayer graphene.

The situation is a bit different in Bernal-stacked bilayer graphene (*AB* stacking) (see Figure 11). The structural asymmetry of the *AB* stacking, together with electron hopping between the two layers, breaks the equivalence between the A and B sub-lattice carbon atoms, leading to a dipole moment in each Bravais lattice unit cell. This dipole moment would enable coupling to incident light, i.e. it would make the optical phonon-mode IR active. Indeed, Kuzmenko et al. [138] observed a PhP response for Bernal-stacked bilayer graphene. However, the experimentally observed PhP showed a much higher oscillator strength, which in turn implied a three-orders-of-magnitude higher dipole moment from what would be expected from classical arguments [139].[12] Also, the observed optical response, as manifest in the measured conductivity, exhibits a spectral profile that is characteristic of Fano resonances [156].

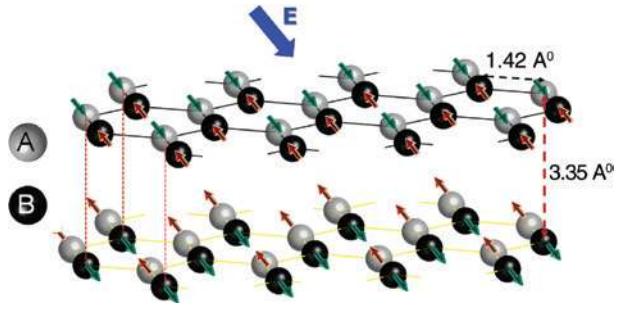

Figure 11: Structure and IR active phonons of Bernal-stacked graphene (*AB* stacking).
The IR active lattice vibration mode (E_u mode) is shown. The effective dipole moment between sub-lattice atoms, *A* and *B* is acquired by a combined effect of inter-layer charge-transfer and phonon interaction with electron-hole pairs (charged-phonon effect) [140, 141]. The atomic spacings are taken from [155].

This IR active response can be strongly tuned by gating the Bernal-stacked bilayer graphene [138, 139]. These curious results of [138] were interpreted within the quantum mechanical framework of charged-phonon theory adapted for the graphene-bilayer system [140, 141]. In particular, based on this theory the "bare" optical phonon mode via interactions with the allowed electron-hole excitations acquires a large dipole moment. Hence, this "dressed" phonon has a much stronger effective dipole moment [139–141, 157] than the one predicted by the asymmetry alone, thus leading to a prominent IR active phonon mode observed in related experiments [138, 157–159]. In other words, this "dressed" phonon effect gives rise to a PhP with much higher oscillator strength. At the same time, the phonon part of this discrete PhP mode interacts with the electronic continuum via electron-phonon scattering, which leads to a Fano profile for the conductivity response [138–141, 157].

Similar effects can occur also in trilayer graphene [160] with the *ABC*-stacking demonstrating a much stronger tunability with the gate voltage. Other explored 2D PhP materials include *AB*-stacked black-phosphorus-carbide (b-PC) [161], with IR-active phonons at frequencies similar to the IR-active spectrum graphene. 2D b-PC shows in-plane optical anisotropy and a Fano spectral response; the latter does not appear to be fully understood at present and could be related to similar effects that were observed in bi-/tri-layer graphene.

We discussed previously α-MoO_3, a vdW transition metal oxide (TMO) [162], that also exhibits in-plane anisotropic PhPs [128, 132]; α-MoO_3 with atomic-scale thickness has been recently realized and studied for its PhP responses [162]. This emergent PhP material is expected to attract increasing interest as an atomically-thin bi-axial material [96] with extreme in-plane anisotropy and IR activity covering a spectral range between ~10 μm and 20 μm [128]. Finally, phosphorene, i.e. a monolayer of black phosphorus has been shown to support IR-active phonons at wavelengths around 20 μm [163].

Summarizing, IR-active phonons in 2D materials, and associated PhP photonic responses, cover a large part of the IR spectrum between free-space wavelengths of 6 μm and 45 μm. In Figure 12 we outline such spectral coverage

12 The oscillator strength, defined in Eq. (27), is connected to the static permittivity, ε_s [see Eq. (24)]. Hence, higher oscillator strength values could imply a higher charge *Q* and thus a higher dipole moment of the ion pair [see Eq. (20)]

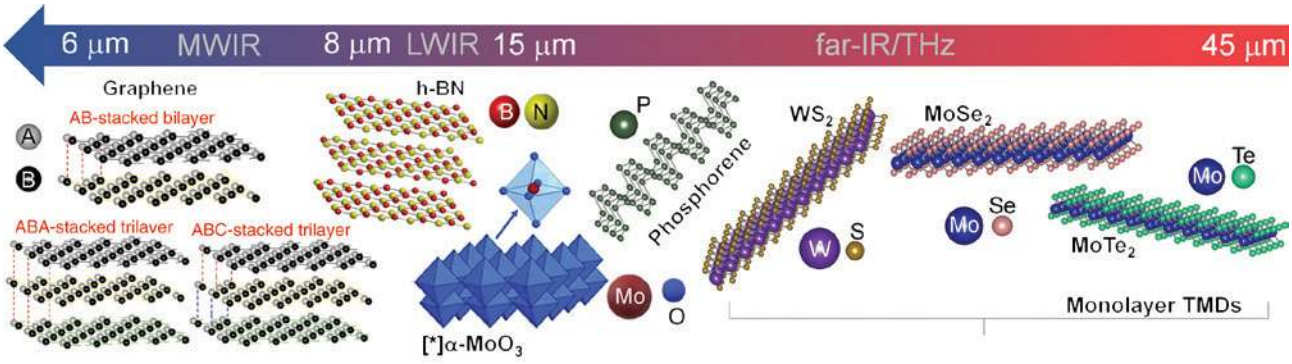

Figure 12: Atomically-thin PhP materials.
The PhP responses of the examples shown fully cover the spectral regime between 6 μm and 45 μm (free-space wavelength). The material schematics are placed in order of decreasing wavelength (from right to left) of the associated IR active optical phonons (see top arrow; note: wavelength scale is not linear/proportional). [*] The α-MoO_3 schematic is adapted from [164] via CC BY 4.0 license (see link at https://creativecommons.org/licenses/by/4.0/).

in IR activity with representative 2D materials discussed in this section. The 2D material are arranged from right to left in order of decreasing wavelength of their IR-active optical phonons.

5 Distinct photonic responses in the PhP regime

5.1 Photonic responses in isotropic PhP material

To visualize the photonic responses in the PhP regime we consider a general fictitious material, with permittivity following the model of Eq. (26) that broadly covers many PhP materials. We consider realistic model parameters within the range of the parameters for the semiconductors of Table 2. In particular, we take $\omega_{LO}=1.3\omega_{TO}$, $\varepsilon_\infty=6$, and $\gamma=0.008\omega_{TO}$ ($N=1$). We plot in Figure 13 the real and imaginary part of the permittivity, versus the frequency, ω, that has been scaled with the TO frequency, ω_{TO}. We can identify three distinct types of photonic responses that underpin distinct design principles for platforms relevant to IR applications.

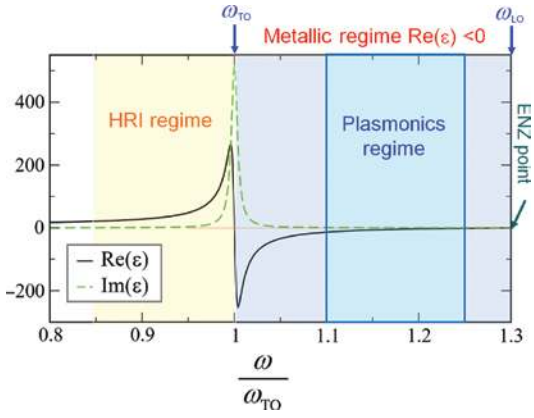

Figure 13: Photonic responses of isotropic PhP media.
A general example of the permittivity response, $\varepsilon(\omega)$, from the model of Eq. (26) (with $N=1$) is shown representing a fictitious material yet with realistic parameters within the range of widely-used semiconductor material. The blue-shaded region indicates the metallic spectral regime with $Re(\varepsilon)<0$. Within this spectral regime, the blue rectangle designates the regime where the PhP permittivity takes values typical of visible-light plasmonics with noble metals. The yellow-shaded region designates the spectral regime of high permittivity, and so high refractive index (HRI). The ENZ point at $\omega=\omega_{LO}$ is also shown.

5.1.1 IR plasmonic-like responses

Within the reststrahlen band, between the TO phonon frequency, ω_{TO}, and LO phonon frequency, ω_{LO}, the photonic response is metallic with $Re(\varepsilon)<0$ (blue-shaded region in Figure 13). The pertinent permittivity range for obtaining powerful light-molding capabilities like that of noble metals in the visible [2], that we call here plasmonic phenomena, does not have hard limits and depends on the particular geometries and sizes as well as the permittivity of the host media. Surely, large negative permittivity values correspond to smaller relative skin-depths and so do not support a strong light-matter interaction. Generally, plasmonic effects can be expected in the spectral range where the permittivity takes values roughly between $\varepsilon=-15$ and $\varepsilon=0$; note that permittivity values of $\varepsilon=-1$ and $\varepsilon=-2$ represent the quasi-static conditions for surface SPP and particle-plasmon respectively assuming the host medium is vacuum [1]. Now, permittivity values between $\varepsilon=-15$ and $\varepsilon=0$ are available for a large portion of the reststrahlen band wherein IR plasmonic-type effects can be

explored. We discuss the basic building blocks of such IR plasmonic-type effects in Section 6. These plasmonic-like responses are also relevant to constructing IR hyperbolic metamaterials that we discuss in Section 7.1.1. We designate the spectral region for IR plasmonic-like responses in Figure 13 with the blue rectangle.

5.1.2 IR high-refractive-index (HRI) responses

We also observe with the example medium of Figure 13 that the permittivity, and thus the refractive index, can reach very high values for frequencies close to but smaller than ω_{TO}. We designate the region of a high-refractive index response with the yellow shaded area. However, there are some differences with pure dielectrics as a significant material loss is present (non-zero imaginary part in the permittivity). We discuss to what extend can this photonic response be utilized for photonic paradigms inspired from all-dielectric photonics in Sections 6.2.1 and 7.2.1. This response is also relevant to constructing IR magnetic metamaterials discussed in Section 7.1.3.

5.1.3 IR ENZ responses

ENZ photonic environments have been associated with enhancing non-linearity [45, 165] and absorption [166, 167] as well as modulating antenna resonances and their collective effects [168, 169]. Naturally, PhP material have an epsilon-near-zero (ENZ) response near the LO phonon frequency and can thus bring such ENZ phenomena in the IR spectrum. Recent examples include [168] and [170] reporting on tailoring of antenna resonances and emission with PhP-enabled ENZ substrates. Also [171] reports a strong angular and spectrally-selective emission mode of an ultrathin PhP film at the ENZ point associated with the Berreman mode [172].

We designate in Figure 13 the ENZ point for the example medium we have considered. Generally, the quality of the ENZ response is determined by the accompanying imaginary part where the real-part of the permittivity is near-zero; lower imaginary part of the permittivity, at the ENZ point, generally corresponds to systems with lower losses and responses with near-zero refractive index. In particular, at the ENZ point with $\mathrm{Re}(\varepsilon) \sim 0$ the full complex refractive index is:

$$n + i\kappa = \sqrt{\frac{\mathrm{Im}(\varepsilon)}{2}}(1+i) \tag{35}$$

An ENZ response at the LO phonon frequency, ω_{LO} is attained assuming:

$$x = \frac{\omega_{LO}\gamma}{\omega_{LO}^2 - \omega_{TO}^2} \ll 1. \tag{36}$$

This condition is reasonably satisfied by most single-oscillator PhP materials; in multiple-oscillator materials the off-resonance contributions by other oscillators may overshadow the ENZ response of the corresponding LO phonon frequency. For single-oscillator material the permittivity becomes, at the LO phonon frequency:

$$\varepsilon(\omega_{LO}) = [0 + O(x^2)] + i[0 + O(x)] \tag{37}$$

Eq. (37) implies that the quality of the ENZ response is better for single-oscillator material with smaller x values as given by Eq. (36).

5.2 Photonic responses in anisotropic PhP material

As we discussed in Section 4 some material, e.g. AlN, GaN, hBN, sapphire, insulating-phase VO_2, semiconducting TMDs, α-MoO_3 etc., have anisotropic PhP responses, with hBN dominating recent attention [108–125, 173]. hBN owes such increased attention to its being a vdW crystal that not only leads to an extreme PhP anisotropy but also brings such anisotropy in atomically-thin structures. α-MoO_3 is another emergent PhP material attracting significant recent interest [128, 132, 162] due to its inherent in-plane PhP anisotropy that enables a biaxial response. Also a vdW crystal, α-MoO_3 can be made into 2D/quasi-2D structures. Next, we discuss how these anisotropic PhP responses, of uniaxial or biaxial type, translate to distinct types of supported photonic modes by these material.

5.2.1 Uniaxial PhP material

Most anisotropic PhP material would be of uniaxial type, with different permittivity responses, $\varepsilon_{\parallel}$ and $\varepsilon_{\perp}$, for an electric field parallel and perpendicular to the c-axis; thus the c-axis is also the optical axis. Propagating EM modes through uniaxial PhP media have been studied since the 1960s [174]. In analogy to bulk EM modes supported in uniaxial crystals [96] these modes were called ordinary PhPs (O-PhPs) and extraordinary PhPs (EO-PhPs) with respective wave dispersion relations:

$$k_x^2 + k_y^2 + k_z^2 = \varepsilon_{\perp}\frac{\omega^2}{c^2}, \tag{38}$$

and

$$\frac{k_x^2+k_y^2}{\varepsilon_{||}}+\frac{k_z^2}{\varepsilon_{\perp}}=\frac{\omega^2}{c^2}. \tag{39}$$

It was not however until the rise of the metamaterials field, and in particular until after the conception of hyperbolic metamaterials [47, 48], that the truly "extraordinary" properties of the EO-PhPs were uncovered. Metamaterials spurred the design of man-made EM meta-atoms yielding vast and unusual effective EM responses not readily available in nature, including media with permittivity of opposite sign along different directions (indefinite media) [25]. Later, in 2010, da Silva et al. [175], noticed that these curious indefinite permittivity responses are actually available in natural quartz by virtue of its anisotropic PhP response. In particular, within a distinct frequency regime, quartz has $\varepsilon_{||}\varepsilon_{\perp}<0$, causing a hyperbolic dispersion form for the EO-PhPs (Eq. 39) and in turn negative refraction [176, 177], a phenomenon which up to that point had been associated only with man-made artificial metamaterials [178]. An example from [179] of such EO-PhP-enabled negative refraction in natural crystals is shown in Figure 14; this negative refraction also enables superfocusing effects [176, 179] similar to those reported with artificial hyperbolic metamaterials [47, 48].

Generally an arbitrary EM wave incident on an anisotropic uniaxial crystal with a general interface cut couples to both ordinary and extraordinary modes [80, 96]; for PhP crystals this would mean both O-PhPs and EO-PhPs would simultaneously couple leading to birefringent PhP propagation [174]. However, in most frequently encountered situations, the interface plane is perpendicular to the *c*-axis.

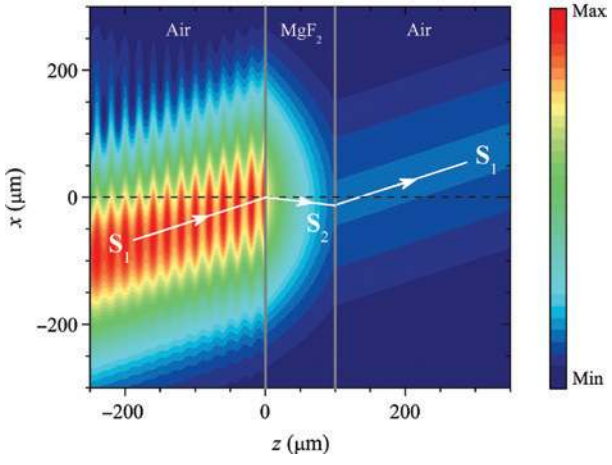

Figure 14: PhP media as natural "metamaterials". Negative light refraction at a MgF2 slab enabled by its indefinite permittivity response of $\varepsilon_{||}\varepsilon_{\perp}<0$ emanating from anisotropic PhPs. (After [179]; reprinted from [179]. Copyright 2013 with permission from Elsevier.)

For this particular interface cut, the O-PhP and EO-PhP modes decouple with O-PhP modes becoming accessible only by S-polarized waves (left panel of Figure 15A) and EO-PhP modes becoming accessible only by P-polarized waves (right panel of Figure 15A) [80, 96].

In Figure 15B we summarize the corresponding wave dispersion forms for these cases, determined from Eqs. (36) and (37) as applicable per case; we consider all the possible permittivity value combinations available throughout the PhP regime with widely used materials. We depict in Figure 15C the graphical representations[13] of the distinct possible wave dispersion forms. Both types of the hyperbolic dispersion forms, type I and type II (both seen in Figure 15C), are available for different frequency ranges. These are the familiar dispersion forms observed in hyperbolic metamaterials [47, 48, 80, 182]. Aside from negative refraction and superfocusing effects reported in [175, 176, 179] these PhP-enabled hyperbolic dispersions in natural PhP materials can bring to the IR many of the other exotic effects associated with hyperbolic metamaterials, such us dark-field imaging or a Purcell enhancement [48, 182] from IR quantum dots [183].

5.2.2 Biaxial PhP material

Certain materials may additionally exhibit in-plane anisotropy, i.e. the PhP response is also anisotropic in the plane perpendicular to the stacking direction, as for example, in α-MoO_3 (see also Figure 8 and Table 5). The photonic responses of biaxial media is much richer and a lot more complex than that of uniaxial media. Similar to uniaxial media, the wave dispersion of waves propagating in a non-magnetic biaxial medium, is determined by Maxwell's equations mandating that the supported modes must satisfy Det[A]=0, with [A] being a 3×3 matrix with elements:

$$A_{ii}=\varepsilon_i\frac{\omega^2}{c^2}-\sum_{j=1}^{3}(1-\delta_{ij})k_j^2, \tag{40}$$

with $i=1, 2, 3$ and

$$A_{ij}=k_ik_j, \quad \text{with} \quad i\neq j, \tag{41}$$

and $i, j=1, 2, 3$; δ_{ij} is Kronecker's delta and the running indices correspond to the Cartesian directions as: $1\leftrightarrow x$, $2\leftrightarrow y$, and $3\leftrightarrow z$.

However, unlike the case of uniaxial media, the wave dispersion relations, $\omega(k)$, resulting from solving the

13 These graphical representation of the wave dispersion are generally known as k-surfaces [96], surfaces of wave-normals [180], or equi-frequency surfaces (EFSs) [181].

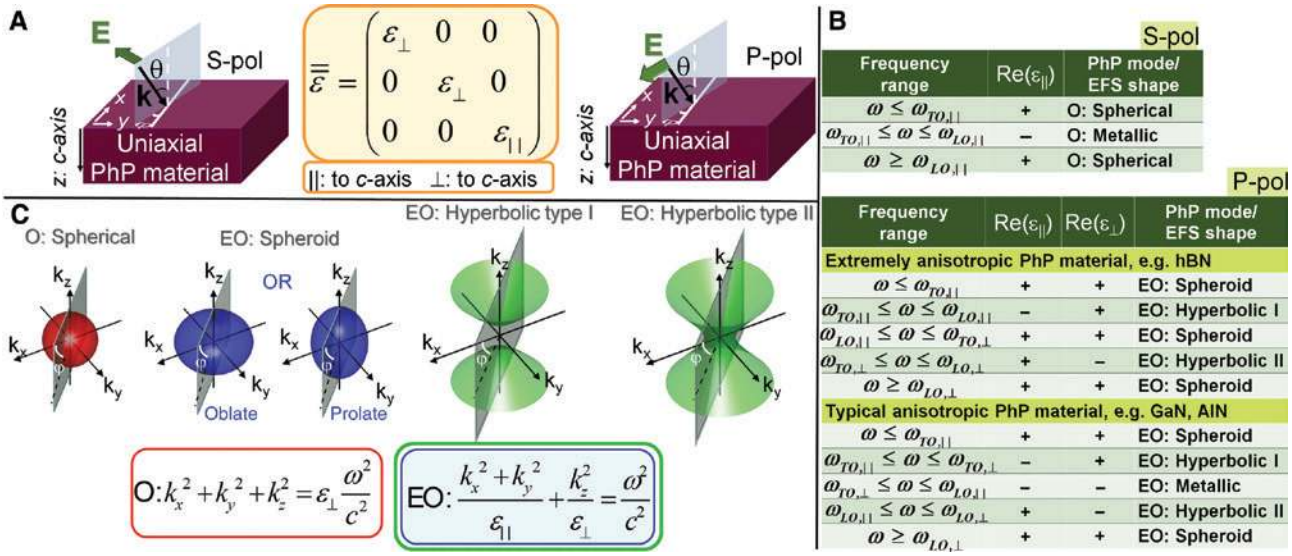

Figure 15: Photonic responses for uniaxial PhP media.
(A) S- and P-polarized waves incident on a uniaxial PhP medium with interface cut ⊥ to the *c*-axis. The anisotropic permittivity tensor is also indicated. (B) S-and P-polarized waves couple respectively to the ordinary (O) and extraordinary (EO) waves. The tables designates the possible distinct photonic wave mode responses, arising in different frequency regimes determined by the respective TO and LO phonon frequencies in the directions || and ⊥ to the *c*–axis. (C) Graphical representation in wave-vector space, (k_x, k_y, k_z), of the characteristic wave modes outlined in (B) (EFS/surfaces of wave normals). These are determined by the respective dispersion relations for the O-waves and EO-waves (equations in boxes) for the applicable signs of the permittivity values in each case (material loss is neglected). The gray planes represents the plane of incidence, as seen also in (A). The modes designated as metallic in (B) are not drawn here; these refer to highly lossy wave solutions similar to plane waves in metals.

condition above cannot be represented by simple expressions like Eqs. (38) and (39). Given the vast possibilities in biaxial PhP responses, it goes beyond the scope of this review to identify all possible photonic mode forms that are supported. To give the reader a flavor for the unconventional possibilities with PhP biaxial media we showcase an example in Figure 16 that corresponds to $\varepsilon_x < 0$, $\varepsilon_y > 0$, $\varepsilon_z > 0$ with $\varepsilon_y \neq \varepsilon_z$. This case is entirely possible with α-MoO_3 in the spectral range $\lambda_0 \sim$ 11–12 μm (free-space wavelength). The corresponding depicted equi-frequency surface (EFS) shows an unusual shape resembling type I hyperbolic dispersion joined with an ellipsoidal dispersion. This unusual EFS has been recently reported for α-MoO_3 (see [128]). The EFS of Figure 16 depicts all available modes in the entire wave vector space for a particular frequency, ω. However, the associated electric field corresponding to a certain wave vector **k** at a certain frequency, ω, must also be examined to determine whether the mode is or is not accessible by a certain light excitation.

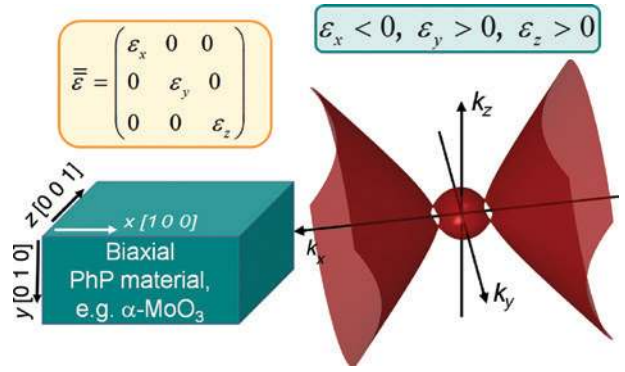

Figure 16: Example of an indefinite photonic response of a biaxial PhP medium.
The indicated crystallographic directions, associated with the *x*, *y*, *z* directions correspond to the case of α-MoO_3 (see also Figure 8). The EFS/surface of wave normals depicts a general possible case with in-plane indefinite permittivity response, i.e. with $\varepsilon_x \varepsilon_z < 0$. In the depicted case: $\varepsilon_x < 0$, $\varepsilon_y > 0$, $\varepsilon_z > 0$ with $\varepsilon_y \neq \varepsilon_z$.

In Section 5 we reviewed the different types of photonic responses enabled by PhPs. In the following section we review the geometries which in synergy with PhP responses lead to confined EM modes which form the backbone of many of the diverse reported IR PhP-based capabilities and phenomena.

6 The essential building blocks of IR phonon-polaritonics

The vast range of amazing phenomena in the field of plasmonic optics all share a common thread: they are build upon

the highly-confined optical states at either metal/dielectric planar interfaces or around metallic nanoparticles. Conversely, the essential building blocks relevant to IR photonics would be highly confined photonic modes around planar interfaces or micron/sub-micron particles of pertinent IR material like alternative IR plasmonic materials [3, 56, 57] or PhP material which is the subject of this review. Therefore, we review in this section the fundamentals of localized modes around PhP material interfaces or PhP particles that set the foundations of the phonon-polaritonics field and present examples of current related research, new phenomena and applications that have emerged. We also discuss the similarities and difference of PhP-based localized modes with their plasmonic counterparts. Furthermore, we highlight new types of localized modes emerging from exotic EM dispersions, such as hyperbolic EM dispersions, which have no counterpart in the optical regime with natural material. The latter have been attracting increasing attention and are expected to play a central role in PhP-based IR photonics.

6.1 Confined PhP modes at planar interfaces and ultrathin films

6.1.1 Ordinary surface phonon-polaritons (O-SPhPs)

Localized quasi-bound EM modes[14] may be supported at the surface of PhP materials, with $\mathrm{Re}(\varepsilon)<0$. These modes share similar characteristics to SPPs [38] and are so analogously called surface phonon polaritons (SPhPs) [18, 184].[15] The dispersion relation for SPhPs, relating their lateral wave vector k_x, with their frequency ω, is the same as for SPPs given by [38]:

$$k_x = \sqrt{\frac{\varepsilon(\omega)\varepsilon_d}{\varepsilon(\omega)+\varepsilon_d}}\ \frac{\omega}{c}, \tag{42}$$

with c being the speed of light, $\varepsilon(\omega)$ the complex frequency-dependent permittivity response of an isotropic PhP medium and ε_d the permittivity of the dielectric material interfacing with the PhP medium.[16]

SPhPs are supported within the PhP gap/reststrahlen band where $\mathrm{Re}(\varepsilon)<0$. The black-solid line in Figure 17A is a graphical representation of the dispersion relation of Eq. (42) for an example SPhP mode supported at the interface between air and the PhP material of Figure 13. The frequency ω is scaled with the TO phonon frequency, ω_{TO}, and the real part of the wave vector is represented with the dimensionless quantity $\beta=\mathrm{Re}(k_x)c/\omega$; thus the vertical brown-dashed line at $\beta=1$ represents the lightline. Furthermore, the electric-field landscape (x-component) for the mode designated with the green rectangle, shown in the upper part of Figure 17, suggests a well-confined surface mode around the interface of significant propagation range.

The quality of confinement and propagation range are typically in competition for surface waves at interfaces of lossy materials, with $\mathrm{Re}(\varepsilon)<0$ [186, 187]. Different quantifiable measures, i.e. figures of merit (*FOM*), to capture the performance of these confined surface waves have been hitherto introduced. Here we consider for the SPhP a *FOM* with the intent to capture simultaneously both the confinement quality and propagation sustainability of the mode, given by:

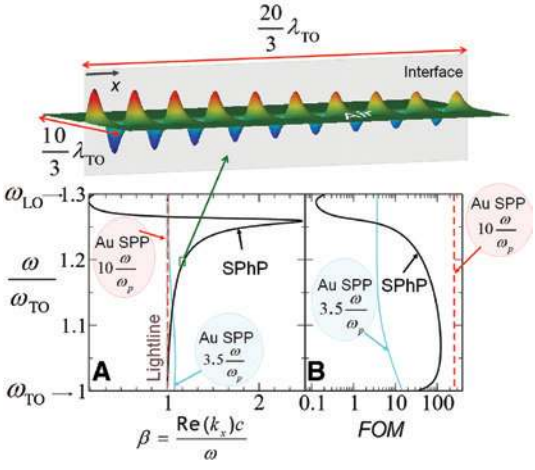

Figure 17: Surface phonon polaritons (SPhPs) at plane interfaces. (A) SPhP dispersion (black solid line) at the interface of air and the PhP medium of Figure 13. $\mathrm{Re}(k_x)$ is represented with the dimensionless parameter β after scaling its value with the free-space wave vector ω/c. The upper panel shows the x-component of the electric-field for the mode designated with the green rectangle. (Note, $\lambda_{TO}=2\pi c/\omega_{TO}$.) The SPhP dispersion is compared with the SPP dispersion at an air-Au planar interface at two different frequency regions; around telecomm wavelengths (red-dashed line) and in the green-blue part of the visible spectrum (cyan line). (B) Figure of merit (*FOM*) [see Eq. (43)] for the SPhP mode (black-solid line) compared to the *FOM*s of the SPP mode at the two frequency regimes that were shown in A.

14 These show a decaying rather than an evanescent wave profile from the interface. Purely bound EM modes with an evanescent wave profile are only an idealized scenario at interfaces between materials of opposite permittivity and no dissipation [23].

15 We do not discuss Zenneck waves [185] here which may be supported for the spectral range with $\mathrm{Re}(\varepsilon)>0$; Zenneck waves are also quasi-bound surface waves showing much looser confinement though.

16 The square root represents the complex-valued square root.

$$FOM = \frac{|\mathrm{Im}(k_y)|}{\mathrm{Im}(k_x)}. \quad (43)$$

The defined *FOM* represents the ratio of the distance the surface wave travels along the interface until its electric field strength drops by a factor of $1/e$ over the perpendicular-to-the-interface distance at which the electric field strength drops by a factor of $1/e$ inside the dielectric medium. The *FOM* value from Eq. (43) should be used in conjunction with the dispersion relation to characterize the overall quality of an SPhP mode. For example, dispersion regions which are very close to or above the lightline certainly signify a weak confinement to the interface; thus any relatively high *FOM* values in these region only signify a large propagation range. The *FOM* for the SPhP of Figure 17A is shown in Figure 17B with a black solid line.

To obtain a sense of how SPhPs relate to SPPs, we also include in Figure 17A and B the dispersion relation and *FOM*-values respectively of an SPP mode supported at the air-Au interface (see also Figure 2A), where realistic optical parameters are used for Au (see Figure 1). To make such comparison, first the SPP's frequency ω is scaled with the plasma frequency, ω_p. As we discussed in Section 2, SPPs in the mid- and longwavelength IR are essentially grazing waves loosely confined at the interface. So we find it useful to compare the IR SPhPs with their SPPs counterparts but around telecomm and visible frequencies. For this reason, the SPP's ω/ω_p value is shown in Figure 17A after being multiplied by a suitable factor yielding, respectively, the red-dashed curves, representing the SPP mode around telecom frequencies, and the cyan curve, representing the SPP mode around visible frequencies.

It appears the SPPs on the surface of Au are generally closer to the lightline in comparison to SPhPs. As with respect to *FOM* values, the telecom-wavelength SPP modes show a high *FOM*- but that would mean only a low propagation loss as confinement is ultra-weak for the telecom SPP mode which essentially follows the lightline. The more confined visible SPP mode is clearly outperformed by its SPhP counterpart for most of the reststrahlen band range. This superior performance of the SPhPs modes, in terms of strong confinement and low propagation loss, occurs

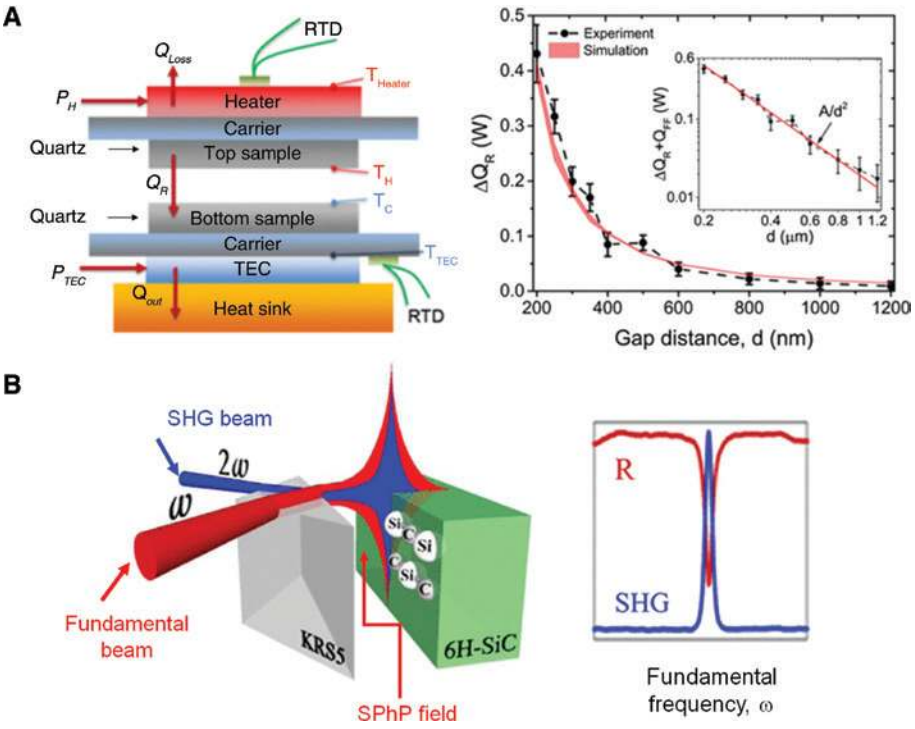

Figure 18: Examples of SPhP-enabled phenomena.
(A) SPhP-enabled enhanced near-field heat transfer: (Left) heat transfers from a hot to a cold quartz plate, separated by a distance, *d*; (Right) Observation of a $\propto 1/d^2$ scaling law, a signature of near-field heat transfer facilitated by the SPhP. (Reprinted with modification with permission from [194] (see link at https://journals.aps.org/prl/abstract/10.1103/PhysRevLett.120.175901). Copyright 2018 American Physical Society.) (B) SPhP-enabled enhanced second harmonic generation (SHG): (Left) The fundamental beam couples via an ATR prism to a SPhP mode supported at the air-SiC interface. (Right) The coupling to SPhP manifests itself as a dip in the reflectivity spectrum (red line), giving rise to a SHG signal that out-couples on the other side of the prism (blue line). (Reprinted (adapted) with permission from [195]. Copyright 2017 American Chemical Society.)

around the middle of the reststrahlen band away from the TO and LO phonon frequencies. Actually, it is interesting to observe that unlike its SPP counterpart, the SPhP mode runs through a broader range of β values,[17] even crossing through the lightline into β values less than 1 at frequencies approaching the LO phonon frequency, ω_{LO} [Foteinopoulou S, unpublished]. It is worth mentioning that such SPhP dispersion crossing into the above-the-lightline region was first experimentally observed in the 1970s for the case of α-quartz [189, 190]. However, as the *FOM* shown in Figure 17B attests, high performing SPhPs are associated with the portion of the dispersion curve below the lightline and around the middle of the reststrahlen band.

SPhPs have been utilized to enhance near-field heat transfer [191–194] (see also Figure 18A), as well as to enhance SHG signals [195] (see Figure 18B). Theoretical calculations have also shown [196] that SPhPs can enhance the inherent thermal conductivity of a material. SPhPs substrates may enhance coupling with biomolecular vibrational modes and are thus relevant to SEIRA spectroscopy [197]. Moreover, when SPhPs are accessed with an attenuated total internal reflection (ATR)-type prism [1] ultra-sharp peaks can emerge in the reflectance spectra that can be used for the IR analog [198] of surface plasmon resonance (SPR) sensors [199]. Pairing up SPhP modes with other physical systems such as phase-change materials [107, 200, 201], 2D materials with gate-tunable properties [135, 136], or plasmonic [2, 186, 187] and dielectric [15] waveguides, as well as IR active media such as quantum dots [183] and quantum wells including strained superlattices [202], unleashes many more possibilities for harnessing IR light pertinent to integrated and/or tunable infrared devices, IR imaging systems [37, 203] and quantum-well IR photodetectors [202, 204]. We discuss more examples of these hybrid systems in Section 9.

6.1.2 Extraordinary surface phonon-polaritons (EO-SPhPs)

The indefinite anisotropic PhP responses, as discussed in Section 5.2, unlock possibilities for unprecedented types of confined EM modes at PhP material interfaces; this is an unfamiliar territory with no analogue in plasmonics where metals have isotropic negative permittivity responses. The most trivial case involves a uniaxial PhP material in a regime where the permittivity is negative both along and in the normal plane to the *c*-axis. In such a case, assuming the interface is along the normal to *c*-axis plane, a minor adjustment to Eq. (42) accounts for such anisotropy and determines the dispersion for the SPhP modes; this can be seen, for example, in [205], where SPhPs are excited on the surface of 4H-SiC for a frequency within the associated reststrahlen bands of both the parallel and normal to the *c*-axis directions [97].

However, the in-plane anisotropy present in certain bi-axial PhP material, such as α-MoO_3, introduces entirely new avenues for confining EM waves at PhP-material surfaces beyond the familiar SPPs, such as Dyakonov surface waves [206]. Dyakonov type surface waves are also supported in uniaxial hyperbolic PhP material for an interface cut along a plane that includes the optical axis [207]. Actually, very recently such atypical surface confined waves have been theoretically predicted and experimentally observed on the edge face of an hBN-crystal flake excited by the near-field emanating from a scattering-scanning near-field optical microscopy s-SNOM[18] tip (see mode designated as hyperbolic surface polariton (HSP) in Figure 19 after [209]). Alfaro-Mozaz et al. [210] also report antenna behavior for an hBN sub-micron strip that is enabled by hybridization of the HSP modes between the edge faces that lead to sharp resonances of a quality factor, *Q*, of around 100. Moreover, the guided modes on the hBN strips have shown to couple strongly with the molecular vibrations of organic semiconductors making this system ideal for SEIRA spectroscopy [211].

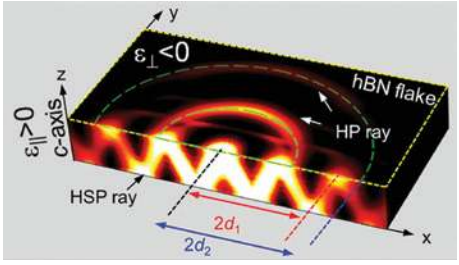

Figure 19: Two types of confined modes at an hBN flake with $\varepsilon_x=\varepsilon_y<0$ and $\varepsilon_z>0$.
(I) SPhPs confined on the edge-face-air boundary, i.e. || to the *xz*-plane; these emanate from the indefinite, hyperbolic, dispersion on the *xz*-plane and were termed as hyperbolic surface plasmons (HSPs) in [209]. (II) Hyperbolic GPhPs, emanating from type II hyperbolic dispersion within the hBN flake; these propagate along the *y*-direction yielding a fringe pattern on the top face (and bottom face not shown here) and were termed as hyperbolic polaritons (HPs) in [209]. The different distance between the field maxima at the edge and top face as indicated manifests the co-existence of these two distinct modes. [Reprinted (adapted) with permission from [209]. Copyright (2016) American Chemical Society.]

17 β is essentially the modal refractive index [188].

18 s-SNOM is a popular technique for mapping the near-field landscapes in the IR and has been widely used in probing PhP-based confined modes. See related review article of [208].

6.1.3 Ordinary guided PhPs (O-GPhPs): Fuchs-Kliewer interface polaritons

Different types of guided waves may arise at PhP-material thin films. An ultrathin slab comprising an isotropic PhP-material will behave, in the reststrahlen band, analogously to an insulator-metal-insulator waveguide [39, 186] in visible/near-IR frequencies. In particular, the SPhP modes at each interface will hybridize splitting into two bonding/anti-bonding-like branches just like SPs in plasmonic thin films [39]. These coupled SPhP modes at the interfaces of finite slabs were first studied by Fuchs and Kliewer [212] and are thus sometimes referred to as Fuchs-Kliewer phonons or Fuchs-Kliewer interface polaritons. Ultra-thin PhP-materials slabs supporting such Fuchs-Kliewer polaritons can operate accordingly as IR waveguides. Moreover, the Fuchs-Kliewer polaritons can be utilized for IR dark-field transfer analogous to that in Pendry's silver lens, also known as the poor man's superlens [213]. Actually, this phenomenon has been confirmed by Taubner et al. in [214] where a SiC slab supporting SPhPs functions as an IR superlens.

6.1.4 Extraordinary guided PhPs (EO-GPhPs)

The indefinite permittivity responses [25] in natural PhP material showcased in Figures 15 and 16 underpin exotic IR guided modes with unconventional dispersion relations. Let us assume a thin slab waveguide with an indefinite uniaxial, i.e. hyperbolic, PhP response with in-plane permittivity, $\varepsilon_{\perp}<0$, and permittivity parallel to the *c*-axis $\varepsilon_{\parallel}>0$. The dispersion relation for supported guided modes propagating along the plane with a complex wave vector k_t has been given as (after [108, 116, 215]):

$$k_t(\omega)=-\frac{1}{d\psi_i}\left[\tan^{-1}\left(\frac{\psi_i}{\varepsilon_{\perp}}\right)+\tan^{-1}\left(\frac{\varepsilon_{\text{sub}}\psi_i}{\varepsilon_{\perp}}\right)+\pi l\right], \qquad (44)$$

where $\psi_i=i\sqrt{\varepsilon_{\perp}}/\sqrt{\varepsilon_{\parallel}}$, ε_{sub} is the substrate permittivity and l represents the order of the supported guided mode. An example of such a hyperbolic GPhP is depicted in Figure 19; it is the mode with the fringed pattern on the planar face of the hBN flake designated as a hyperbolic polariton (HP) (after [209]).

The hyperbolic guided mode of Eq. (44) can be launched onto the PhP-material layer by scattering IR light onto an atomic force microscopy (AFM) tip and was observed for the first time in hBN by the Basov group [108] with IR imaging from s-SNOM [208]. The Basov group's pioneering work spurred numerous investigations aiming to further understand such curious guided modes in hBN, e.g. see [114, 116, 122, 209]. Recent reports on this unconventional guided mode include works that show that it can be also launched by scattering light onto the natural defects of the hBN flake such as folds [117] as well as its realization in suspended hBN as thin as 15 nm [215]. The suspended platform exhibits a clear advantage of reduced damping in comparison to the hBN-on-SiO_2 system [215]. The hyperbolic-type GPhPs in hBN stimulated a strong interest to explore these extraordinary guided modes in other PhP material. Very recently, previously unseen guided modes have been reported [128] in biaxial α-MoO_3; α-MoO_3 is anisotropic and can be indefinite by virtue of its PhP response on the interface plane (see also Figure 16).

These hyperbolic guided modes in hBN can be utilized for super-focusing/imaging [119, 120] as well as ultra-slow signal propagation [110, 121]. hBN guided modes have also been shown to boost the sensitivity of graphene photodetectors [216], an effect that may lead to high resolution IR imaging systems. The quality of the hyperbolic GPhP in hBN can be further tailored by controlling the Boron isotopic purity in the hBN sample. Specifically, processed hBN samples with either ^{10}B or ^{11}B isotopic purity were very recently utilized to achieve a substantially longer propagation range (lower loss) for the hyperbolic guided mode in comparison with the natural species [217].

6.2 Particle PhPs

Light incident on plasmonic nanoparticles may give rise to highly localized resonant modes that have been termed as particle plasmons [41], LSPs [40] or Mie plasmons [42, 43], because of the Mie-type light scattering involved [44]. Nanoantennae [41], high-Q Fano resonances for biosensing [218], aperture-less near-field optical microscopy [219] and spasers [220], etc. form only an indicative list of a plethora of fantastic effects and applications enabled by particle plasmons. Conversely, localized modes "molded" around micron-sized PhP particles can be the basis for shaping IR light for targeted IR applications; analogously we will refer to these modes as particle PhPs.

However, unlike particle plasmons, particle PhPs may arise from distinctively different material responses which are available in the PhP regime; these can range from plasmonic-like responses characteristic of noble metals in the visible spectrum to HRI responses (see Section 5.1 and Figure 13). Furthermore, indefinite uniaxial or biaxial responses (see Section 5.2 and Figures 15 and 16) are also available with PhP material. These responses do not have

any counterpart in dielectrics outside the PhP regime or metals. Thus, in the following we will be referring to particle PhPs as ordinary if connected to plasmonic-type or HRI isotropic photonic responses and as extraordinary if connected to indefinite anisotropic [25] PhP photonic responses as discussed in Section 5.2.

6.2.1 Ordinary particle PhPs

Just like the case of plasmonic nanoparticles, the resonant response of PhP microparticles to incoming light can be captured by the extinction efficiency, Q_{ext} [221], which is the extinction cross-section [44] normalized to the particle's cross-sectional area. The extinction efficiency involves the particle's response both in terms of scattering and absorption and so gives a more complete picture for the resonant response of particles comprising lossy photonic materials, such as PhP materials. The extinction efficiency sums up the effect of all possible resonant orders, that may be excited at the microparticle (multipoles). Assuming a plane wave of angular frequency, ω, is incident on a microsphere of radius R immersed in air (vacuum), the extinction efficiency, Q_{ext}, is equal to [44, 221–223]:

$$Q_{ext} = \frac{2c^2}{\omega^2 R^2} \sum_{n=1}^{\infty} (2n+1) Re(a_n + b_n), \tag{45}$$

with $n=1$ representing the dipolar resonant order, $n=2$ the quadrupolar resonant order and so on.

For each order the mode is a superposition of two characteristically different field distributions each having a strength represented by the coefficients a_n and b_n, determined by the EM boundary conditions at the sphere's surface.[19] Actually, a_n represents the strength of a field distribution having an electric field with a strong radial component (implying a strong surface charge density) and a magnetic field that is purely tangential. Conversely, the coefficient b_n represents the strength of a field distribution having a magnetic field with a strong radial component and an electric field that is purely tangential. Accordingly, a_n and b_n have been associated with an electric- and magnetic-type resonant response, respectively [223].

We plot in Figure 20A the extinction efficiency for an example case. We do so in order to showcase the existence of distinct types of ordinary particle PhPs emanating from the different isotropic photonic responses in the PhP regime: plasmonic-like and HRI responses, respectively. The particular example we consider here involves a microsphere made of the PhP material of Figure 13, with radius, R, equal to $0.065\,\lambda_{TO}$, with λ_{TO} being the transverse-optical phonon free-space wavelength. We observe two resonances, hence two particle PhPs: one within the plasmonic permittivity regime, that we will be referring to as the type A particle PhP, and one within the HRI regime, that we will be referring to as the type B particle PhP.

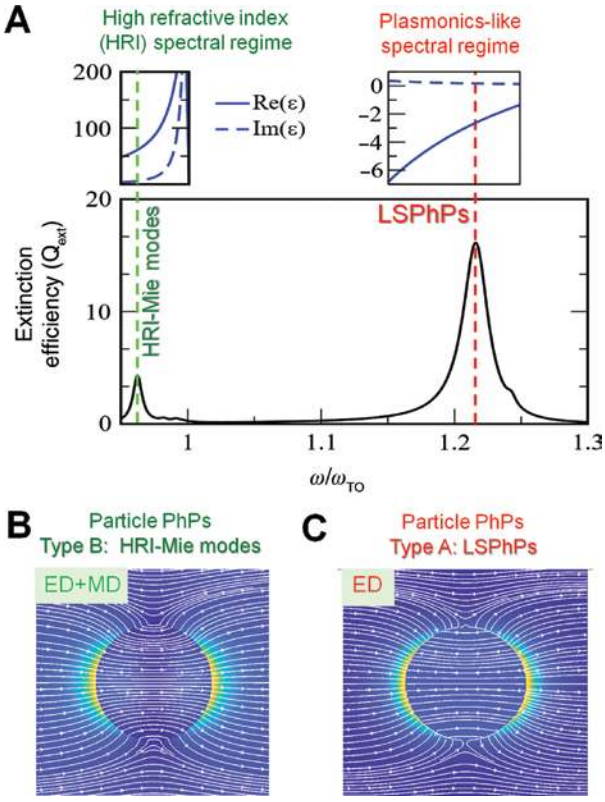

Figure 20: Ordinary particle PhPs.
(A) Extinction efficiency calculated from Mie theory [44] for a sphere with the permittivity of Figure 13 and radius equal to $0.065\lambda_{TO}$ where $\lambda_{TO} = 2\pi c/\omega_{TO}$. The dashed vertical lines designate the two particle PhP resonances: type A, i.e. an LSPhP mode and type B that is a high-refractive-index (HRI) Mie PhP mode. The two top insets show the permittivity of the microsphere around the respective spectral ranges of the two resonances. (B) Electric-field intensity, $|\mathbf{E}|^2$, and streamlines for the HRI-Mie PhP having a mixed electric-dipole (ED) and magnetic-dipole (MD) character. (C) Electric-field intensity, $|\mathbf{E}|^2$, and streamlines for the LSPhs of electric-dipole (ED) character.

The type A ordinary particle PhP is similar to the LSP; and hence is typically referred to as the localized surface phonon polariton (LSPhPs) [224–227]. Indeed, its dominant response comes from the dipolar electric-type term, a_1, yielding an electric field landscape shown in Figure 20C that resembles the familiar dipolar response of plasmonic nanospheres in the visible spectrum (see, e.g.

19 We follow here the notation adopted most widely in the literature (e.g. see [221–223]); in [44] a_n is designated as b_n^r while b_n is designated as a_n^r.

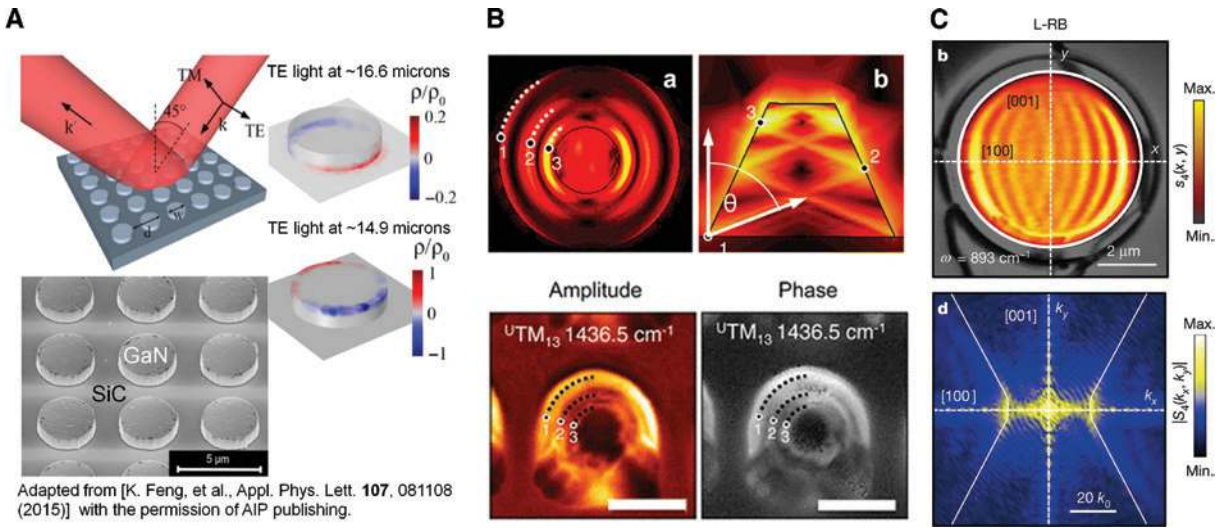

Figure 21: Experimentally observed particle PhPs.
(A) LSPhPs [Type A ordinary (O) particle PhPs] in GaN microdisks resting on a SiC substrate. The two dipolar modes depicted are excited at different free-space wavelengths and have enhanced fields at the top or bottom of the microdisk, respectively. This is because of the different corresponding dielectric environments affecting the resonance conditions. (Adapted from [224] with the permission of AIP publishing, see link at https://aip.scitation.org/doi/10.1063/1.4929502.) (B) EO particle PhPs at hBN sub-micron cones observed at: 7 μm. The unconventional photonic interference inside the hBN nanocone (top panels) stemming from hBN's hyperbolic dispersion yields characteristic hot rings on its surface at deep-subwavelength distances, which were experimentally observed with s-SNOM (bottom images) (scale bars are 300 nm). [Reprinted (adapted) with permission from [113]. Copyright 2016 American Chemical Society.] (C) EO particle PhPs at an α-MoO_3 microdisk at: ~11 μm. The observed deep-subwavelength fringe pattern (top panel) comes from the underlying indefinite biaxial permittivity response. The associated unconventional photonic dispersion (similar to the one of Figure 16) manifests itself in the associated Fourier transform (bottom panel). (Reprinted by permission from Springer Nature Customer Service Centre GmbH: Springer Nature-Nature [132]. Copyright 2018.)

LSP1 mode of Figure 2E). The observed LSPhP resonance is excited near the Fröhlich condition [1, 222].[20] This is expected given the deep-subwavelength size of the microsphere. Just like in the case of LSPs, as the microsphere becomes larger the electric dipolar resonance would occur increasingly further from the Fröhlich condition and an electric quadrupolar resonance would emerge. Eventually, for microsphere sizes of the order of the wavelength the near-field response to the incoming EM field involves multiple orders and both electric- and magnetic-type field distributions.

The type B ordinary particle PhP shown in Figure 20B resembles the Mie-resonant responses of dielectric particles [221]. For this particular example, the electric field involves contributions both from the electric dipole (ED) term, a_1, and the magnetic dipole (MD) term, b_1.[21] Therefore the type B particle PhPs may be referred to as HRI-Mie PhPs [228], in order to distinguish these from LSPhPs; however unlike pure dielectric Mie modes, these type B particle PhPs have a lossy character. In fact, the high extinction efficiency that is observed in Figure 20A is in large part a result of a high absorption efficiency, as opposed to a high scattering efficiency. HRI-Mie PhPs have not, thus far, been widely investigated.

Actually, to-date it is mostly type A particle PhPs, i.e. LSPhPs, that have been widely studied. Theoretical reports of LSPhs involve infinite or finite-height cylinders with circular, elliptical and rectangular cross-section cylinders [100, 229, 230] as well as disks [225]. The existence of LSPhs has been experimentally verified; in fact LSPhPs have been spectroscopically characterized and/or imaged in sub-micron pillars [226, 231], microdisks [224] (see Figure 21A) or nanoparticle clusters [227]. The field enhancements in LSPhP excitations may be utilized for thermal emission [86, 98, 100, 232], enhancing nonlinear phenomena such as second harmonic generation, for example, see [226] and in sensing platforms like SEIRA [197]. LSPhP properties can be further tuned by harnessing their collective interactions in a 2D array lattice [233], just like with lattice LSPs [218]. Finally, particle PhPs in SiO_2 microspheres have been shown to enable enhanced near-field heat transfer from the microsphere to a SiO_2 plane by coupling to the respective plane SPhPs [234]; likely both LSPhPs and HRI Mie PhPs contribute to this phenomenon in this case.

20 I.e. close to the frequency where $\varepsilon = -2$ as the host permittivity is 1 here.

21 The b_1 term is on-resonance; however the off-resonant value of a_1 is not small in this case.

6.2.2 Extraordinary (EO) particle PhPs

PhPs made available unconventional "metamaterial" photonic responses in natural material. As discussed in Section 5.2, permittivity may be indefinite [25] in PhP media, i.e. have a different sign in two of the crystallographic directions. The corresponding photonic dispersions can be extraordinary, of hyperbolic type or other curious complex shapes as in the case of the biaxial medium of Figure 16. Accordingly, the discovery of indefinite responses in PhP media [108, 175] brought out an entire exotic garden of related localized particle PhPs which are currently a subject of increased research attention. In this section we use the term of EO-particle PhPs to be inclusive of particle PhPs in any anisotropic PhP medium with corresponding EO, i.e. non-isotropic, photonic dispersions. However, truly unconventional resonant signatures not possible with isotropic particles appear to emerge only in certain instances of microparticles comprising indefinite PhP media.

For example, particle PhPs have been theoretically and experimentally studied in a bow-tie nanoantenna comprising anisotropic 4H-SiC with the purpose of achieving spectral selectivity of the SiC's emission spectrum. The observed resonant PhP modes in each triangular structure of the bow-tie nanoantenna resemble the multi-resonant response observed at the visible spectrum in triangular plasmonic particles [235]. Moreover hBN-disk dimers [173], with hBN in the hyperbolic dispersion regime appear to respond somewhat similarly to plasmonic dimers [42] in the sense of confining and yielding large enhanced fields in the interstitial region between the disks.

On the other hand, particle PhPs observed in hBN nanocones [113, 118] exhibit an extraordinary electric-field landscape with "hot-rings" at deep-subwavelength distances on the nanocone surface (see Figure 21B). These modes are atypical for microparticle resonators comprising isotropic material and originate from the hBN hyperbolic photonic responses that cause unconventional, highly directional, reflections inside the cone structure at its boundary. These peculiar EO-PhPs are promising for shaping resonances with high-quality factors and strong field confinement. Furthermore, very recently, particle PhPs have been also imaged on an α-MoO_3 disk exhibiting also a strong deep-subwalength fringe pattern on the disk surface [132] (see Figure 21C). It can also be seen in Figure 21C that a Fourier-transform of the PhPs curious electric field landscape reveals the underpinning photonic dispersion which emanates from α-MoO_3's indefinite biaxial properties and is similar to the one depicted in Figure 16. Note that, the Cartesian axis system of Figure 21C has the y and z axis interchanged in comparison with the one of Figure 16.

6.3 New physics with particle PhPs: LO-TO phonon mixing and atomic-scale thermal emitters

Both O-PhPs and EO-PhPs are expected to be major protagonists in conceiving new platforms to shape, divert, absorb or emit IR-light as mandated by specific applications. Very importantly, these systems may also unveil new PhP physics. For example, although LO phonon oscillations are known to be inaccessible by IR light in planar geometries [19] it has been very recently reported [236] that microparticle resonators comprising certain anisotropic long-cell polytypes of a PhP material, like 4H-SiC, may enable making zone-folded LO phonons accessible with IR light excitations. In turn, this enables new hybridized longitudinal-transverse PhP excitations. This recent study will inspire new investigations for the understanding, control and realization of these hybrid excitations in other PhP material systems. As Gubbin et al. report [236], these mixed excitations pave the way for the realization of electrically pumped mid-IR emitters. Furthermore, particle PhPs can be brought down to the atomic-scale in low-dimensional particles in which cases atomistic models would be required to capture their PhP responses. Recently, Venkataram et al. [237] developed an atomistic theory to capture PhP-mediated emission and heat-transfer effects between elongated low-dimensional molecules and macroscopic objects that cannot be interpreted with classical models.

7 Patterned PhP materials: metamaterials and mesophotonic platforms

As we discussed in Section 6, localized PhP modes at planar interfaces or particles can offer a plethora of possibilities in IR light control. There are however certain patterning routes of PhP material that build further from these localized modes by harnessing judiciously their interaction. Moreover, non-resonant PhP responses can be also brought together into platforms with new capabilities. We briefly review below quintessential examples of such patterning routes along with the corresponding characteristic length scales of their feature sizes and discuss how they move forward the already vast potential of the systems of Section 6.

7.1 PhP-based metamaterials

7.1.1 Hyperbolic PhP metamaterials

While PhP media can be "natural metamaterials" with hyperbolic photonic responses of type I or type II, as we discussed in Section 6.2, it is certainly worthwhile to look at the metamaterial patterning route to a hyperbolic response with PhP material. This way a broader parameter space and spectral availability of the hyperbolic photonic dispersion can be accessed and tailored by design at will. The associated building-block units should comprise a PhP material in its reststrahlen band and should be deeply sub-wavelength, with a size of the order of $\lambda_0/100$, with λ_0 being the free-space wavelength [80, 238, 239]. When these elemental units are put in periodic arrangements they respond as "meta-atoms" to incoming IR light making a new material with effective photonic properties. The extremely, deep-subwavelength size for the meta-atom is a requirement for a high quality effective hyperbolic response [80] that sustains up to large lateral wave vectors [238].

Typical arrangements reported with PhP material involve either periodic-rod [80, 240, 241] or lamellar structures [238, 239, 242] (Figure 22A). At such deep-subwavelength dimensions it can be assumed the electric-field is quasi-static within each constituent. Then the respective effective permittivity responses parallel and perpendicular to the optical axis, $\varepsilon_{\parallel}$ and $\varepsilon_{\perp}$, can be obtained by established mixing formulae [48, 80, 238, 240] that take into account the EM boundary conditions that apply at the two different electric field orientations. In particular, for the case of periodic rods [80, 240]:

$$\varepsilon_{\parallel} = f\varepsilon_1 + (1-f)\varepsilon_2 \tag{46a}$$

$$\varepsilon_{\perp} = \varepsilon_2 \frac{(1+f)\varepsilon_1 + (1-f)\varepsilon_2}{(1-f)\varepsilon_1 + (1+f)\varepsilon_2}, \tag{46b}$$

and for the case of periodic lamellae [48, 182, 238]:

$$\varepsilon_{\parallel} = \frac{\varepsilon_1\varepsilon_2}{f\varepsilon_2 + (1-f)\varepsilon_1} \tag{47a}$$

$$\varepsilon_{\perp} = f\varepsilon_1 + (1-f)\varepsilon_2, \tag{47b}$$

where ε_1, ε_2 are the isotropic permittivities of the two material constituents and f is the volumetric ratio of constituent '1' with respect to the volume of the unit meta-atom. The optical-axis direction of the effective metamaterial for both systems has been designated in Figure 22A.

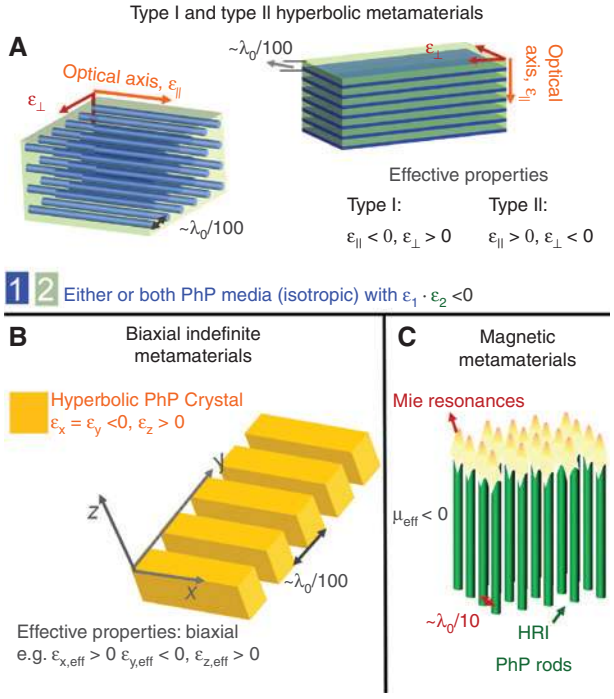

Figure 22: PhP metamaterials: Representative characteristic structures with indicative building-block sizes with respect to the free-space wavelength, λ_0.
(A) Type I and Type II PhP hyperbolic metamaterials (see [80, 240–242]). (B) Biaxial indefinite PhP metamaterial from natural PhP hyperbolic crystals, e.g. hBN (see [243]). (C) Magnetic PhP metamaterial (see [181, 244, 245]).

An indefinite response of $\mathrm{Re}(\varepsilon_{\parallel}) \cdot \mathrm{Re}(\varepsilon_{\perp}) < 0$ is needed to obtain hyperbolic photonic responses of either type. For this to be possible the constituents should have an opposite permittivity, i.e. $\mathrm{Re}(\varepsilon_1) \cdot \mathrm{Re}(\varepsilon_2) < 0$. One possibility is for one constituent to be a PhP material operating within its reststrahlen band with the other constituent being a dielectric. Alternatively, both constituents can be a PhP material with one operating within and the other outside their respective reststrahlen bands. In principle, in a dielectric-PhP material composite both type I and type II hyperbolic responses are accessible at different spectral bands [80, 240]. When both constituents are PhP materials, several spectral bands of type I and type II hyperbolic behavior may emerge; this behavior has been reported for self-organized eutectic ionic crystal mixtures such as NaCl-LiF and NaCl-KCl [80, 241].

PhP-based hyperbolic metamaterials can be instrumental in enabling new components for table-top IR optics. For example, [80] reports that PhP-based hyperbolic metamaterials can function as both polarization filters and converters. Furthermore, the IR lensing and beam-steering capabilities reported for natural PhP

hyperbolic crystals [175–177, 179] can be extended to PhP hyperbolic metamaterials while adding at-will design flexibility over the operational bandwidth and steering angles. Recently, dark-field imaging in the optical spectrum was shown to be possible with a type-I/typeII hyperbolic metamaterial heterostructure [246]. This capability can be extended to the IR with corresponding judiciously designed heterostructures of either two PhP hyperbolic metamaterials or a PhP hyperbolic metamaterial and a natural PhP hyberbolic crystal and can benefit IR imaging systems [37, 203]. Finally, [242] reports that PhP hyperbolic metamaterial may exhibit enhanced superplanckian thermal emission.

7.1.2 Highly tailorable anisotropic PhP metamaterials

The naturally available indefinite responses in PhP materials open-up the possibility of easily implementable and highly tailorable anisotropic photonic metamaterials. Li et al. [243] very recently reported, with a spectroscopic-based analysis, that patterning hBN as a grating with a deeply sub-wavelength pitch of 100 nm can yield effective indefinite biaxial responses (see Figure 22B) of the kind observed in α-MoO_3 (see also Figure 16) but highly tailorable with patterning. Note, that this type of metamaterial is unique to PhP-based systems. It would not be possible to obtain an effective indefinite biaxial behavior with a simple grating patterning in a plasmonic material. In fact, for an analogous biaxial metamaterial to be realized with optical plasmonic systems, a substantially more challenging two-step patterning would be required involving a grating structuring on an already patterned metallodielectric lamellar structure (e.g. see [46, 247]).

7.1.3 Magnetic PhP metamaterials

As the meta-atom sizes of periodic-rod structures increases the quasi-static response picture ceases to be valid and along with it the effective permittivity response models of Eqs. (46) and (47). That does not necessarily mean however, that such systems cease to behave as a metamaterial. In fact, for HRI rods the Mie resonances occur at lower frequencies [248]. Effectively this means that HRI-rod periodic structures may support Mie excitations even when building-block units are significantly smaller than the free-space wavelength [248, 249]. On the other hand, rigorous effective medium tests have shown [80, 181] that periodic dielectric systems with building-block units of the order of ~$\lambda_0/10$, with λ_0 being the free-space wavelength, generally behave as metamaterials. However, their effective photonic responses are generally not captured by the simple standard effective medium theories of Eqs. (46) and (47) [250]. The most general approach to determine the effective EM constitutive properties of periodic PhP-material systems are suitable EM retrieval processes based on their transmission/reflection spectra (see Appendix D of [80] or [181] for a retrieval method established especially for these type of systems). HRI-rod Mie resonances and their interaction with the Bragg resonances in a periodic lattice can be tailored to yield an effective magnetic behavior for the periodic-rod system (see [249]).

PhP media possess a HRI in the vicinity of the TO phonon frequency (see Figure 13). Accordingly, periodic structures with PhP rods, depicted in Figure 22C, are ideal systems to realize the aforementioned magnetic metamaterial for IR frequencies. The first theoretical report of artificial magnetism in PhP-media periodic composites, with an effective negative permeability, μ, came from Huang et al. [244] in a system utilizing $LiTaO_3$ rods. Following this work, a negative effective μ has been reported in an fcc lattice of $LiTaO_3$ [250] as well as in a periodic SiC-rod system [245]. Furthermore, an effective magnetic response, albeit weaker, was reported in [181] in a LiF/NaCl composite, a system that is easily realizable with self-assembled eutectic mixtures [241]. Permeability μ negative media (MNG) in heterostructures with permittivity ε negative media (ENG) may act as a photonic analogue of an LC circuit [251]. Accordingly PhP-based magnetic metamaterials can be useful for the construction of resonator elements in integrated IR photonic systems serving as bandpass filters or modulators.

7.2 PhP-based mesophotonic systems

We use the term "mesophotonic systems" here to describe systems in the sub-wavelength regime where geometric optics fails but that may not respond with effective photonic responses as metamaterials. Typical feature/building-block sizes in this class of system are ~$\lambda_0/2$, with λ_0 being the free-space wavelength. We outline below couple of characteristic platforms in this class that have utilized PhP material.

7.2.1 Particle-PhP arrays: metasurfaces

One-dimensional (1D) or 2D arrays of periodic or more general arrangements of particle PhP resonators can be

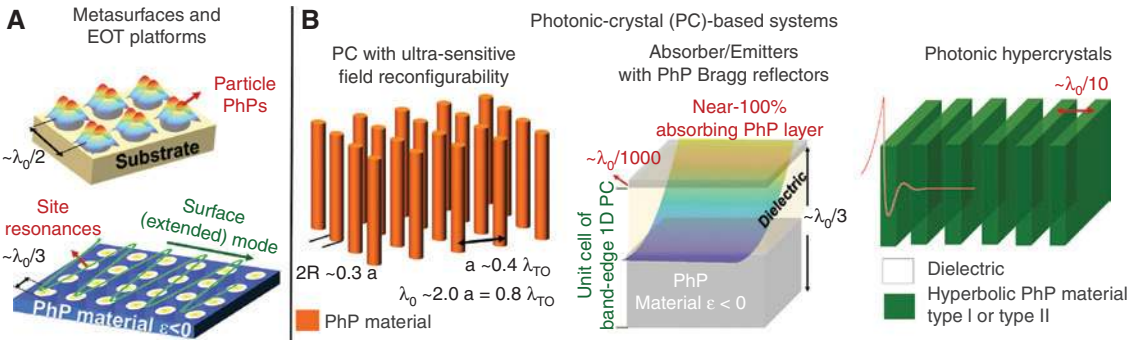

Figure 23: Examples of PhP-based mesophotonic platforms.
(A) PhP analogues of metasurfaces and EOT platforms (e.g. see [87, 100]). (B) PC systems: (left panel) A PC made of PhP-material rods with overlapping photonic and PhP band gaps that exhibits extreme field re-configurability within an ultra-narrow spectral window around the TO phonon frequency (see [252]). (Middle panel) An ultra-thin PhP-material layer atop a PhP-material-dielectric Bragg reflector comprising only one unit cell acts like a frequency-selective near-perfect absorber (see [101]). (Right panel) A photonic hypercrystal: A 1D periodic system comprising alternating layers of a PhP natural hyperbolic crystal (e.g. sapphire) and a dielectric yields new types of low-loss ultra-confined interface states (see [238, 239]). Note that indicative feature/unit-cell size-ranges with respect to the free-space wavelength, λ_0, for the stated targeted operation are given in all examples.

envisioned constituting essentially PhP-based metasurfaces [see, e.g. depiction in Figure 23A]. This line of research has not been widely pursued to the best of our knowledge but is very promising for sculpting, diverting, absorbing/emitting IR light and biosensing methods like SEIRA [197]. For example, one could envision an LSPhP-based platforms for IR beam steering operating analogously to LSP-based ultra-refractive metasurfaces [253]. Then, established design routes of all-dielectric Mie-based metasurfaces [228, 254], such as reflection suppression relying on the lattice Kerker effect [255], can inspire new Mie-PhP-based platforms for near-perfect absorption/emission [256]. Furthermore, new extraordinary particle PhPs set a pathway for unexplored metasurface platforms that have no analogue in IR metallic [26], plasmonic [253] or all-dielectric [228, 255] metasurfaces. Collective phenomena analogous to lattice LSPs [218] will be important to all particle PhP-based metasurfaces.

Currently, specific 1D [86, 98, 100] and 2D [232] arrangements of unit or composite particle-PhP resonators have primarily been researched for harnessing enhanced and/or highly-directional thermal emission. As an example we discuss the platform of [100] seen in Figure 24. LSPhPs in rectangular cross-section rods arranged in a 1D array of micropyramids have been utilized to achieve polarization selective near-perfect absorption that covers about half the SiC reststrahlen band. The micropyramid array responds like moth eyes with a near-zero albedo [257] and thus near-perfect absorption when light impinges from the tip side of the pyramid, sequentially coupling from the smaller cross-section to the larger cross-section rods. By virtue of the directional Kirchoff's law [100] this structure then behaves as a near-unidirectional emitter. The phenomenon can be relevant for highly efficient polarized spectrally selective globar thermal sources which can benefit MIR biomedical imaging [258]. LSPhP-based absorption/

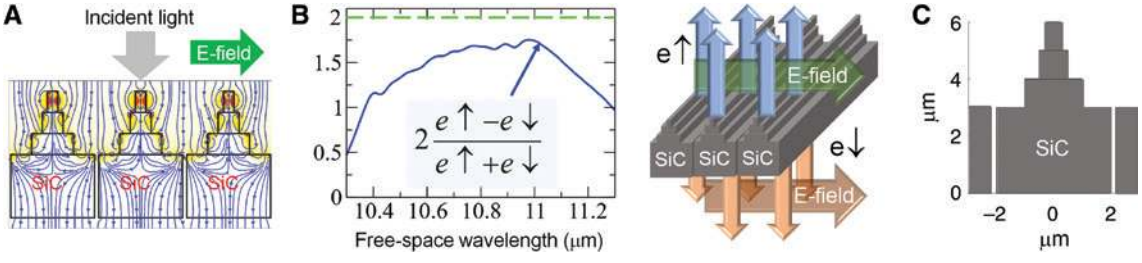

Figure 24: Extreme absorption/emission control with LSPhPs.
(A) TM-polarized light gets near-perfectly absorbed with a SiC micropyramid array in the reststrahlen band of SiC by virtue of a cascaded coupling effect of the LSPhPs from the tip-to-the base SiC blocks. (B) Corresponding highly-asymmetric emissivity, e, of the micropyramid array. A value of 2.0 for the asymmetry factor defined in the inset implies a perfect uni-directional emission (C) Structural size details for the micropyramid array design (zoomed around the middle micropyramid). (After [100]).

emission engineering [86, 98, 100] is promising for many applications including IR-imaging bolometers [259], radiative cooling [10, 11] and optothermal devices [260].

7.2.2 Perforated PhP-material arrays

Holes in a PhP material matrix in the metallic regime, i.e. when $\mathrm{Re}(\varepsilon) < 0$, would also support site-resonances analogous to holes in metals. Accordingly, the long-range interaction between such site resonances in perforated PhP-material arrays (see depiction in Figure 23A) can yield enhanced optical transmission (EOT) phenomena similar to metal perforated arrays [261, 262]. EOT in a perforated SiC array has been reported in Refs. [87, 263]. The interaction between the site resonances at the holes and extended surface-Bloch modes [264] also enables Fano interference [156] in these platforms [87]. This class of systems can be useful to modulate/spectrally select emission spectra pertinent to imaging [37, 203] or thermophotovoltaic applications [265]. Also, the stronger electric fields associated with the site resonances may be suitable to enhance molecular absorption fingerprints for SEIRA methods [197].

7.2.3 Photonic-crystal-based PhP systems

In the photonic crystal (PC) regime, structures do not respond with effective constitutive properties. The behavior of the system is a result of a combination of any localized resonances (e.g. Mie resonances) within the building-block unit and Bragg scattering between the building-block units [248]. PCs with PhP constituents can show extreme field re-configurability within an ultra-narrow spectral window [252]. Specifically, if the photonic band-gap of a periodic-rod PC is aligned with the PhP gap of the PhP-rod constituent material extreme field reconfiguration occurs when crossing the TO phonon frequency: the electric-field is confined within the rods just below the TO phonon frequency and it becomes completely expelled from the rods just above the TO phonon frequency (see indicative structural parameter range for this phenomenon in the left panel of Figure 23B after [252]). The effect may inspire new switchable/reconfigurable PhP-based IR devices.

Furthermore, PhP-based multilayer media are suitable to harness absorption/emission [101, 102, 266] relevant to bolometers [259] and thermo-photovoltaic applications [265]. While PhP media in the reststrahlen band are completely reflective, slicing them up into ultra-thin slices separated by much thicker dielectric spacers can achieve near-100% absorption (see [102] for the case of SiC). In aperiodic arrangements this effect can become highly broadband, covering the entire reststrahlen band [266]. If the multilayer operates near-the-band edge, it provides near-unity reflectivity, i.e. it becomes a Bragg reflector. However, [101] reports that an extremely sub-wavelength PhP material layer of judiciously chosen thickness, placed on top of one unit-cell of such a PhP medium-dielectric Bragg reflector, can suppress reflection while concentrating the electric field on the ultrathin PhP layer. In particular, a spectrally-selective absorption as high as 92% occurring in the ultrathin PhP layer, SiC in this case, was theoretically demonstrated (see schematic in the middle panel of Figure 23B).

We note in passing that, [267] also reports near-perfect absorption on a thin layer of PhP material by utilizing destructive reflection interference in a three-layer system comprising the top PhP material layer, a dielectric spacer and a frequency-selective backreflector. The PhP material layer of [267] has still a sub-wavelength thickness of $\sim\lambda_0/140$, albeit quite larger in comparison to the PhP material top layer of [101] which is about $\sim\lambda_0/1000$, with λ_0 being the free-space wavelength. Additionally, EM wave-interference phenomena for absorption management in PhP material have also been realized in geometries interfacing a PhP material layer and an all-dielectric 1D photonic crystal (multilayer). In particular, [268] reports on one-way near-perfect absorption in a $\lambda_0/25$ thick GaAs layer operating in its reststrahlen band that rests on an all-dielectric Si/SiO2 stack.

Sapphire is also gaining attention as an IR material, given that it also possesses a spectral regime where it behaves as a natural hyperbolic material due to anisotropic PhPs (see also Sections 4.3 and 5.2.1). Narimanov [238] reports periodic multilayers, i.e. 1D PCs, comprising sapphire in the hyperbolic dispersion regime. These type of PCs with hyperbolic material constituents, termed as photonic hypercrystals [see schematic in Figure 23B (right panel)], may give rise to new types of low-loss ultra-confined surface modes [238, 239]. These low-loss surface modes can be utilized for new capabilities in longer-wavelength infrared (LWIR) spectroscopic sensing relevant to part of the IR fingerprint spectrum and smaller molecules [269, 270].

8 Dynamic PhP material for tunable, switchable and reconfigurable IR platforms

In this section we discuss avenues to tune the natural PhP material responses to enable tuning or extension of the

operational bandwidth of pertinent modes and platforms that we discussed in the previous sections. The tunability would permit filling spectral gaps of available PhP material relevant to targeted applications. Furthermore, we discuss possibilities to tune and switch the PhP material responses with external stimuli that would enable new IR tunable, switchable or reconfigurable platforms.

8.1 Doping-tunable PhP permittivity in semiconductors: the LOPC effect

The carriers in semiconductors provide a tuning "knob" for the ionic permittivity response seen in Figure 6 via their Drude contribution to the full permittivity [see Eqs. (30) and (31)]. For a significant carrier concentration, $\omega_p/\sqrt{\varepsilon_\infty}$ can approach or become larger than the TO phonon frequency, ω_{TO} [271]. While the TO phonon frequency, ω_{TO} remains unaffected by the presence of free carriers, as these do not influence the physical properties of the IR activated lattice vibrations, this is not true for the LO phonon frequency, ω_{LO}. With carriers present, there are two possible frequencies, where the permittivity can become zero thus implying that the original LO optical phonon frequency ω_{LO} splits into two branches: ω_{LO+} (blue shifted) and ω_{LO-} (red shifted). This splitting of the LO phonon frequency into two branches [271] has been termed as the longitudinal optical phonon-plasmon coupling (LOPC) effect.

The LOPC effect arises from the ionic and carrier motion being coupled together via the macroscopic electric field. Although known since the 1960s [82], the significance of the LOPC effect for IR light-matter interactions was realized only recently when utilized in planar [272] or microstructured platforms [83, 84] for tunable IR light confinement, enhancement and absorption. To get a feeling for the impact of the LOPC effect on the photonic responses of semiconductors around their reststrahlen band we showcase a demonstrating example in Figure 25 depicting the full permittivity, ε_{sem}, of InP for different carrier concentrations (assuming room temperature).

Doping may be enabled via photoinjection, i.e carrier generation with optical pulsed or continuous wave fields with frequencies above the semiconductor band gap [273]. This has been utilized by [84] to dynamically tune particle PhPs in arrays of InP and 4H-SiC sub-micron pillars. In the semimetals and semiconductors of the 2D/quasi-2D PhP material of Section 4.4, tunability via the LOPC can be achieved by applying a gate voltage. Note that some materials demonstrate a stronger phonon-plasmon coupling leading to cross-coupled damping coefficients; the permittivity response of these materials is different from the independent plasmon and phonon responses of Eqs. (30) and (31) (see [274]).

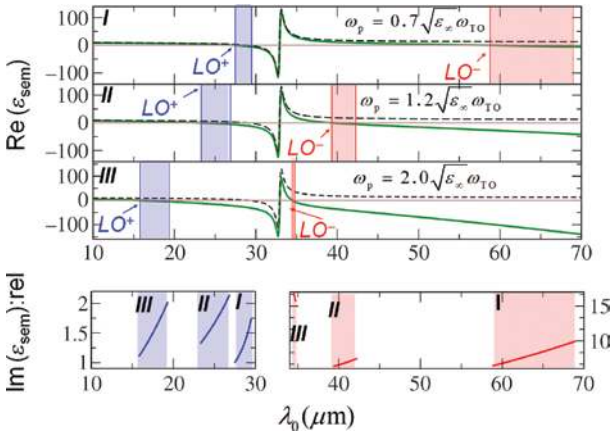

Figure 25: The LOPC effect in InP and its cost in optical loss. (Top panels) The full permittivity, ε_{sem} (real part), versus the free-space wavelength λ_0, for three different plasma frequencies, ω_p of the free carriers is shown. The vertical blue (red) lines annotated with LO^+ (LO^-), depict the blue (red)-shifted LO phonon frequencies. The shaded regions highlight spectral ranges with Re(ε_{sem}) between −5 and 0 which is of interest for plasmonic-type effects and certain metamaterials. (Bottom panels) The imaginary part of ε_{sem} is plotted within the shaded regions in the top panels, scaled with a reference value, Im(ε_{ref}) equal to the imaginary part of the ionic-only permittivity, ε_{ion} at the frequency where the respective real part is equal to −2.5.

8.2 Tunable PhPs with strong optical fields: unlocking non-linear phonon-polaritonics

Another interesting optical-fields-based mechanism has been very recently discovered, unlocking new avenues for tunable phenomena in PhP materials with optical pulses [275]. Specifically, Cartella et al. [275] point out that the linear ionic oscillator model (see Section 3) would be valid only for small-to-moderate displacements. A theoretical model developed by the authors of [275] indicates that the high-frequency permittivity and the ionic effective charge Q (Born-effective charge) may acquire a term that is quadratic on the displacement, u [275] under the influence of strong optical fields. Their hypothesis is supported by experimental evidence showing that the PhPs in SiC can act as a type of a parametric oscillator yielding gain in SiC's reflectance spectrum when excited by a strong pump beam. This very recent study sets the foundations for phonon-enabled IR non-linear photonics opening a whole new range of phenomena and capabilities in IR photonics.

8.3 Electric-field tunable PhP responses: the case of ferroelectrics

Discovered in 1921 [276], ferroelectrics represent a special class of dielectrics with intricate photonic responses stemming from a special acentric crystal structure that however possesses an axis of symmetry [277]. Ferroelectric materials exhibit a residual polarization even in the absence of an applied electric field; with application of an electric field the electric polarization follows a hysteresis similar to the magnetic polarization hysteresis of ferromagnetic materials [19]. Ferroelectric materials lose their curious responses for temperatures above a critical temperature, T_C, known as the Curie temperature [19, 23, 277–279]. The Curie point, T_C, of transition to the ferroelectric phase, can be tuned with the application of stress [280] or even material thickness [281], and can be very high, approaching the melting point for many ferroelectric materials [277].

The explosion and progress in the field of 2D and quasi-2D materials helped also bring ferroelectrics down to the scale of a few nanometers, despite that being initially thought of as impossible [282]. Examples of 2D/quasi-2D ferroelectrics that have been experimentally realized are SnTe, $CuInP_2S_6$ (CIPS) as well as α-In_2Se_3 [282]. Moreover, first principle atomistic calculations revealed additional ferroelectric material that can be stable in 2D form such as SbN [283], BiP [283] and β-GeSe [284]. β-GeSe can be versatile for a range of applications, as it also exhibits strong tunability under strain, which can bring its Curie temperature down to the room temperature range.

Ferroelectrics are very interesting from the point of view of PhPs. Going back to the microscopic model of Section 3.2, we see from Eq. (19) that when:

$$2k = \frac{NQ^2(\varepsilon_\infty + 2)}{9\varepsilon_0} \tag{48}$$

the PhP frequency $\omega_R = \omega_{TO}$ becomes zero while simultaneously the static dielectric constant, ε_s, becomes infinite thus still obeying the LST relation [Eq. (24)] [278, 279]. This unstable PhP behavior is known as polarization catastrophe and signifies the transition to the ferroelectric state [19, 278, 285]. Accordingly, at the transition point a small change in the electric field yields a giant change in the polarization [23]. Following thermodynamic arguments (Devonshire model) it can be shown that in the ferroelectric state, i.e. for temperatures below the Curie temperature T_C, the low-frequency PhP mode (also known as soft-mode) increases in frequency, i.e. "hardens" with the application of a static electric field. Note, however, that the Curie transition temperature itself may increase with the application of a static electric field [286].

Clearly, the PhP (ionic) photonic responses of ferroelectric material are strongly tunable with a static external electric field. Thus ferroelectrics are desirable components for IR tunable devices; especially those with a Curie point at or above room temperature. Ferro-electric material with DC controlled ionic permittivity responses have been recently utilized for tuning the defect mode of a 1D photonic crystal cavity [287]. Moreover, tunable near-field radiative heat transfer has been demonstrated [191] that relies on the electric-field tunability of the associated surface PhP modes (see Section 6.1.1) of the ferroelectric material.

8.4 Magnetic-field tunable photonic responses in the PhP regime: the case of n-InSb

The cyclotron motion of the carrier electrons [23] under a static magnetic field causes a directional change in the full permittivity response of n-doped semiconductors (see [288, 289]). The phenomenon becomes relevant to tuning photonic responses in the PhP regime only when the cyclotron frequency, $\omega_c = eB/m_e^*$, with $B = |\mathbf{B}|$ being the magnetic field strength, is in the range of the TO phonon frequency, ω_{TO} for relatively low magnetic fields. Not many semiconductors would meet that requirement. Given its low electron effective mass, n-doped InSb has been predominantly studied for its magnetic-field tunable photonic responses in its PhP regime from the 1970s [85] until today (see indicative example in Figure 26A).[22] Recent related research includes tunable non-reciprocal plasmonic-type devices functional at THz frequencies for photonic isolators [289, 291], THz sensors [292], THz tunable polarization conversion [289] as well as magnetic-field tunable near-field radiative heat transfer pertinent to ultrafast control of thermal management [293, 294].

8.5 Turning PhP photonic responses on and off by phase transitions

VO_2 has been attracting increasing attention as a tunable photonic material owing to its transition from an insulating monoclinic to a metallic rutile phase at the temperature of 68°C [106, 107]. VO_2 exhibits multiple PhP oscillations in its insulating phase (see Table 4). When heated beyond the transition temperature, these PhP

22 Representative values for the carrier concentration and electron effective mass as well as the PhP model parameters have been taken from [85] (see also Table 2 for the latter).

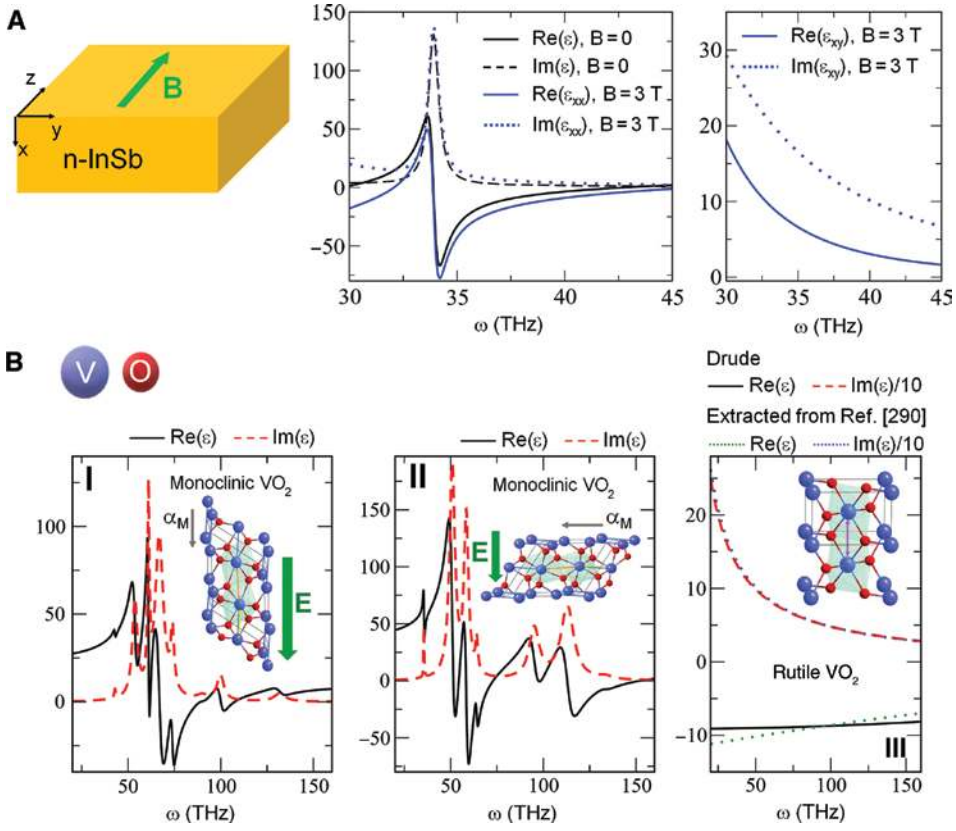

Figure 26: Tunable photonic responses in the PhP regime.
(A) A static magnetic field induces anisotropy with large off-diagonal terms in the permittivity of n-doped InSb [85]. (B) Phase-change enabled temperature tunability in VO_2: I and II depict the anisotropic room-temperature permittivity in monoclinic VO_2 showing multiple PhP resonances (see Table 4 and [105]). Panel III shows the real and imaginary parts of the VO_2 permittivity (dotted-green and dotted-blue lines) in the rutile metallic phase at 360 °K calculated here based on the experimental data and analysis of [290] [see note 24]. The black-solid and red-dashed lines depict the respective values from a matching simple Drude model considered here. [The VO_2-crystal-structure insets are reproduced (adapted) from [106] through Creative Commons Attribution License, see link at https://creativecommons.org/licenses/by/3.0/].

responses completely disappear and VO_2 responds with a metallic Drude-like permittivity.[23]

In Figure 26B-I and 26B-II we plot the room-temperature permittivity of VO_2 in the PhP regime for electric fields parallel and perpendicular, respectively, to its crystallographic direction, α_M (ionic permittivity model parameters are from [105] shown in Table 4). Indeed, we observe from Figure 26B-III that the permittivity changes dramatically past the phase-transition point at a temperature of 87°C where VO_2 is in the rutile metallic phase.[24]

Based on permittivity values extracted from the Basov-group experimental data [290], we also considered here a standard fitting Drude model that captures well the permittivity in the metallic rutile phase for the frequency range relevant to the PhP regime of the insulating phase. This Drude model's parameters are $\omega_p = 15.67 \times 10^{14}$ rad/s and $\gamma_p = 4.92 \times 10^{14}$ rad/s; the associated real (imaginary) part of the permittivity is represented with the black-solid (red-dashed) lines in Figure 26B-III.

The ionic-to-Drude permittivity transition in VO_2 has been utilized to tune the near-field radiative heat transfer with temperature [192] as well as to device a microsecond switchable thermal antenna [295]. Both effects rely on switching on/off surface or particle PhPs in VO_2. As other phase-change material, like GST [200, 201], are gaining interest for photonics in the last years, new PhP switching capabilities beyond VO_2 may come to light. In fact, there is recent on-going research on characterizing IR active phonons in GST and other phase-transitioning alloys [296,

23 VO_2 undergoes a Mott-type insulator-to-metal transition [290]; around the transitional temperatures there is coexistence of an insulating phase and a strongly-correlated electron metallic phase that is different from the rutile metallic phase at higher temperatures.

24 The real (imaginary) parts of the permittivity [green-dotted (blue-dotted) lines of Figure 26B-III] has been calculated from [290] by taking the experimental properties as depicted in Figure 4 and using relations (1), (C1), and (C2) of this reference.

297]. Temperature enabled volatile PhP control in phase-change material would be highly attractive for applications pertinent to thermal homeostasis capability [298] or for thermal camouflage [299]. Non-volatile PhP switching is pertinent to reconfigurable elements for integrated IR photonics. Furthermore, recent research that enabled gate-controlled non-volatile phase-transition in VO_2 [300] via hydrogen ion infiltration offers potentially exciting pathways towards gate-tunable PhP-based IR photonics with VO_2.

Of course phase-transition enabled tunable devices can also be envisioned by interfacing PhP material not undergoing a phase transition with other phase-change material not possessing PhPs in the spectrum of interest. We will review the latter type of systems when we discuss hybrid platforms in the following section.

9 Hybrid platforms with PhPs

Hybrid platforms are systems that bring together, in a synergistic manner, capabilities stemming from distinct physical mechanisms. In this manner, "the best of two worlds" is combined towards breaking performance bottlenecks or enabling new functionalities and thus broadening the applications horizon. Hybrid approaches to designing photonic devices are gaining increased popularity across the EM spectrum. For example, 2D semiconductors can be combined with disk resonators or photonic crystals to enhance their photoluminescence spectrum [301, 302]; plasmonic nanoantennae can be combined with dielectric microcavities achieving both high confinement and high quality factor, Q [303]. In this section, we discuss how certain PhP modes reviewed in previous sections can be combined with other types of photonic modes and/or materials to form hybrid systems that advance further extreme IR light control.

In Section 3 we discussed that PhPs are hybridized modes coming from strong coupling of IR light and lattice vibrations. PhP-enabled modes, such as SPhPs or GPhPs, may also themselves hybridize with other types of modes, such as SPPs. Such hybridization manifests itself as a strong modification of their mixed dispersion, $\omega(k)$. In fact, the original independent modes have dispersions that cross in the (ω, k) space. As a result of the their strong interaction they may convert into two anti-crossed branches both having a mixed character from the two original independent modes. Such anti-crossing is really the quintessential signature of the strong-coupling effect between two different types of modes [304]. One possibility is SPhPs strongly-coupling with SPPs. For example, [305] reports on the strong coupling between SPhPs, native of an SiC or oxide layer, with SPPs, native of a plasmonic metallic layer. Such strong coupling is exploited to devise an architecture that provides enhancement of near-field radiative heat transfer while at the same time being tunable by application of a gate voltage. The gate voltage tunability is facilitated by the PhP material layer which in fact serves in a dual role: enhancing the near-field heat transfer and providing an insulating spacer between the plasmonic layer and the metallic contact, needed for tuning the properties of the the plasmonic layer with voltage. Furthermore, strong coupling between SPhPs of a SiO_2 layer and Mie plasmons of a gold nanoantenna [306] as well as SPhPs on a PMMA film and designer SPPs of a plasmonic metamaterial [307] have also been reported. Such effects can find applications in modulators and filters for IR sources.

Naturally, the current interest in 2D and quasi-2D photonic material [135, 136], has also spurred investigations of SPP-SPhP as well as SPP-GPhP strong coupling involving composite systems with either or both constituents being atomically-thin materials. Many related systems have been reported for strong coupling between SPP modes in graphene, and several SPhP modes in SiO_2 [308],[25] SPP modes in graphene and the hyperbolic GPhP in hBN [109, 123, 310, 311] (e.g. see Figure 27A) or SPP modes in doped BP and GPhPs in SiO_2 [314]. This strong-coupling enables modulation of the composite SPP-SPhP or SPP-GPhP photonic dispersion with gate-tunable capability via gating of the graphene layer. Highly-doped bilayer graphene is a uniquely interesting system because it can by itself support SPP-SPhP hybridization. Although monolayer graphene does not support PhPs, bilayer graphene does (see Section 4.4). Then the native longitudinal (transverse) plasmons can couple to the TO (LO) optical phonons [315]. Such hybridization grows stronger with increased doping and shows the signature of strong coupling: anti-crossing of the mixed-mode dispersion bands. The phenomenon has been experimentally verified in ultra-highly doped bilayer graphene via $FeCl_3$ intercalation [316]. These effects open several possibilities for bringing extreme IR light control with 2D tunable devices.

Furthermore, in a graphene-polar semiconductor heterostructure it was reported that GPhPs supported in an ultrathin polar semiconductor layer may fast decay into graphene SPPs thereby getting completely quenched [317]. Also, hot carriers in graphene [318] or in highly-biased

25 SiO_2, like quartz, possesses multiple PhP oscillations; see [309].

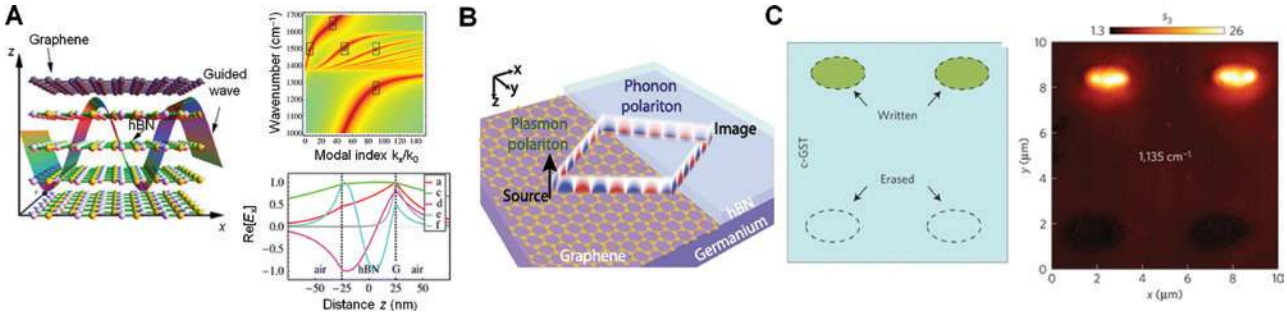

Figure 27: Examples of hybrid platforms with PhPs.
(A) Dispersion of hybrid modes emanating from strong coupling between the type II hyperbolic GPhPs in hBN and the SPPs in graphene (top right panel) in a graphene-hBN heterostructure (left panel). The *x*-component of the electric field, E_x, is also shown (bottom right panel) across the heterostructure for the modes designated in the top panel. [Reprinted (adapted) with permission from [109]. Copyright 2015 American Chemical Society.] (B) Negative refraction at the interface of a graphene-hBN lateral heterostructure: An SPP wave supported on graphene refracts negatively to a GPhPs supported on hBN in the spectral regime where it has a type I hyperbolic dispersion. (Reprinted with permission from [312]). (C) Re-writable patterns on GST by changing its phase. The GST rests on a quartz substrate operating within its reststrahlen band thus supporting SPhPs. The different GST phases provide a different dielectric environments for the SPhPs; this causes SPhP scattering at the boundaries of the elliptical amorphous GST areas thereby giving rise to the localized modes visualized with s-SNOM (right panel). (Reprinted by permission from Springer Nature Customer Service Centre GmbH: Springer Nature-Nature Materials [313]. Copyright 2016.)

graphene bilayers [319] can cool via coupling to the GPhP modes of an adjacent hBN layer. 2D material dielectrics, such as TMDs outside their PhP regime, also can affect the properties of SPhPs in an adjacent polar semiconductor layer; in particular they ultra-squeeze the associated SPhPs into tight confinement [320]. Moreover, gate-tunable hybridized SPP-SPhP modes have been reported in a graphene-LiF heterostructure; these may be tailored to outperform, in terms of combined confinement and propagation length, both the individual SPPs supported by the graphene layer and the SPhPs supported on the LiF surface [321].

Beyond mode interaction, hybridization and strong coupling, atomically-thin PhP material can be interfaced with other atomically-thin material to tailor their photonic responses or achieve new functionalities. For example, a deep-subwavelength graphene/hBN heterostructure can serve as a gate-tunable meta-atom for a metamaterial with adjustable photonic dispersion. The latter metamaterial's photonic response can change from ellipsoidal to hyperbolic (see Figure 15) making it an ideal medium to strongly modulate the emission spectrum of single-photon emitters [322]. A similar graphene/polar-dielectric (SiO_2) lamellar structure acting as a tunable hyperbolic metamaterial [323] has been very recently experimentally realized; the structure incorporates additional Al, and Al_2O_3 layers needed to enable the fabrication of the structure. Furthermore, hBN/BP vertical heterostructures have also been considered operating within the PhP regime of hBN and outside the PhP regime of BP. The strong in-plane anisotropy of the BP dielectric enables GPhPs in hBN that are in-plane anisotropic [324]. In addition, when a lateral heterostructure interface is considered between graphene and hBN, SPPs supported on the graphene side may refract negatively into GPhPs on the hBN side at the graphene-hBN interface [312] (see also Figure 27B). By virtue of such negative refraction a localized emitter source may be focused across the interface similarly to a point source focusing through Pendry's negative refraction index lens [178, 213], making this an attractive platform for imaging applications. Furthermore, very recently tunable IR superlensing has been theoretically reported in a similar system in an hBN-graphene lateral heterojunction resting on a SiC substrate; this tailorable and tunable superlens phenomenon exploits the strong coupling between the SPhP modes supported by SiC and the hyperbolic PhPs supported in hBN [325].

Phase-change material (PCM), such as VO_2 [107, 299] and GST [200, 201], are gaining increased attention as photonic materials. In Section 8.5, we discussed how PhP responses can be turned on and off in VO_2 as well as on-going research in uncovering PhP responses in GST. However, even outside their PhP regime these material can serve as a volatile or non-volatile photonic environment to tune or reconfigure the PhP responses of PhP-based platforms interfaced with them. For example, [326] reports a VO_2-hBN-graphene vertical heterostructure with asymmetric light transmission and resonant near-perfect absorption capability that can be tuned both via the VO_2 insulator-to-metal transition and via gating of the graphene.

Furthermore, judiciously designed patterns on PCMs that comprise the different material phases can be used for reconfigurable beam-shaping and steering of SPhP- or GPhP-waves supported on an adjacent hBN flake [327]. A similar phenomenon has been used in a GST-quartz heterostructure. The reversible switching of GST between amorphous and crystalline phases allows writing and erasing paths for SPhP guided waves as well LSPhP resonator structures [313, 328] (see also Figure 27C). In addition, SPhPs on SiC interacting with deep-subwavelength metal holes form a high-Q cavity with ultra-small modal volume. A thin GST layer sandwiched between the SiC layer and the perforated gold structure can switch the cavity on and off by modifying GST's dielectric constant by switching it between the crystalline and amorphous phases [329].

Finally, there has been recent interest in IR-integrated photonics analogous to integrated optics [15]. Long-range IR waveguides of ultra-confined modes would be key components to advance such area. Natural candidates would be of course SPhP-based or GPhP-based structures. Hybridization of PhP-waveguides with other guiding components enables flexibility and control over their guiding characteristics including propagation range. Different types of such hybrid waveguides have been reported such as 4H-SiC SPhP-ridge Si hybrid waveguide [330] as well as SPhP-insulator-SPhP waveguide with hBN [331]. Moreover, highly tailorable localized IR photonic modes have been reported in [332] by enabling hybridization between the modes supported by a Ge grating structure and the SPhP modes supported on the interface of SiC. The PhP-quantum well system may also enable new integrated IR sources as recent research shows the large lateral momenta of any type of polaritons facilitate indirect transitions in semiconductors [333]. Furthermore, Ohtani et al. [334] very recently have reported an electrically pumped phonon-polariton laser. Specifically, the intersubband gain in a quantum cascade structure leads to emission into PhPs supported by one of the constituents in the superlattice (AlAs). This structure can also be regarded as a type of phonon laser as significant energy is directed into the vibrational motion of the atomic ions.

We have recapped above the most predominant research directions involving hybrid platforms with PhP media. Of course many other hybrid systems of variable degree of complexity bringing together different system types for photonic control may be envisioned. For example, [335] reports on a PhP slab interfaced with a dielectric grating and a graphene metamaterial aiming to achieve tunable THz deflection and asymmetric transmission.

10 Conclusions and outlook

Phonon-polaritonics is a burgeoning field bringing into the IR domain many of the powerful capabilities that until recently had been only available in the optical domain. We reviewed here key widely-used and emergent PhP material including 2D and quasi-2D material that play a central role in the development of this field. We discussed a microscopic picture explaining how these PhP material obtain their extraordinary responses, recapped the vast range of distinct photonic responses they make available as well as presented avenues by which these can be tuned/reconfigured. We reviewed the different types of modes that can be supported with PhP material and discussed the capabilities they bring out and associated application areas they advance. Finally, we presented many examples that move forward the already versatile potential of PhP material by considering metamaterial and mesophotonic structuring routes as well as interfacing them with other photonic modes or systems, such as SPPs, antenna resonators, ridge waveguides or phase-change material.

Phonon-polaritonics has grown immensely in the last years impacting the advancement of a broad range of high-interest application areas in IR photonics, such as thermal imaging [37, 203], thermal photovoltaics [265], SEIRA [197], sensors and detectors [198], heat management and radiation cooling [10, 11, 194, 305], THz imaging for medical diagnostics [12] as well as components for integrated IR photonics [15]. The parallel rapid development of the fields of atomically-thin material photonics [135, 136], PCM photonics [107, 200, 201] and thermal management [10, 11, 100, 194, 298, 299, 305] serves as a catalyst for the continued progress of the phonon-polaritonics field; PhP photonics is expected to continue to flourish in the years to come bringing out many more exciting new phenomena and applications for IR light.

Phonon-polaritonics is a part of the broader field of polaritonics [336, 337] that involves different types of material excitations that strongly couple with light, such as magnon-polaritons (e.g see [338]) or exciton-polaritons (e.g. see [339]). As other polaritons also induce a Lorentzian-resonant response in the material's constitutive properties, for example, in the permittivity for exciton-polaritons [339] or in the permeability for magnon-polaritons [338] the progress in phonon-polaritonics can inspire new photonic platforms with other type of polaritonic materials in the applicable spectal ranges (e.g. see [340] for exciton polaritons).

Acknowledgments: We would like to thank the UNM Center for Advanced Research Computing, supported in

part by the National Science Foundation, for providing the high-performance computing resources used in this work. Sandia National Laboratories is a multimission laboratory managed and operated by National Technology & Engineering Solutions of Sandia, LLC, a wholly owned subsidiary of Honeywell International Inc., for the U.S. Department of Energy's National Nuclear Security Administration under contract DE-NA0003525. This paper describes objective technical results and analysis. Any subjective views or opinions that might be expressed in the paper do not necessarily represent the views of the U.S. Department of Energy or the United States Government. D. W. acknowledges the support from NSF grant ECCS-1609912. S. K. acknowledges support from the George R. K. Smith Chair account.

References

[1] Maier SA. Plasmonics: fundamentals and applications. New York, Springer, 2007.
[2] Stockman MI, Kneipp K, Bozhevolnyi SI, et al. Roadmap on plasmonics. J Opt 2018;20:043001.
[3] Law S, Podolskiy V, Wasserman D. Towards nano-scale photonics with micro-scale photons: the opportunities and challenges of mid-infrared plasmonics. Nanophotonics 2013;2:103–30.
[4] Miller DL. Principles of infrared technology: a practical guide to the state of the art. New York, Springer, 1994.
[5] Ferguson B, Zhang X-C. Materials for terahertz science and technology. Nat Mater 2002;1:26–33.
[6] Baker JM, Aleese LM, Meijer G, Von Helden G. Fingerprint IR spectroscopy to probe amino acid conformations in the gas phase. Phys Rev Lett 2003;91:203003.
[7] Keirssea J, Boussard-Pledela C, Lorealb O, et al. IR optical fiber sensor for biomedical applications. Vib Spectrosc 2003;32: 23–32.
[8] Adato R, Altug H. In situ ultra-sensitive infrared absorption spectroscopy of biomolecule interactions in real time with plasmonic nanoantennas. Nat Commun 2013;4:2154.
[9] Dall'o G, Sarto L, Panza A. Infrared screening of residential buildings for energy audit purposes: results of a field test. Energies 2013;6:3859–78.
[10] Raman AP, Anoma MA, Zhu L, Rephaeli E, Fan S. Passive radiative cooling below ambient air temperature under direct sunlight. Nature (London) 2014;515:540–4.
[11] Raphaelli E, Raman A, Fan SH. Ultrabroadband photonic structures to achieve high-performance daytime radiative cooling. Nano Lett 2013;13:1457–61.
[12] Diakides NA, Bronzino JD. Medical Infrared Imaging. Boca Raton, FL, CRC Press (Taylor & Francis), 2007.
[13] Button KJ. Infrared and millimeter waves Vol. 6: systems and components. New York, Academic Press, 1982.
[14] Wanke MC, Lee M, Nordquist CD, et al. Integrated chip-scale THz technology. Proceedings of the SPIE 8031, Micro- and Nanotechnology Sensors, Systems, and Applications III. 2011:80310E.
[15] Zou Y, Chakravarty S, Chung C-J, Xu X, Chen RT. Mid-infrared silicon photonic waveguides and devices. Photonics Res 2018;6:254.
[16] Feurer T, Stoyanov NS, Ward DW, Vaughan JC, Statz ER, Nelson KA. Terahertz polaritonics. Annu Rev Mater Res 2007;37:317–50.
[17] Joshua Caldwell D. Mid-IR to THz polaritonics: realizing novel materials for nanophotonics (Conference Presentation). Proceedings of the SPIE 9918, Metamaterials, Metadevices, and Metasystems 2016;2016:991828.
[18] Feng K, Streyer W, Zhong Y, Hoffman AJ, Wasserman D. Photonic materials, structures and devices for reststrahlen optics. Opt Express 2015;23:A1418–33.
[19] Kittel C. Introduction to solid state physics. Hoboken, NJ, John Wiley & Sons, 2005.
[20] Adachi S. The reststrahlen region. In: Optical properties of crystalline and amorphous semiconductors. New York, Springer, 1999:33–62.
[21] Economou EN. The physics of solids: essentials and beyond. Berlin, Heidelberg, Springer-Verlag, 2010.
[22] Brown FC. The physics of solids: ionic crystals, lattice vibrations and imperfections. New York, W.A. Benjamin Inc., 1967.
[23] Ashcroft NW, David Mermin N. Solid state physics. New York, Holt, Rinehart and Winston, 1976.
[24] Huang K. On the interaction between the radiation field and ionic crystals. Proc R Soc Lond Ser A 1951;208:352–65.
[25] Smith DR, Schurig D. Electromagnetic wave propagation in media with indefinite permittivity and permeability tensors. Phys Rev Lett 2003;90:077405.
[26] Yu N, Aieta F, Genevet P, Kats MA, Gaburro Z, Capasso F. A broadband, background-free quarter-wave plate based on plasmonic metasurfaces. Nano Lett 2012;12:6328–33.
[27] Aydin K, Ferry VE, Briggs RM, Atwater HA. Broadband, polarization-independent resonant light absorption using ultrathin, plasmonic super absorbers. Nat Commun 2011;2:517.
[28] Mason JA, Smith S, Wasserman D. Strong absorption and selective thermal emission from a midinfrared metamaterial. Appl Phys Lett 2011;98:241105.
[29] Watts CM, Liu X, Padilla WJ. Metamaterial electromagnetic wave absorbers. Adv Mater 2012;24:OP98.
[30] Liu YQ, Kong LB, Liu PK, Long-range spoof surface plasmons on the doubly corrugated metal surfaces. Opt Commun 2016;370:13–7.
[31] Ye Y-H, Zhang J-Y, Middle-infrared transmission enhancement through periodically perforated metal films. Appl Phys Lett 2004;84:2977–9.
[32] Subramania G, Foteinopoulou S, Brener I. Nonresonant broadband funneling of light via ultrasubwavelength channels. Phys Rev Lett 2011;107:163902.
[33] Etchegoin PG, Le Ru EC, Meyer M. An analytic model for the optical properties of gold. J Chem Phys 2006;125:164705; *ibid* J. Chem Phys 2007;127:189901.
[34] Palik ED. Handbook of optical constants of solids, Vols. I and II, III. San Diego, CA, USA; Chestnut Hill, MA, USA; London, UK, Academic Press, 1985, 1991, 1998.
[35] Johnson PB, Christy RW. Optical constants of noble metals. Phys Rev B 1972;6:4370.
[36] Panofsky WKH, Phillips M. Classical electricity and magnetism. Reading, MA, USA; London, UK, Addison-Wesley Publishing Company Inc., 1962.

[37] Montoya JA, Tian ZB, Krishna S, Padilla WJ. Ultra-thin infrared metamaterial detector for multicolor imaging applications. Opt Express 2017;25:23343–55.
[38] Raether H. Surface plasmons on smooth and rough surfaces and on gratings. Berlin, Heidelberg, Springer-Verlag, 1988.
[39] Economou EN. Surface plasmons in thin films. Phys Rev 1969;182, 539.
[40] Pelton M, Aizpurua J, Bryant G. Metal-nanoparticle plasmonics. Laser Photon Rev 2008;2:136–59.
[41] Foerster B, Rutten J, Pham H, Link S, Sonnichsen C. Particle plasmons as dipole antennas: state representation of relative observables. J Phys Chem C 2018;122:19116–23.
[42] Foteinopoulou S, Vigneron JP, Vandenbem C. Optical near-field excitations on plasmonic nanoparticle-based structures. Opt Express 2007;15:4253–67.
[43] Yamamoto N, Ohtani S, Javier Garcia de Abajo F. Gap and Mie plasmons in individual silver nanospheres near a silver surface. Nano Lett 2011;11:91–5.
[44] Stratton JA. Electromagnetic theory. New York, London, McGraw-Hill, 1941.
[45] Engheta N. Pursuing near-zero response. Science 2013;340:286–7.
[46] Subramania G, Fischer AJ, Luk TS. Optical properties of metal-dielectric based epsilon near zero metamaterials. Appl Phys Lett 2012;101:241107.
[47] Liu Y, Bartal G, Zhang X. All-angle negative refraction and imaging in a bulk medium made of metallic nanowires in the visible region. Opt Express 2008;16:15439–48.
[48] Poddubny A, Iorsh I, Belov P, Kivshar Y. Hyperbolic metamaterials. Nat Photon 2013;7:948–67; (and references therein).
[49] Low T, Avouris P. Graphene plasmonics for terahertz to mid-infrared applications. ACS Nano 2014;2:1086–101.
[50] Guo Q, Li C, Deng B, Yuan S, Guinea F, Xia F. Infrared nanophotonics based on graphene plasmonics. ACS Photonics 2017;4:2989–99.
[51] Naik GV, Kim J, Boltasseva A. Oxides and nitrides as alternative plasmonic materials in the optical range. Opt Mater Exp 2011;1:1090–9.
[52] Khamh H, Sachet E, Kelly K, Mariab J-P, Franzen S. As good as gold and better: conducting metal oxide materials for mid-infrared plasmonic applications. J Mater Chem C 2018;6: 8326–42.
[53] Ginn JC, Jarecki RL, Shaner EA, Davids PS. Infrared plasmons on heavily-doped silicon. J Appl Phys 2011;110:043110.
[54] Barho FB, Gonzalez-Posada F, Milla M-J, et al. Highly doped semiconductor plasmonic nanoantenna arrays for polarization selective broadband surface-enhanced infrared absorption spectroscopy of vanillin. Nanophotonics 2018;7:507–16.
[55] Chochol J, Postava K, Cada M, et al. Plasmonic behavior of III-V semiconductors infrared and terahertz range. J Eur Opt Soc: Rapid Pub 2017;13:13.
[56] Zhong Y, Malagari SD, Hamilton T, Wasserman DM. Review of mid-infrared plasmonic materials. J Nanophotonics 2015;9:093971.
[57] Taliercio T, Biagioni P. Semiconductor infrared plasmonics. Nanophotonics 2019;8:949–90.
[58] Poulet H, Mathieu JP. Vibration spectra and symmetry of crystals. New York, Gordon and Breach, 1976.
[59] Yu P, Cardona M. Fundamentals of semiconductors: physics and material properties, Vol. 3, Berlin; London, Springer, 2010.
[60] Jackson JD. Classical electrodynamics. New York, John Wiley and Sons, 1962.
[61] Huang K. Phenomenological equations of motion for simple ionic lattices. Tech Rep 1950;T339:50–9.
[62] Stern F. Elementary theory of the optical properties of solids. Solid State Phys 1963;15:299–408.
[63] Huang K. Lattice vibrations and optical waves in ionic crystals. Nature 1951;167:779.
[64] Rivera N, Coulter J, Christensen T, Narang P. Ab initio calculation of phonon polaritons in silicon carbide and boron nitride. 2018:Arxiv: 189.00058.
[65] Houstoun RA. A treatise on light. London; New York, Longmans Green and Co, 1942.
[66] Pahuja OP. Solid state physics. New Delhi, Laxmi Publications, 2005.
[67] Dragoman D, Dragoman M. Optical characterization of solids. Berlin, Heidelberg, New York, Springer-Verlag, 2002.
[68] Ushioda S, McMullen JD, Delaney MJ. Damping mechanism of polaritons in GaP. Phys Rev B 1973;8:4634–7.
[69] Klemens PG. Anharmonic decay of optical phonons. Phys Rev 1966;148:845.
[70] Schwarz UT, Maier M. Damping mechanisms of phonon-polaritons, exploited by stimulated Raman gain measurements. Phys Rev B 1998;58:766–75.
[71] Srivastava GP. The physics of phonons. New York, Taylor and Francis, 1990.
[72] Bittner B, Scherm M, Schoed T, Tyroller T, Schwarz UT, Maier M. Phonon-polariton damping by low-frequency excitations in lithium tantalate investigated by spontaneous and stimulated Raman scattering. J Phys: Condens Matter 2002;14:9013–28.
[73] Schwarz UT, Maier M. Frequency dependence of phonon-polariton damping in lithium niobate. Phys Rev B 1996;53:5074.
[74] Barker AS. Dielectric dispersion and phonon line shape in gallium phosphide. Phys Rev 1968;165:917–22.
[75] Schoche S, Hofmann T, Korlacki R, Tiwald TE, Schubert M. Infrared dielectric anisotropy and phonon modes of rutile TiO_2. J Appl Phys 2013;113:164102.
[76] Tropf WJ, Thomas ME, Harris TJ. Properties of crystals and glasses. In: Bass M, Van Stryland EW, Williams DR, Wolfe WL, editors. Handbook of optics, vol. 2: devices, measurements and properties. New York, NY, McGraw-Hill, 1995.
[77] Berreman DW, Underwald FC. Adjusting poles and zeros of dielectric dispersion to fit reststrahlen of $PrCl_2$ and $LaCl_2$. Phys Rev 1968;174:791.
[78] Gervais F, Piriou B. Temperature dependence of transverse- and longitudinal-optic modes in TiO_2 (rutile). Phys Rev B 1974;10:1642.
[79] Schubert M, Tiwald TE, Herzinger CM. Infrared dielectric anisotropy and phonon-modes of sapphire. Phys Rev B 2000;61:8187.
[80] Foteinopoulou S, Kafesaki M, Economou EN, Soukoulis CM. Two-dimensional polaritonic photonic crystals as terahertz uniaxial metamaterials. Phys Rev B 2011;84:035128.
[81] Kaiser W, Spitzer WG, Kaiser RH, Howarth LE. Infrared properties of CaF_2, SrF_2, and BaF_2. Phys Rev 1962;127:1950.
[82] Varga BB. Coupling of plasmons to polar phonons in degenerate semiconductors. Phys Rev 1965;137:A1896–902.
[83] Streyer W, Feng K, Zhong Y, Hoffman AJ, Wasserman D. Engineering the reststrahlen band with hybrid plasmon/phonon excitations. MRS Commun 2016;6:1–8.

[84] Dunkelberger AD, Ellis CT, Ratchford DC, et al. Active tuning of surface phonon-polariton resonances via carrier photoinjection. Nat Photonics 2018;12:50–7.
[85] Palik ED, Kaplan R, Gammon RW, Kaplan H, Wallis RF, Quinn JJ. Coupled surface magnetoplasmon-optic-phonon-polariton modes on InSb. Phys Rev B 1976;13:2497–506.
[86] Vassant S,, Marquier F, Greffet JJ, Pardo F, Pelouard JL. Tailoring GaAs terahertz radiative properties with surface phonons polaritons. Appl Phys Lett 2010;97:161101.
[87] Catrysse PB, Fan S. Near-complete transmission through subwavelength hole arrays in phonon-polaritonic thin films. Phys Rev B 2007;75:075422.
[88] Spitzer WG, Kleinman D, Walsh D. Infrared properties of hexagonal silicon carbide. Phys Rev 1959;113:127.
[89] Manabe A, Mitsuishi A, Yoshinaga H. Infrared lattice reflection spectra of II-VI compounds. Japanese J Appl Phys 1967;6:593–600.
[90] Ng SS, Ooi PK, Lee SC, Hassan Z, Abu Hassan H. Surface phonon-polariton of wurtzite AlN thin film grown on sapphire. Mater Chem Phys 2012;134:493–8.
[91] Barker Jr AS, Ilegems M. Infrared lattice vibrations and free-electron dispersion in GaN. Phys Rev B 1973;7:743–50.
[92] Martin BG, Broerman JG. Theory of surface polaritons in a polar zero-gap semiconductor. Phys Rev B 1981;24.
[93] Grynberg M, Le Toullec R, Balkanski M. Dielectric function in HgTe between 8 and 300 K. Phys Rev B 1974;9.
[94] Claus R, Merten L, Brandmuller J. Light scattering by phonon-polaritons. Springer-Verlag Berlin, 1975.
[95] Irmer G, Roder C, Himcinschi C, Kortus J. Phonon-polaritons in uniaxial crystals: a Raman scattering study of polaritons in α-GaN. Phys Rev B 2013;88:104303.
[96] Kong JA. Electromagnetic wave theory. New York, John Wiley & Sons, 1990.
[97] Tiwald TE, Woollam JA, Zollner S, et al. Carrier concentration and lattice absorption in bulk and epitaxial silicon carbide determined using infrared ellipsometry. Phys Rev B 1999;60:11464.
[98] Le Gall J, Olivier M, Greffet J-J. Experimental and theoretical study of reflection and coherent thermal emission by a SiC grating supporting a surface-phonon-polariton. Phys Rev B 1997;55:10105–14.
[99] Narayanaswamy A, Chen G. Surface modes for near field thermophotovoltaics. Appl Phys Lett 2003;82:3544.
[100] Devarapu GCR, Foteinopoulou S. Broadband near-unidirectional absorption enabled by phonon-polariton resonances in SiC micropyramid arrays. Phys Rev Appl 2017;7:034001.
[101] Devarapu GCR, Foteinopoulou S. Compact photonic-crystal superabsorbers from strongly absorbing media. J Appl Phys 2013;114:033504-1–11.
[102] Devarapu GCR, Foteinopoulou S. Mid-IR near-perfect absorption with a SiC photonic crystal with angle-controlled polarization selectivity. Opt Express 2012;20:13040–54.
[103] Wang T, Li P, Chigrin DN, et al. Phonon-polaritonic bowtie nanoantennas: controlling infrared thermal radiation at the nanoscale. ACS Photonics 2017;4:1753–60.
[104] Spitzer WG, Kleinman DA. Infrared lattice bands of quartz. Phys Rev B 1961;121:1324–35.
[105] Barker AS, Verleur HW, Guggenheim HJ. Infrared optical properties of vanadium dioxide above and below the transition temperature. Phys Rev Lett 1966;17:1286.
[106] Hong W-K, Cha S, Sohn JI, Kim JM. Metal-insulator phase transition in quasi-one-dimensional VO_2 structures. J Nanomater 2015;2015:538954.
[107] Miller KJ, Haglund Jr RF, Weiss SM. Optical phase change materials in integrated silicon photonic devices: review. Opt Mater Express 2018;8:2415.
[108] Dai S, Fei Z, Ma Q, et al. Tunable phonon-polaritons in atomically thin van der Waals crystals of boron nitride. Science 2014;343:1125–9.
[109] Kumar A, Low T, Hung Fung K, Avouris P, Fang NX. Tunable light-matter interaction and the role of hyperbolicity in graphene-hBN system. Nano Lett 2015;15:3172–80.
[110] Ambrosio A, Tamagnone M, Chaudhary K, et al. Selective excitation and imaging of ultraslow phonon-polaritons in thin hexagonal boron nitride crystals. Light Sci Appl 2018;7:27.
[111] Zhou Y, Qi D-X, Wang Y-K. Phonon-polaritons in cylindrically curved hBN. Opt Express 2017;25:17606–15.
[112] Zhao B, Guizal B, Zhang ZM, Fan S, Antezza M. Near-field heat transfer between graphene/hBN multilayers. Phys Rev B 2017;95:245437.
[113] Giles AJ, Dai S, Glembocki OJ, et al. Imaging of anomalous internal reflections of hyperbolic phonon-polaritons in hexagonal boron nitride. Nano Lett 2016;16:3858–65.
[114] Dai S, Tymchenko M, Yang Y, Ma Q, et al. Manipulation and steering of hyperbolic surface polaritons in hexagonal boron nitride. Adv Mater 2018;30:1706358.
[115] Ambrosio A, Tamagnone M, Chaudhary K, et al. imaging of ultra-confined phonon-polaritons in hexagonal boron nitride on gold. In: Conference on Lasers and Electro-Optics, OSA Technical Digest (online) (Washington, DC, Optical Society of America, 2018), paper FTh1K.6.
[116] Kim KS, Trajanoski D, Ho K, et al. The effect of adjacent materials on the propagation of phonon-polaritons in hexagonal boron nitride. J Phys Chem Lett 2017;8:2902–8.
[117] Gilburd L, Kim KS, Ho K, et al. Hexagonal boron nitride self-launches hyperbolic phonon-polaritons. J Phys Chem Lett 8;2017:2158–62.
[118] Caldwell JD, Kretinin AV, Chen Y, et al. Sub-diffractional volume-confined polaritons in the natural hyperbolic material hexagonal boron nitride. Nat Commun 2014;5:5221.
[119] Dai S, Ma Q, Andersen T, et al. Subdiffractional focusing and guiding of polaritonic rays in a natural hyperbolic material. Nat Commun 2015;6:6963.
[120] Li P, Lewin M, Kretinin AV, et al. Hyperbolic phonon-polaritons in boron nitride for near-field optical imaging and focusing. Nat Commun 2015;6:7507.
[121] Yoxall E, Schnell M, Nikitin AY, et al. Direct observation of ultraslow hyperbolic polariton propagation with negative phase velocity. Nat Photonics 2015;9:674–9.
[122] Shi Z, Bechtel HA, Berweger S, et al. Amplitude- and phase-resolved nanospectral imaging of phonon-polaritons in hexagonal boron nitride. ACS Photonics 2015;2:790–6.
[123] Dai S, Ma Q, Liu MK, et al. Graphene on hexagonal boron nitride as a tunable hyperbolic metamaterial. Nat Nanotechnol 2015;10:682.
[124] Brar VW, Seok Jang M, Sherrott M, et al. Hybrid surface-phonon-plasmon polariton modes in graphene/monolayer h-BN heterostructures. Nano Lett 2014;14:3876–80.

[125] Ciano C, Giliberti V, Ortolani M, Baldassarre L. Observation of phonon-polaritons in thin flakes of hexagonal boron nitride on gold. Appl Phys Lett 2018;112:153101.
[126] Geick R, Perry CH, Rupprecht G. Normal modes in hexagonal boron nitride. Phys Rev 1966;146:543–7.
[127] Richard Powell C. Symmetry, group theory and the physical properties of crystals. New York, Springer, 2010.
[128] Zheng Z, Xu N, Oscurato SL, et al. A mid-infrared biaxial hyperbolic van der Waals crystal. Sci Adv 2019;5:eaav8690.
[129] Cai Y, Zhang L, Zeng Q, Cheng L, Xu Y. Infrared reflectance spectrum of BN calculated from first principles. Solid State Commun 2007;141:262–6.
[130] Guimond S, Gobke D, Sturm JM, et al. Well-ordered molybdenum oxide layers on Au(111): preparation and properties. J Phys Chem C 2013;117:8746–57.
[131] Eda K, Longitudinal-transverse splitting effects in IR absorption spectra of MoO3. J Solid State Chem 1991;95:64–73.
[132] Ma W, Alonso-Gonzalez P, Li S, et al. In-plane anisotropic and ultra-low-loss polaritons in a natural van der Waals crystal. Nature 2018;562:557–63.
[133] Mitoraj MP, Michalak A. On the asymmetry in molybdenum-oxygen bonding in the MoO_3 structure: ETS-NOCV analysis, Struct Chem 2012;23:1369–75.
[134] Novoselov KS, Mishchenko A, Carvalho A, Castro AH, Neto, 2D materials and van der Waals heterostructures. Science 2016;353:6298.
[135] Javier Garca de Abajo F. Special issue "2D materials for nanophotonics". ACS Photonics 2017;4:2959–61.
[136] Foteinopoulou S, Panoiu NC, Shalaev VM, Subramania GS. Feature issue introduction: Beyond thin films: photonics with ultrathin and atomically thin materials. Opt Mater Express 2019;9:2427–36.
[137] Geim AK, Grigorieva IV. van der Waals heterostructures. Nature 2013;499:419.
[138] Kuzmenko AB, Benfatto L, Cappelluti E, et al. Gate tunable infrared phonon anomalies in bilayer graphene. Phys Rev Lett 2009;103:116804.
[139] Cappelluti E, Benfatto L, Kuzmenko AB. Infrared phonon activity and Fano interference in multilayer graphenes. Phys Scr 2014;T62:014018.
[140] Cappelluti E, Benfatto L, Kuzmenko AB. Phonon switching and combined Fano-Rice effect in optical spectra of bilayer graphene. Phys Rev B 2010;82:041402(R).
[141] Cappelluti E, Benfatto L, Manzardo M, Kuzmenko AB. Charged-phonon theory and Fano effect in the optical spectroscopy of bilayer graphene. Phys Rev B 2012;86:115439.
[142] Caldwell JD, Novoselov KS. Mid-infrared nanophotonics. Nat Mater 2015;14:364–6.
[143] Caldwell JD, Vurgaftman I, Tischler JG, Glembocki OJ, Owrutsky JC, Reinecke TL. Atomic-scale photonic hybrids for mid-infrared and terahertz nanophotonics. Nat Nanotech 2016;11:9.
[144] Gorbachev RV, Riaz I, Nair RR, et al. Hunting for monolayer boron nitride: optical and Raman signatures. Small 2011;7:465–8.
[145] Ajayan P, Kim P, Banerjee K. Two-dimensional van der Waals materials. Phys Today 2016;69:38.
[146] A. Molina-Sanchez and Wirtz L. Phonons in single-layer and few-layer MoS_2 and WS_2. Phys Rev B 2011;84:155413.
[147] Kumar S, Schwingenschlogl U. Thermoelectric response of bulk and monolayer $MoSe_2$ and WSe_2. Chem Mater 2015;27:1278–84.
[148] Kan M, Nam HG, Lee YH, Sun Q. Phase stability and Raman vibration of the molybdenum ditelluride ($MoTe_2$) monolayer. Phys Chem Chem Phys 2015;17:14866.
[149] Voiry D, Mohite A, Chhowalla M. Phase engineering of transition metal dichalcogenides. Chem Soc Rev 2015;44:2702–12.
[150] Chhowalla M, Shin HS, Eda G, Li L-J, Loh KP, Zhang H. The chemistry of two-dimensional layered transition metal dichalcogenide nanosheets. Nat Chem 2013;5:263–75.
[151] Lin Y-F, Xu Y, Wang S-T, et al. Ambipolar $MoTe_2$ Transistors and their applications in logic circuits. Adv Mater 2014;26:3263–9.
[152] Wu W, Morales-Acosta AD, Wang Y, Pettes MT. Isotope effect in bilayer WSe_2. Nano Lett 2019;19:1527–33.
[153] Editorial: It's still all about graphene. Nat Mater 2011;10:1.
[154] Qian J, Allen MJ, Yang Y, Dutta M, Stroscio MA. Quantized long-wavelength optical phonon modes in graphene nanoribbon in the elastic continuum model. Superl Micros 2009;46:881–8.
[155] Warner JH, Schaffel F, Bachmatiuk A, Rummeli AH. Graphene: fundamentals and emergent applications. Elsevier, 2013.
[156] Miroshnichenko AE, Flach S, Kivshar YS. Fano resonances in nanoscale structures. Rev Mod Phys 2010;82:2257–98 (and references therein).
[157] Low T, Guinea F, Yan H, Xia F, Avouris P. Novel midinfrared plasmonic properties of bilayer graphene. Phys Rev Lett 2014;112:116801.
[158] Yan H, Low T, Guinea F, Xia F, Avouris P. Tunable phonon-induced transparency in bilayer graphene nanoribbons. Nano Lett 2014;14:4581–6.
[159] Tang T-T, Zhang Y, Park C-H, et al. A tunable phonon-exciton Fano system in bilayer graphene. Nat Nanotechnol 2010;5:32–5.
[160] Lui CH, Cappelluti E, Li Z, Heinz TF. Tunable infrared phonon anomalies in trilayer graphene. Phys Rev Lett 2013;110:185504.
[161] Huang X, Cai Y, Feng X, et al. Black phosphorus carbide as a tunable anisotropic plasmonic metasurface. ACS Photonics 2018;5:3116–23.
[162] Zheng Z, Chen J, Wang Y, et al. Highly confined and tunable hyperbolic phonon-polaritons in van der Waals semiconducting transition metal oxides. Adv Mater 2018;30:1705318.
[163] Sun Y-Y, Zhang S. Communication: Effect of accidental mode degeneracy on Raman intensity in 2D materials: hybrid functional study of bilayer phosphorene. J Chem Phys 2016;145:21102.
[164] Hou X, Huang J, Liu M, et al. Single-Crystal MoO_3 Micrometer and millimeter belts prepared from discarded molybdenum disilicide heating elements. Sci Rep 2018;8:16771.
[165] Caspani L, Kaipurath RPM, Clerici M, et al. Enhanced nonlinear refractive index in ε-near-zero materials. Phys Rev Lett 2016;116:233901.
[166] Park J, Kang J-H, Liu X, Brongersma ML. Electrically tunable epsilon-near-zero (ENZ) metafilm absorbers. Sci Rep 2015;5:15754.
[167] Krayer LJ, Kim J, Munday JN. Near-perfect absorption throughout the visible using ultra-thin metal films on index-near-zero substrates [Invited]. Opt Mater Express 2019;9:330–8.
[168] Kim J, Dutta A, Naik GV, et al. Role of epsilon-near-zero substrates in the optical response of plasmonic antennas. Optica 2016;3:339–46.

[169] DeVault CT, Zenin VA, Pors A, et al. Suppression of near-field coupling in plasmonic antennas on epsilon-near-zero substrates. Optica 2018;5:2334–6.
[170] Dominguez O, Nordin L, Lu J, Feng K, Wasserman D, Hoffman AJ. Monochromatic multimode antennas on epsilon-near-zero materials. Adv Opt Mater 2019;7:1800826.
[171] Nordin L, Dominguez O, Roberts CM, et al. Mid-infrared epsilon-near-zero modes in ultra-thin phononic films. Appl Phys Lett 2017;111:091105.
[172] Berreman DW. Infrared absorption at longitudinal optic frequency in cubic crystal films. Phys Rev 1963;130:2193–8.
[173] Tamagnone M, Ambrosio A, Chaudhary K, et al. Ultra-confined mid-infrared resonant phonon polaritons in van der Waals nanostructures. Sci Adv 2018;4:7189.
[174] Merten L. Polariton dispersion in biaxial and uniaxial crystals. Phys Stat Sol 1968;30:449.
[175] da Silva RR, Silva RM, Dumelow T, da Costa JAP, Honorato SB, Ayala AP. Using phonon resonances as a route to all-angle negative refraction in the far-infrared region: the case of crystal quartz. Phys Rev Lett 2010;105:163903.
[176] Dumelow T. Chapter 2 – Negative refraction and imaging from natural crystals with hyperbolic dispersion. Solid State Phys 2016;67:103–82.
[177] Maceedo R, Dumelow T, Camley RE, Stamps RL. Oriented asymmetric wave propagation and refraction bending in hyperbolic media. ACS Photonics 2018;5:5086–94.
[178] Pendry JB. Negative refraction. Contemp Phys 2004;45:191–202.
[179] Macedo R, Rodrigues da Silva R, Dumelow T, da Costa JAP. MgF_2 as a material exhibiting all-angle negative refraction and sub-wavelength imaging due to the phonon response in the far infrared. Opt Commun 2014;310:94–9.
[180] Yang T, Jing H, Liu D. An improved description of Jones vectors of the electric fields of incident and refracted rays in a birefringent plate. J Opt A: Pure Appl Opt 2006;8:295–9.
[181] Foteinopoulou S. Photonic crystals as metamaterials. Physica B 2012;407:4056–61.
[182] Shekhar P, Atkinson J, Jacob Z. Hyperbolic metamaterials: fundamentals and applications. Nano Convergence 2014;1:14.
[183] Wasserman D, Ribaudo T, Lyon SA, Lyo SK, Shaner EA. Room temperature midinfrared electroluminescence from InAs quantum dots. Appl Phys Lett 2009;94:061101.
[184] Caldwell JD, Lindsay L, Giannini V, et al. Low-loss, infrared and terahertz nanophotonics using surface phonon-polaritons. Nanophotonics 2015;4:44–68.
[185] Faryad M, Lakhtakia A. Observation of the Uller-Zenneck wave. Opt Lett 2014;39:5204.
[186] Dionne JA, Sweatlock LA, Atwater HA, Polman A. Phys Rev B 2005;72:075405.
[187] Berini P. Figures of merit for surface plasmon waveguides. Opt Express 2006;14:13030.
[188] Knight JC. Photonic crystal fibres. Nature 2003;424:847–51.
[189] Schuller E, Falge HJ, Borstel G. Dispersion curves of surface phonon-polaritons with backbending. Phys Lett 1975;54A:317.
[190] Borstel G, Schuller E, Falge HJ. Surface phonon polaritons on absorbing crystals. Phys Stat Sol B 1976;76:759.
[191] Huang Y, Boriskina SV, Chen G. Electrically tunable near-field radiative heat transfer via ferroelectric materials. Appl Phys Lett 2014;105:244102.
[192] van Zwol PJ, Joulain K, Ben-Abdallah P, Chevrier J. Phonon-polaritons enhance near-field thermal transfer across the phase transition of VO_2. Phys Rev B 2011;84:161413(R).
[193] Francoeur M, Pinar Menguc M, Vaillon R. Near-field radiative heat transfer enhancement via surface phonon-polaritons coupling in thin films. Appl Phys Lett 2008;93:043109.
[194] Ghashami M, Geng H, Kim T, Iacopino N, Cho SK, Park K. Precision measurement of phonon-polaritonic near-field energy transfer between macroscale planar structures under large thermal gradients. Phys Rev Lett 2018;120:175901.
[195] Passler NC, Razdolski I, Gewinner S, Schollkopf W, Wolf M, Paarmann A. Second-harmonic generation from critically coupled surface phonon polaritons. ACS Photonics 2017;4:1048–53.
[196] Chen DA, Narayanaswamy A, Chen G. Surface phonon-polariton mediated thermal conductivity enhancement of amorphous thin films. Phys Rev B 2005;72:155435.
[197] Griffiths PR, Surface-enhanced infrared absorption spectroscopy: principles and applications. In: Yarwood J, Douthwaite R, Duckett S, editors. Spectroscopic properties of inorganic and organometallic compounds: techniques, materials and applications. vol. 44. London, UK, RCS, 2013.
[198] Zheng G, Chen Y, Bu L, Xu L, Su W. Waveguide-coupled surface phonon resonance sensors with super-resolution in the mid-infrared region. Opt Lett 2016;41:1582–5.
[199] Prabowo BA, Purwidyantri A, Liu K-C. Surface plasmon resonance optical sensor: a review on light source technology. Biosensor 2018;8:80.
[200] Youngblood N, Rios C, Gemo E, et al. Tunable volatility of Ge2Sb2Te5 in integrated photonics. Adv Funct Mater 2019;29:1807571.
[201] Zhang Q, Zhang Y, Li J, Soref R, Gu T, Hu J. Broadband non-volatile photonic switching based on optical phase change materials: beyond the classical figure-of-merit. Opt Lett 2018;43:94–7.
[202] Peters DW, Goldflam MD, Campione S, et al. Resonant ultrathin infrared detectors enabling high quantum efficiency, 2018 IEEE Research and Applications of Photonics In Defense Conference (RAPID), Miramar Beach, FL, USA, IEEE, 2018:1–3.
[203] Baraniuk RG, Kelly KF, Krishna S, Bridge RF. Compressive sensing architecture advances infrared camera design. Laser Focus World 2011;47:31.
[204] Choi KK, Allen SC, Sun JG, Endres D, Olver KA, Fu RX. Small pitch resonator-QWIP detectors and arrays. Infrared Phys Technol 2018;94:118–25.
[205] Huber AJ, Deutsch B, Novotny L, Hillenbrand R. Focusing of surface phonon-polaritons. Appl Phys Lett 2008;92:203104.
[206] Narimanov EE. Dyakonov waves in biaxial anisotropic crystals. Phys Rev A 2018;98:013818.
[207] Takayama O, Bogdanov AA, Lavrinenko AV. Photonic surface waves on metamaterial interfaces. J Phys Cond Mater 2017;29:463001.
[208] Folland TG, Nordin L, Wasserman D, Caldwell JD. Probing polaritons in the mid- to far-infrared. J Appl Phys 2019;125:191102.
[209] Li P, Dolado I, Alfaro-Moraz FJ, et al. Optical nanoimaging of hyperbolic surface polaritons at the edges of van der Waals materials. Nano Lett 2017;17:228–35.
[210] Alfaro-Mozaz FJ, Alonso-Gonzalez P, Velez S, et al. Nanoimaging of resonating hyperbolic polaritons in linear boron nitride antennas. Nat Commun 2017;8:15624.

[211] Autore M, Li P, Dolado I, et al. Boron nitride nanoresonators for phonon-enhanced molecular vibrational spectroscopy at the strong coupling limit. Light: Sci Appl 2018;7:17172.
[212] Kliewer KI, Fuchs R. Optical modes of vibration in an ionic crystal slab including retardation. I. Nonradiative region. Phys Rev 1966;144:495.
[213] Pendry JB. Negative refraction makes a perfect lens. Phys Rev Lett 2000;85:3966.
[214] Taubner T, Korobkin D, Urzhumov Y, Shvets G, Hillebrand R. Near-field microscopy through a SiC superlens. Science 2006;313:1595.
[215] Dai S, Quan J, Hu G, et al. Hyperbolic phonon polaritons in suspended hexagonal boron nitride. Nano Lett 2019;19:1009–14.
[216] Woessner A, Parret R, Davydovskaya D, et al. Electrical detection of hyperbolic phonon-polaritons in heterostructures of graphene and boron nitride. npj 2D Mater Appl 2017;1:25.
[217] Giles AJ, Dai S, Vurgaftman I, et al. Ultralow-loss polaritons in isotopically pure boron nitride. Nat Mater 2018;17:134.
[218] Kravets VG, Kabashin AV, Barnes WL, Grigorenko AN. Plasmonic surface lattice resonances: a review of properties and applications. Chem Rev 2018;118:5912–51.
[219] Kalkbrenner T, Ramstein M, Mlynek J, Sandoghdar V. A single gold particle as a probe for apertureless scanning near-field optical microscopy. Microscopy J 2000;202:72–6.
[220] Premaratne M, Stockman MI. Theory and technology of SPASERs. Adv Opt Photonics 2017;9:81.
[221] Tzarouchis D, Sihvola A. Light scattering by a dielectric sphere: perspectives on the Mie resonances. Appl Sci 2018;8:184.
[222] Bohren CF, Huffman DR. Absorption and scattering of light by small particles. John Wiley and Sons, 1983.
[223] Antonoyiannakis EI. Electromagnetic fields and forces in nanostructures. Imperial College of Science. Technology and Medicine, Ph.D. Thesis, 1998.
[224] Feng K, Streyer W, Islam SM, et al. Localized surface phonon-polariton resonances in polar gallium nitride. Appl Phys Lett 2015;107:081108.
[225] Ameen M, Garcia-Etxarri A, Schnell M, Hillenbrand R, Aizpurua J. Infrared phononic nanoantennas: localized surface phonon polaritons in SiC disks. Chinese Sci Bull 2010;55:2625–8.
[226] Razdolski I, Chen Y, Giles AJ, et al. Resonant enhancement of second-harmonic generation in the mid-infrared using localized surface phonon polaritons in subdiffractional nanostructures. Nano Lett 2016;16:6954–9.
[227] Dominguez O, McGinnity TL, Roeder RK, Hoffman AJ. Mid- and far-infrared optical characterization of monoclinic HfO_2 nanoparticles and evidence of localized surface phonon polaritons. Proc SPIE 2017;10100:101001G.
[228] Kivshar Y, Miroshnichenko A. Meta-optics with Mie resonances. Opt Photonics News 2017;28:25–31.
[229] Rockstuhl C, Salt MG, Herzig HP. Analysis of the phonon-polariton response of silicon carbide microparticles and nanoparticles by use of the boundary element method. J Opt Soc Am B 2005;22:481.
[230] Gubbin CR, Maier SA, De Liberato S. Theoretical investigation of phonon polaritons in SiC micropillar resonators. Phys Rev B 2017;95:035313.
[231] Caldwell JD, Glembocki OJ, Francescato Y, et al. Low-loss, extreme subdiffraction photon confinement via silicon carbide localized surface phonon polariton resonators. Nano Lett 2013;13:3690–7.
[232] Neuer III B, Wu C, Eyck GT, et al. Efficient infrared thermal emitters based on low-albedo polaritonic meta-surfaces. Appl Phys Lett 2013;102:211111.
[233] Chen Y, Francescato Y, Caldwell JD, et al. Spectral tuning of localized surface phonon polariton resonators for low-loss mid-IR applications. ACS Photonics 2014;1:718–24.
[234] Shen S, Narayanaswamy A, Chen G. Surface phonon polaritons mediated energy transfer between nanoscale gaps. Nano Lett 2009;9:2909–13.
[235] Kottmann J, Martin O, Smith D, Schultz S. Spectral response of plasmon resonant nanoparticles with a non-regular shape. Opt Express 2000;6:213–9.
[236] Gubbin GR, Berte R, Meeker MA, et al. Hybrid longitudinal-transverse phonon polaritons. Nat Commun 2019;10:1682.
[237] Venkataram PS, Hermann J, Tkatchenko A, Rodriguez AW. Phonon-polariton mediated thermal radiation and heat transfer among molecules and macroscopic bodies: nonlocal electromagnetic response at mesoscopic scales. Phys Rev Lett 2018;121:045901.
[238] Narimanov EE. Photonic hypercrystals. Phys Rev X 2014;4:041014.
[239] Foteinopoulou S. Viewpoint: photonic crystals “go hyper”. Physics 2014;7:110.
[240] Foteinopoulou S. Photonic-crystal-based polaritonic metamaterials functional at terahertz. In: 14th International Conference on Transparent Optical Networks (ICTON), We.A6.3, Coventry, UK, IEEE, 2012:1–4.
[241] Reyes-Coronado A, Acosta MF, Merino RI, et al. Self-organization approach for THz polaritonic metamaterials. Opt Express 2012;20:14663.
[242] Biehs S-A, Tschikin M, Messina R, Ben-Abdallah P. Super-Planckian near-field thermal emission with phonon-polaritonic hyperbolic metamaterials. Appl Phys Lett 2013;102:131106.
[243] Li P, Dolado I, Alfaro-Mozaz FJ, et al. Infrared hyperbolic metasurface based on nanostructured van der Waals materials. Science 2018;359:892–6.
[244] Huang KC, Povinelli ML, Joannopoulos JD. Negative effective permeability in polaritonic photonic crystals. Appl Phys Lett 2004;85:543.
[245] Schuller JA, Zia R, Taubner T, Brongersma ML. Dielectric metamaterials based on electric and magnetic resonances of silicon carbide particles. Phys Rev Lett 2007;99:107401.
[246] Shen L, Wang H, Li R, Xu Z, Chen H, Hyperbolic-polaritons-enabled dark-field lens for sensitive detection. Sci Rep 2017;7:6995.
[247] Guo T, Zhu L, Chen P-Y, Argyropoulos C. Tunable terahertz amplification based on photoexcited active graphene hyperbolic metamaterials [Invited]. Opt Mater Express 2018;8:3941–52.
[248] Rybin MV, Filonov DS, Samusev KB, Belov PA, Kivshar YS, Limonov MF. Phase diagram for the transition from photonic crystals to dielectric metamaterials. Nat Commun 2015;6:10102.
[249] Vynck K, Felbacq D, Centeno E, Cabuz AI, Cassagne D, Guizal B. All-dielectric rod-type metamaterials at optical frequencies. Phys Rev Lett 2009;102:133901.
[250] Yannopapas V, Moroz A. Negative refractive index metamaterials from inherently non-magnetic materials for deep infrared to terahertz frequency ranges. J Phys: Cond Matt 2005;17:3717–34.

[251] Alu A, Engheta N. Pairing an epsilon-negative slab with a Mu-negative slab: resonance, tunneling and transparency. IEEE Trans Antennas Prop 2003;51:2558–71.
[252] Huang KC, Bienstman P, Joannopoulos JD, Nelson KA, Fan S. Field expulsion and reconfiguration in polaritonic photonic crystals. Phys Rev Lett 2003;90:196402.
[253] Ni X, Emani NK, Kildishev AV, Boltasseva A, Shalaev VM. Broadband light bending with plasmonic nanoantennas. Science 2012;335:427–8.
[254] Kuznetsov AI, Miroshnichenko AE, Brongersma ML, Kivshar YS, Lukyanchuk B. Optically resonant dielectric nanostructures. Science 2016;354:aag2472.
[255] Liu W, Kivshar YS. Generalized Kerker effects in nanophotonics and meta-optics [Invited]. Opt Express 2018;26:13085–105.
[256] Radi Y, Asadchy VS, Kosulnikov SU. Full light absorption in single arrays of spherical nanoparticles. ACS Photonics 2015;2:653–60.
[257] Sun J, Wang X, Wu J, et al. Biomimetic moth-eye nanofabrication: enhanced antireflection with superior self-cleaning characteristic. Sci Rep 2018;8:5438.
[258] Hermes M, Brandstrup Morrish R, Huot L, et al. Mid-IR hyperspectral imaging for label-free histopathology and cytology. J Opt 2018;20:023002.
[259] Eaton HAC. Infrared imaging bolometers. In: Huber MCE, Pauluhn A, Culhane JL, Timothy JG, Wilhelm K, Zehnder A, editors. Observing photons in space: a guide to experimental space astronomy. 2013;9:515–24.
[260] Boriskina SV, Weinstein LA, Tong JK, Hsu W-C, Chen G. Hybrid optical-thermal antennas for enhanced light focusing and local temperature control. ACS Photonics 2016;3:1714–22.
[261] Ebbesen TW, Lezec HJ, Ghaemi HF, Thio T, Wolff PA. Extraordinary optical transmission through sub-wavelength hole arrays. Nature 1998;391:667–9.
[262] Garca de Abajo FJ, Gomez-Medina R, Saenz JJ. Full transmission through perfect-conductor subwavelength hole arrays. Phys Rev E 2005;72:016608.
[263] Korobkin D, Urzhumov YA, Neuner III B, et al. Mid-infrared metamaterial based on perforated SiC membrane: engineering optical response using surface phonon polaritons. Appl Phys A 2007;88:605–9.
[264] Zhang X, Liu H, Zhong Y. Microscopic analysis of surface Bloch modes on periodically perforated metallic surfaces and their relation to extraordinary optical transmission. Phys Rev B 2014;89:195431.
[265] Sakakibara R, Stelmakh V, Chan WR, et al. Practical emitters for thermophotovoltaics: a review. J Photonics Energy 2019;9:032713.
[266] Devarapu GCR, Foteinopoulou S. Broadband mid-IR superabsorption with aperiodic polaritonic photonic crystals. J Eur Opt Soc: Rapid Pub 2014;9:14012.
[267] Rodriguez-Ulibarri P, Beruete M, Serebryannikov AE. One-way quasiplanar terahertz absorbers using nonstructured polar dielectric layers. Phys Rev B 2017;96:155148.
[268] Serebryannikov AE, Nojima S, Ozbay E. One-way absorption of terahertz waves in rod-type and multilayer structures containing polar dielectrics. Phys Rev B 2014;90:235126.
[269] Baker MJ, Trevisan J, Bassan P, et al. Using Fourier transform IR spectroscopy to analyze biological materials. Nat Protoc 2014;9:1771–91.
[270] Svensson T, Hallberg T. Infrared absorption bands measured with an uncooled interferometric LWIR hyperspectral camera. Proc SPIE 10644, 2018:106440Y.
[271] Talwar DN. Direct evidence of LO phonon-plasmon coupled modes in n-GaN. Appl Phys Lett 2010;97:051902.
[272] Janipour M, Misirlioglu IB, Sendur K. Tunable surface plasmon and phonon-polariton interactions for moderately doped semiconductor surfaces. Sci Rep 2016;6:34071.
[273] Spann BT, Compton R, Ratchford D, et al. Photoinduced tunability of the reststrahlen band in 4H-SiC. Phys Rev B 2016;93:085205.
[274] Kukharskii AA. Plasmon-phonon coupling in GaAs. Solid State Commun 1973;13:1761–5.
[275] Cartella A, Nova TF, Fechner M, Merlin R, Cavalleri A. Parametric amplification of optical phonons. Proc Natl Acad Sci USA 2018;115:12148–51.
[276] Valasek J. Piezo-electric and allied phenomena in Rochelle salt. Phys Rev 1921;17:475–81.
[277] Whatmore R. Ferroelectric materials. In: Kasap S, Capper P, editors. New York, Springer handbook of electronic and photonic materials, 2017:589–614.
[278] Cochran W. Crystal stability and the theory of ferroelectricity. Adv Phys 1960;9:387–23.
[279] Worlock JM, Fleury PA. Electric field dependence of optical-phonon frequency. Phys Rev Lett 1967;19:1176.
[280] Pertsev NA, Zembilgotov AG, Hoffmann S, Waser R, Tagantsev AK. Ferroelectric thin films grown on tensile substrates: renormalization of the Curie-Weiss law and apparent absence of ferroelectricity. J Appl Phys 1999;85:1698.
[281] Wang B, Woo CH, Zheng Y. Tunable ferroelectric phase transition, UTAM Symposium on Size Effects on Material and Structural Behavior at Micron- and Nano-Scales. Hong Kong, China, Proceedings of the IUTAM Symposium, 2004:1–12.
[282] Cui C, Xue F, Hu W-J, Li L-J. Two-dimensional materials with piezoelectric and ferroelectric functionalities. npj-2D Mater Appl 2018;2:18.
[283] Liu C, Wan W, Ma J, Guo W, Yao Y. Robust ferroelectricity in two-dimensional SbN and BiP, Nanoscale 2018;10:7984–90.
[284] Guan S, Liu C, Lu Y, Yao Y, Yang SA. Tunable ferroelectricity and anisotropic electric transport in monolayer β-GeSe. Phys Rev B 2018;97:114104.
[285] Cochran W. Crystal stability and the theory of ferroelectricity. Phys Rev Lett 1959;3:412.
[286] Kukreti A, Kumar A, Naithani UC. Condensed matter: electronic structure, electrical, magnetic and optical properties-electric field dependence of Curie temperature in BaxSr1-xTiO3 ferroelectric perovskites. Indian J Pure Appl Phys 2011;49:126–31.
[287] Skoromets V, Němec H, Kadlec C, Fattakhova-Rohlfing D, Kužel P. Electric-field-tunable defect mode in one-dimensional photonic crystal operating in the terahertz range. Appl Phys Lett 2013;102:241106.
[288] Cardona M. Faraday rotation in semiconductors. In: Advances in Solid State Physics. New York, Springer, 2007:72–88.
[289] Mu Q, Fan F, Chen S, et al. Tunable magneto-optical polarization device for terahertz waves based on InSb and its plasmonic structure. Photonics Res 2019;7:325–31.
[290] Qazilbash MM, Brehm M, Andreev GO, et al. Infrared spectroscopy and nano-imaging of the insulator-to-metal transition in vanadium dioxide. Phys Rev B 2009;79:075107.

[291] Chochol J, Postava K, Cada M, et al. Magneto-optical properties of InSb for terahertz applications. AIP Adv 2016;6:115021.
[292] Chochol J, Postava K, Cada M, Pistora J. Experimental demonstration of magnetoplasmon polariton at InSb(InAs)/dielectric interface for terahertz sensor application. Sci Rep 2017;7:13117.
[293] Moncada-Villa E, Fernandez-Hurtado V, Garcia-Vidal FJ, Garcia-Martin A, Cuevas JC. Magnetic field control of near-field radiative heat transfer and the realization of highly tunable hyperbolic thermal emitters. Phys Rev B 2015;92:125418.
[294] Abraham Ekeroth RM, Ben-Abdallah P, Cuevas JC, Garcia-Martin A. Anisotropic thermal magnetoresistance for an active control of radiative heat transfer. ACS Photonics 2018;5:705–10.
[295] Ben-Abdallah P, Benisty H, Besbes M. Microsecond switchable thermal antenna. J Appl Phys 2014;116:034306.
[296] Bragaglia V, Holldack K, Boschker JE, et al. Far-infrared and Raman spectroscopy investigation of phonon modes in amorphous and crystalline epitaxial GeTe-Sb_2Te_3 alloys. Sci Rep 2016;6:28560.
[297] Chen C, Jost PH, Volker M, et al. Dielectric properties of amorphous phase-change materials. Phys Rev B 2017;95:094111.
[298] Wu S-H, Chen M, Barako MT, et al. Thermal homeostasis using microstructured phase-change materials. Optica 2017;4:1390–6.
[299] Kats MA, Blachard R, Zhang SY, et al. Vanadium dioxide as a natural disordered metamaterial: perfect thermal emission and large broadband negative differential thermal emittance. Phys Rev X 2013;3:041004.
[300] Chen S, Wang Z, Ren H, et al. Gate-controlled VO_2 phase transition for high-performance smart windows. Sci Adv 2019;5:6815.
[301] Liu C-H, Zheng J, Chen Y, Fryett T, Majumdar A. Van-der-Waals materials integrated nanophotonic devices [Invited]. Opt Mater Express 2019;9:384–99.
[302] Zhang X, Choi S, Wang D, Naylor CH, Charlie Johnson AT, Cubukcu E. Unidirectional doubly enhanced MoS_2 emission via photonic fano resonances. Nano Lett 2017;17:6715–20.
[303] Doeleman HM, Verhagen E, Femius Koenderink A. Antenna-cavity hybrids: matching polar opposites for purcell enhancements at any linewidth. ACS Photonics 2016;3:1943–51.
[304] Yu X, Yuan Y, Xu J, Yong K-T, Qu J, Song J. Strong coupling in microcavity structures: principle, design, and practical application. Laser Photonics Rev 2019;13:1800219.
[305] Papadakis GT, Zhao B, Buddhiraju S, Fan S. Gate-tunable near-field heat transfer. ACS Photonics 2019;6:709–19.
[306] Huck C, Vogt J, Neuman T, et al. Strong coupling between phonon-polaritons and plasmonic nanorods. Opt Express 2016;24:25528.
[307] Wan W, Yang X, Gao J. Strong coupling between mid-infrared localized plasmons and phonons. Opt Express 2016;24:12367–74.
[308] Luxmoore IJ, Gan CH, Qiang Liu P, et al. Strong coupling in the far-infrared between graphene plasmons and the surface optical phonons of silicon dioxide. ACS Photonics 2014;1:1151–5.
[309] Fischetti MV, Neumayer DA, Cartier EA. Effective electron mobility in Si inversion layers in metal-oxide-semiconductor systems with a high-κ insulator: the role of remote phonon scattering. J Appl Phys 2001;90:4587.
[310] Jia Y, Zhao H, Guo Q, Wang X, Wang H, Xia F. Tunable plasmon-phonon polaritons in layered graphene-hexagonal boron nitride heterostructures. ACS Photonics 2015;2:907–12.
[311] Jiang Y, Lin X, Low T, Zhang B, Chen H. Group-velocity-controlled and gate-tunable directional excitation of polaritons in graphene-boron nitride heterostructures. Laser Photonics Rev 2018;12:180049.
[312] Lina X, Yangc Y, Rivera N, et al. All-angle negative refraction of highly squeezed plasmon and phonon polaritons in graphene-boron nitride heterostructures. Proc Natl Acad Sci USA 2017;114:6717–21.
[313] Li P, Yang X, Mass TWW, et al. Reversible optical switching of highly confined phonon-polaritons with an ultrathin phase-change material. Nat Mater 2016;15:870.
[314] Huber MA, Mooshammer F, Plankl M, et al. Femtosecond photo-switching of interface polaritons in black phosphorus heterostructures. Nat Nanotech 2017;12:207.
[315] Jablan M, Soljacic M, Buljan H. Unconventional plasmon-phonon coupling in graphene. Phys Rev B 2011;83:161409.
[316] Bezares FJ, De Sanctis A, Saavedra JRM, et al. Intrinsic plasmon-phonon interactions in highly doped graphene: a near-field imaging study. Nano Lett 2017;17:5908–13.
[317] Liu PQ, Reno JL, Brener I. Quenching of infrared-active optical phonons in nanolayers of crystalline materials by graphene surface plasmons. ACS Photonics 2018;5:2706–11.
[318] Tielrooij K-J, Hesp NCH, Principi A, et al. Out-of-plane heat transfer in van der Waals stacks through electron-hyperbolic phonon coupling. Nat Nanotechnol 2018;13:41–6.
[319] Yang W, Berthou S, Lu X, et al. A graphene Zener-Klein transistor cooled by a hyperbolic substrate. Nat Nanotechnol 2018;13:47–52.
[320] Dubrovkin AM, Qiang B, Krishnamoorthy HNS, Zheludev NI, Wang QJ. Ultra-confined surface phonon polaritons in molecular layers of van der Waals dielectrics. Nat Commun 2018;9:1762.
[321] Hajian H, Serebryannikov AE, Ghobadi A, et al. Tailoring far-infrared surface plasmon polaritons of a single-layer graphene using plasmon-phonon hybridization in graphene-LiF heterostructures. Sci Rep 2018;8:13209.
[322] Imran M, Wang H, Jiang Y, Xu Z, Shen L. Harnessing graphene graphene-hBN hyperstructure for single-photon sources. Opt Express 2019;27:16461.
[323] Brouillet J, Papadakis GT, Atwater HA. Experimental demonstration of tunable graphene hyperbolic metamaterial. 2019:arXiv:1906.10663.
[324] Chaudhary K, Tamagnone M, Rezaee M, et al. Engineering phonon polaritons in van der Waals heterostructures to enhance in-plane optical anisotropy. Sci Adv 2019;5:7171.
[325] Zhang Q, Zhen Z, Liu C, Jariwala D, Cui X. Gate-tunable polariton superlens in 2D/3D heterostructures. Opt Express 2019;27:18628–41.
[326] Hajian H, Ghobadi A, Serebryannikov AE, et al. VO_2-hBN-graphene-based bi-functional metamaterial for mid-infrared bi-tunable asymmetric transmission and nearly perfect resonant absorption. J Opt Soc Am B 2019;36:1607.
[327] Folland TG, Fali A, White ST, et al. Reconfigurable infrared hyperbolic metasurfaces using phase change materials. Nat Commun 2018;9:4371.
[328] I. Staude and Rockstuhl C. To scatter or not to scatter. Nat Mater 2016;15:821.

[329] Sumikura H, Wang T, Li P, et al. Highly confined and switchable mid-infrared surface phonon polariton resonances of planar circular cavities with a phase change material. Nano Lett 2019;19:2549–54.
[330] Finch MF, Saunders CAB, Premkumar N, Yang YC, Lail BA. A 4H-SiC phonon-polariton enhanced hybrid waveguide. Fajardo, Puerto Rico, IEEE Antennas and Propagation Society International Symposium, 2016:987–8.
[331] Miao S, Premkumar N, Yang Y, Xiong D, Lail BA. Hybrid slot-waveguide fed antenna using hexagonal boron nitride Dyakonov polaritons. Opt Express 2019;27:9115–27.
[332] Qiang B, Dubrovkin AM, Krishnamoorthy HNS, et al. High Q-factor controllable phononic modes in hybrid phononic-dielectric structures. Adv Photonics 2019;1:026001.
[333] Kurman Y, Rivera N, Christensen T, et al. Control of semiconductor emitter frequency by increasing polariton momenta. Nat Photonics 2018;12:423–9.
[334] Ohtani K, Meng B, Franckie M, et al. An electrically pumped phonon-polariton laser. Sci Adv 2019;5:1632.
[335] Serebryannikov AE, Hajian H, Beruete M, Ozbay E, Vandenbosch G. Tunable deflection and asymmetric transmission of THz waves using a thin slab of graphene-dielectric metamaterial, with and without ENZ components. Opt Mater Express 2018;8:3887.
[336] Basov DN, Fogler MM, Garcia de Abajo FJ. Polaritons in van der Waals materials. Science 2016;354:aag1992.
[337] Ballarini D, Liberato SD, Polaritonics: from microcavities to sub-wavelength confinement. Nanophotonics 2019;8:641–54.
[338] Grishunin K, Huisman T, Li G, et al. Terahertz magnon-polaritons in TmFeO3, ACS Photonics 2018;5:1375–80.
[339] De Silva LMS, Wijewardena Gamalath KAIL. Modelling of exciton-polaritons. World Sci News 2018;106:194–213.
[340] Papadakis GT, Davoyan A, Yeh P, Atwater HA. Mimicking surface polaritons for unpolarized light with high-permittivity materials. Phys Rev Mater 2019;3:015202.